Numerical Modeling of Shear Bands and Dynamic Fracture in Metals

Colin James McAuliffe

Submitted in partial fulfillment of the
requirements for the degree of
Doctor of Philosophy
in the Graduate School of Arts and Sciences

COLUMBIA UNIVERSITY

2014

Abstract

Numerical Modeling of Shear Bands and Dynamic Fracture in Metals

Colin James McAuliffe

Understanding the failure of metals at high strain rate is of utmost importance in the design of a broad range of engineering systems. Numerical methods offer the ability to analyze such complex physics and aid the design of structural systems. The objective of this research will be to develop reliable finite element models for high strain rate failure modelling, incorporating shear bands and fracture. Shear band modelling is explored first, and the subsequent developments are extended to incorporate fracture. Mesh sensitivity, the spurious dependence of failure on the discretization, is a well known hurdle in achieving reliable numerical results for shear bands and fracture, or any other strain softening model. Mesh sensitivity is overcome by regularization, and while details of regularization techniques may differ, all are similar in that a length scale is introduced which serves as a localization limiter.

This dissertation contains two main contributions, the first of which presents several developments in shear band modeling. The importance of using a monolithic nonlinear solver in combination with a PDE model accounting for thermal diffusion is demonstrated. In contrast, excluding one or both of these components leads to unreliable numerical results. The Pian-Sumihara stress interpolants are also employed in small and finite deformation and shown to significantly improve the computational cost of shear band modelling. This is partly due to the fact that fewer unknowns than an irreducible discretization result from the same mesh, and more significantly, the fact that convergence of numerical results upon mesh refinement is improved drastically. This means coarser meshes are adequate to resolve shear bands, alleviating some of the computational cost of numerical modelling, which are notoriously significant. Since extremely large deformations are present during shear banding, a mesh to mesh transfer algorithm is presented for the Pian Sumihara element and used as

part of a remeshing strategy. A practical application of the numerical formulation developed is modelling the shear band failure of a friction stir welded aluminum joint under high rate loading. The energy absorption capacity of these joints are subsequently analyzed and found to be significantly weaker than untreated aluminum due to the nonhomogeneous material properties of the joint.

The second contribution is extending the shear band model described previously to account for fracture by way of the phase field method. The phase field method is modified to account for the contribution of inelastic deformation to the creation of fracture surfaces, which results in a rate and temperature dependent theory for fracture, due to the rate and temperature dependence of plasticity. The combined fracture and shear band model is shown to be capable of representing a wider spectrum of strain rates than either the phase field model or the shear band model alone.

Contents

Acknowledgements

There are several people and organizations to whom the I am grateful. To the Department of Homeland Security, for providing funding for this work. To Drs Ryan Karkkainen and Chian Yen for hosting me as an intern at the Army Research Lab. To professor Haim Waisman, for thoughtful guidance and countless interesting discussions. And to my family, for their constant support and understanding.

To my lovely wife Christina Marie

Chapter 1

Introduction

Deformations in metals subjected to high strain rates may become unstable due are shear banding or fracture. Shear banding is a localization phenomenon where thermal softening leads to narrow zones of intense inelastic deformation [138]. While a shear band typically precedes fracture, since the thermal softening leads to profound and rapid loss of load carrying capability, the shear band is considered a failure mode in its own right[9, 58, 88].

Experimentally derived material models for these loading regimes describe plastic flow as being dependent on temperature, strain rate, and a hardening parameter [138]. While several models are available, all are similar in that increasing temperature (due to plastic work) has a softening effect, causing plastic flow to occur more readily, while increases in strain rate and the hardening parameter have a hardening effect. Following the experimental work of [96], shear bands develop in three stages. In Stage 1, before localization, a homogeneous distribution of plastic strain exists. Stage 2 begins when the thermal softening effect dominates the strain and strain rate hardening effects, resulting in strain softening, and thus strain localization. Stage 3 is marked by severe localization and rapid softening, a phenomena termed stress collapse, which indicates a sudden and large drop in the material's load bearing ca-

pability [140]. Shear bands can be modeled by a system of four partial differential equations (PDEs) describing conservation of momentum, conservation of energy, elastic and inelastic constitutive relations [138]. There are several examples of scenarios where high strain rate failure involves both shear bands and cracks.

Shear banding as a precursor to void growth and fracture has been documented in several experimental works such as [8, 52, 75, 112, 123]. In addition, a ductile - brittle failure transition has been observed in the impact of notched plates by [80, 81, 144]. It was found that failure by shear banding occurred above a critical impact velocity, while brittle fracture resulted from lower impact velocities. A final example is the impact of metal plate with a projectile, where shear bands have been identified propagating parallel to the impact direction, and cracks propagate perpendicular to the impact direction [111], and shown schematically in Figure 1.1. For predictive numerical simulations of dynamic failure, it is thus crucial to account for both failure modes, since exclusion of either mode neglects important physics observed in experiments.

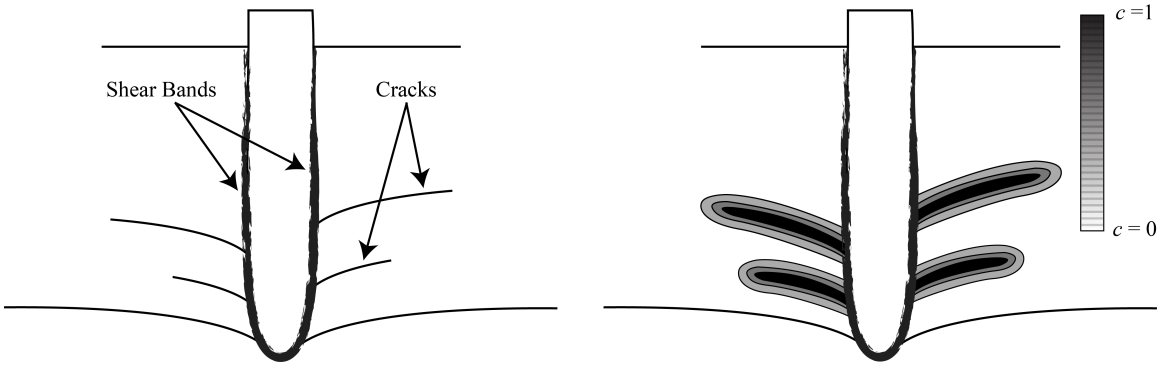

Figure 1.1: On the left, a schematic illustration of a projectile penetrating a metal plate, such as those shown in [111]. Shear failure occurs parallel to the impact direction while crack radiate out perpendicular to the impact direction. On the right, an illustration of the phase field approximation to a crack is shown. In the fully fractured phase, the phase field parameter c is 1, and 0 in the undamaged phase. The width of the diffusive crack is determined by the parameter l_0

As a prerequisite for combined shear band and fracture modeling, are several challenges in modeling shear bands without fracture to be overcome. For example, mesh size sensitivity can be a hurdle in achieving reliable numerical results for shear bands

and other localization problems. Mesh size sensitivity is the absence of convergence for localization problems upon refinement of the finite element mesh and has been observed in computations [26, 86, 143, 145]. This will occur in the numerical solution of localization problems if the governing system of PDEs has no intrinsic length scale. Common regularization techniques which are effective for strain softening materials are strain gradient theories [1, 2, 4], which have been used in the context of shear bands in [3, 83, 136], nonlocal integral averaging methods (see [24] for a review), and regularization through thermal diffusion [13, 17, 139].

A second numerical issue arising in shear band simulation is mesh alignment sensitivity. This is the tendency of shear bands to propagate along element edges, introducing a spurious anisotropy due to the mesh. Element free interpolations have been shown to significantly improve, but not eliminate this issue [85, 86]. The issues of mesh size and alignment are addressed in chapter 2, where it is found that mesh size sensitivity can be eliminated by using a monolithic nonlinear solver in conjunction with diffusive regularization. Mesh alignment sensitivity is reduced, but not totally eliminated by this formulation. Chapter 3 applies this formulation to the analysis of friction stir welded aluminum joints under high rate loading. It is found that the abrupt changes in material properties which arise from the distinct microstructural zones produced by the stir welding process significantly reduce the energy absorption capacity of the joint. This analysis suggests that weld capacity can be improved through various process modifications leading to less abrupt property changes.

In addition to these two types of mesh sensitivity, shear bands simulations involve fine scale solution features and steep gradients which require considerable resources to resolve accurately. This problem is agitated by the fact that in general the location of shear band initiation and its propagation path are not known a priori. In chapter 4, a Pian-Sumihara type element, dubbed the Pian-Sumihara Shear Band Quad (PSSBQ) is developed for shear bands. This element furnishes greater accuracy for less compu-

tational resources than the irreducible shear band quad (ISBQ) also analyzed in that chapter, which employs irreducible interpolations. In addition, it is shown that the PSSBQ is less sensitive to the stiffening effect produced by mildly distorted meshes, though remeshing is unavoidable for severely distorted meshes

Chapter 5 combines the shear model of earlier chapter with the phase field method for fracture [34, 56, 103, 104]. Growth of cracks in the phase field models cited above is driven by the elastic free energy. The elastic energy can then be split into portions which contribute to fracture and portions which do not. For example [31, 103, 104] decompose the strain energy using the principal strains, where only the tensile principal strains contribute to fracture. Inelasticity has been introduced to the phase field model by [32] who combined the phase field model for dynamic fracture with the finite deformation plasticity models in [124]. In addition, modeling of thermo mechanical damage in tungsten subject to conditions found in a fusion reactor was conducted by [44], who combined the phase field model with small deformation plasticity. For an inelastic material, the growth of the elastic free energy will be limited by yielding; in fact the elastic free energy can decrease once thermal softening begins. For metals, where the inelastic response is independent of volumetric deformations, it is conceivable that the elastic free energy due to tensile volumetric deformation will be large enough to initiate a crack. However, the contribution of the extensive inelastic working that occurs during the shear banding process will not be modeled. To remedy this, the model presented in chapter 5 includes an enhancement of the phase field model to account for the contribution of energy of internal inelastic variables to the fracture energy. This leads to the addition of source terms in the phase field evolution equation which are due to inelastic deformation. The physical motivation for inclusion of these terms in the modeling framework is due to the well known relationship between fracture and barriers to dislocation motion such as dislocation density and

grain size. This leads to a model for fracture which is explicitly rate and temperature dependent, due to the rate and temperature dependence of the internal variables.

Finally, appendix A briefly outlines work on isogeometric modeling of shear bands. This is a promising avenue of research because isogeometric analysis is fully compatible with the computational geometry technology employed by CAD software. Additionally, as shown here, NURBS shape functions are capable of accurately resolving shear bands more efficiently than low order finite elements.

Chapter 2

Analysis of a Monolithic Nonlinear Solver for Shear Bands

Mesh size sensitivity can be a hurdle in achieving reliable numerical results for shear bands and other localization problems. Mesh size sensitivity is the absence of convergence for localization problems upon refinement of the finite element mesh and has been observed in computations [26, 86, 143, 145]. This will occur in the numerical solution of localization problems if the governing system of PDEs has no intrinsic length scale. For example, Bazant and Belytschko [23] conducted an analytical study of wave propagation in a one dimensional, rate-independent, adiabatic and isothermal, strain softening bar. They found that after reaching a threshold of material instability the zone of plastic deformation will tend to a single point where the strain becomes infinite. In a numerical solution to such a system, the only length scale affecting the computation is the element size, and thus the width of the localization band will be governed by the size of the finite element mesh chosen, i.e. the numerical results will be mesh sensitive.

Inclusion of rate dependence as a means to regularize boundary value problems is well developed from a theoretical standpoint [92, 108], and has been implemented

in computations [76, 77]. Inclusion of rate dependence can be shown to prevent the change of type of PDEs which occurs with strain softening, rate independent materials [109]. The combined effects of inertia and rate dependence implies a length scale, but the response inside the localization band grows exponentially [22]. Additionally, the regularizing effect of rate dependence disappears over time, and is thus only effective if used for loading durations which are not much longer than the material relaxation time [24].

Common regularization techniques which are effective for strain softening materials are through strain gradient theories[1, 2, 4, 105, 117, 118], which has been used in the context of shear bands in [3, 83, 136], nonlocal integral averaging methods, see [24] for a review as well as [38, 127], and regularization through thermal diffusion [13–18, 139, 140]. Nonlocal methods include an integral averaging operator in the constitutive law which defines a certain state variable as a weighted average of state variables in a predefined neighborhood. Strain gradient theories employ higher order gradients of strain in the constitutive equations and diffusive regularization couples the inelastic response of the material to diffusion via the energy equation. Each of these three methods produces a material nonlocality, meaning that the constitutive law at a material point in the domain depends on history variables within some neighborhood of the point (in the case of integral averaging methods) or in the immediate vicinity of the point (in the case of strain gradient theories and diffusive regularization). This is in contrast to local material models where the constitutive law at a material point depends only on the history variables at that particular point. Nonlocality in all three of these cases leads to a characteristic length scale. It should be mentioned that the steep gradients produced during localization problems are not well resolved by coarse meshes. Thus inaccurate results can be obtained even if a mesh insensitive formulation is used without sufficient mesh refinement. See [113]

for a method which aims to improve the behavior of isoparametric elements used in localization problems.

Despite the fact that diffusion leads to a material length scale it is often assumed that since the process of shear band formation is very fast, being on the order of a few microseconds, adiabatic conditions prevail in the material. Aside from eliminating the only regularizing term in the system (and thus lead to mesh sensitive numerical formulations), this assumption is not justified on physical grounds since while the shear banding process does indeed only last a few microseconds, extremely steep temperature gradients are produced. The numerical calculations presented in this study actually predict that the diffusive and heat source terms in the energy equation are the same order of magnitude within the vicinity of the shear band. A shear band can thus be thought of as a boundary layer, the width of which is controlled by competition between shear heating, which concentrates gradients, and thermal diffusion, which smooths gradients [48–50].

While coupling diffusion to the inelastic response of the material leads to an intrinsic length scale, an appropriate numerical formulation must be used to give mesh insensitive results. A mesh insensitive formulation must preserve the physical interactions which give rise to the length scale. Several computations have used splitting schemes which solve equations sequentially rather than simultaneously, and do not use global nonlinear solution techniques such as Newton or Picard iterations [21, 30, 102, 143, 145], (it should also be noted that [102, 143, 145] model the stage three response using a viscous fluid model and thus the constitutive modeling in this stage differs from that presented here). [30, 102, 143, 145] employ explicit time integration and finite thermal conductivity. [21] also includes finite thermal conductivity, and employs an implicit-explicit Runge Kutta method, where in each governing equation, one variable is treated implicitly while all others are treated explicitly. This means, for example, the energy equation is solved implicitly to update the tempera-

ture from time step n to time step n+1, with the values of stress and plastic strain frozen at time step n. In these schemes, splitting errors occur due to the sequential solution of coupled equations and will be present for any finite time step chosen. Such errors have been found to lead to significantly degraded accuracy compared to a nonlinearly consistent solver of similar mesh size and time step in nonlinear and multiphysics problems such as radiation-diffusion, magnetohydrodynamics, and shallow water flow [82]. Additionally for shear bands, since plastic straining is a path dependent process, these errors are not recovered as the computation proceeds, and the numerical approximation diverges from the true solution. To preserve the intrinsic length scale in the PDE system and eliminate splitting errors, simultaneous solution methods are needed such as Implicit Nonlinearly Consistent (INC, also known as monolithic or simultaneous) schemes. Studies by Batra and various coworkers used simultaneous solvers to obtain mesh insensitive results for shear bands [13–18, 139, 140]. They used the method of lines to reduce their system of PDEs (which account for heat conduction) to a set of coupled ODEs, and an implicit ODE integrator to obtain the system Jacobian (through finite differencing) and solve the resulting numerical system.

A second numerical issue arising in shear band simulation is mesh alignment sensitivity. This is the tendency of shear bands to propagate along element edges, introducing a spurious anisotropy due to the mesh. Element free interpolations have been shown to significantly improve, but not eliminate this issue [85, 86]. The mixed formulation presented below does not eliminate alignment sensitivity, but the results are improved in comparison to explicit solvers.

In this chapter, a small strain formulation for a thermo-visco-plastic material is presented. This problem gives rise to a set of coupled, nonlinear PDEs, which are solved using mixed finite elements. [125] developed a mixed finite element method for elastoplasticity where displacement, stress, and equivalent plastic strain are inter-

polated degrees of freedom. They linearized the resulting nonlinear residual at the semi discrete level to develop a numerical solution using global Newton iterations at the fully discrete level. This is in contrast to classical methods for plasticity such as return mapping [124], where Newton iterations are carried out locally at the gauss points during the stress update procedure. Here we extend the methodology of Simo et al. [125] to account for a thermoviscoplastic flow rule and finite thermal conductivity by including a solution to the energy equation and temperature as an additional degree of freedom. Simultaneously solving the entire system of PDE's, as opposed to using a split scheme where individual PDE's in the system are solved sequentially, results in a high level of robustness and mesh insensitive results (as long as thermal conductivity is not zero). For comparison, we have provided results from the split scheme used in [143]. This scheme is also used by [85, 86, 102], but in conjunction with mesh free Galerkin methods as well as a different constitutive model for stage 3 of shear band formation.

The Jacobian of the system will be a large, sparse, unsymmetric matrix, the derivation of which is outlined as follows. First, the weak form of the PDEs is obtained by multiplying the strong form by a test function and integrating over the problem domain. This defines the weak form of the residual of system $\mathbf{F}[\mathbf{u}]$, where $\mathbf{u} = \begin{bmatrix} v_i & \sigma_{ij} & T & \bar{\gamma}^p \end{bmatrix}^T$ is the solution field. Here, v_i is the velocity, σ the stress, T the temperature and $\bar{\gamma}^p$ the equivalent plastic strain. The system of equations is solved when the boundary conditions are satisfied and

$$\mathbf{F}[\mathbf{u}] = \mathbf{0} \tag{2.1}$$

The residual is discretized in time using a backward Euler method, and discretized in space using Galerkin's method. The resulting nonlinear algebraic equations are then solved using Newton's method. A key point of this chapter is the computation

of the Jacobian analytically by evaluating the Gateaux derivative of the time-discrete residual. This leads to a Jacobian which is consistent with the backward Euler time stepping procedure and avoids the use of numerical differentiation procedures, which can be expensive.

The nonlinearly consistent framework requires full interpolation of the stresses and equivalent plastic strain. The Pian-Sumihara (PS) interpolations have been shown to perform well for incompressible elasticity [114], and have been used for mixed plasticity problems by [125]. Analysis by constraint counting shows that this element possesses the optimal constraint ratio for plane stress [146]. Employed here, this element gives good accuracy for relatively coarse meshes and leads to fast convergence of Newton's method.

2.1 The Numerical Formulation

2.1.1 The PDE Model

The equations describing conservation of momentum and energy, as well as the elastic and inelastic constitutive relations and boundary conditions can be written as a set of coupled PDE's, which include the following. The Momentum Equation, which includes inertial effects but ignores body forces

$$\rho \dot{v}_i = \sigma_{ij,j} \tag{2.2}$$

Here the velocity field is v_i, the time t, the stress tensor σ_{ij}, and the material density ρ. The Energy Equation, which accounts for diffusion as well as heat production in proportion to the plastic work, $\sigma_{ij} d^p_{ij}$ [130], is written as

$$\rho c \dot{T} = \kappa T_{,jj} + \chi \sigma_{ij} d^p_{ij} \tag{2.3}$$

Where T is the temperature, and κ, c, and χ are the conductivity, specific heat and Taylor-Quinney coefficient, respectively. To develop the constitutive relations, the rate of deformation is additively decomposed into elastic, inelastic and thermal parts, i.e

$$d_{ij} = \frac{1}{2}\left(l_{ij} + l_{ji}\right) = d^e_{ij} + d^p_{ij} + d^t_{ij} \tag{2.4}$$

Where the velocity gradient is defined as $l_{ij} = v_{i,j}$. Thus the Elastic Constitutive Relation, in rate form is

$$\dot{\sigma}_{ij} = C^{elas}_{ijkl}\left(d_{kl} - d^p_{kl} - d^t_{kl}\right) \tag{2.5}$$

Where C^{elas}_{ijkl} is the tensor of elastic moduli and the thermal rate of deformation is

$$d^t_{ij} = \alpha \dot{T} \delta_{ij} \tag{2.6}$$

The inelastic constitutive relation is given by

$$\dot{\bar{\gamma}}^p = \sqrt{\frac{2}{3} d^p_{ij} d^p_{ij}} \tag{2.7}$$

where $\dot{\gamma}^p$ is the time rate of change of the equivalent plastic strain.

J2 plasticity is employed, and thus the following additional constitutive relations are used:

$$d^p_{ij} = \frac{3}{2}\frac{g\left(\bar{\sigma}, T, \bar{\gamma}^p\right)}{\bar{\sigma}} s_{ij} \tag{2.8}$$

meaning the plastic strain tensor is in the same direction and the deviatoric stress tensor s_{ij} defined by

$$s_{ij} = \sigma_{ij} - \frac{1}{3}\sigma_{kk}\delta_{ij} \tag{2.9}$$

The effective stress is given by

$$\bar{\sigma} = \sqrt{\frac{3}{2} s_{ij} s_{ij}} \tag{2.10}$$

using the relations (2.8)- (2.10), the following simplifications can be made

$$\sigma_{ij} d^p_{ij} = \frac{3}{2} \frac{g\left(\bar{\sigma}, T, \bar{\gamma}^p\right)}{\bar{\sigma}} s_{ij} s_{ij} = \bar{\sigma} g\left(\bar{\sigma}, T, \bar{\gamma}^p\right) \tag{2.11}$$

$$\sqrt{\frac{2}{3} d^p_{ij} d^p_{ij}} = \frac{g\left(\bar{\sigma}, T, \bar{\gamma}^p\right)}{\bar{\sigma}} \sqrt{\frac{3}{2} s_{ij} s_{ij}} = g\left(\bar{\sigma}, T, \bar{\gamma}^p\right) \tag{2.12}$$

Lastly the flow law g, which has been used in the computations [86, 144, 145], is defined by

$$g\left(\bar{\sigma}, T, \bar{\gamma}^p\right) = \dot{\gamma_0} \left[\frac{\bar{\sigma}}{\sigma_0 \left[1 + \bar{\gamma}^p / \gamma_0\right]^N \left\{1 - \delta \left[\exp\left(\frac{T - T_0}{k}\right) - 1\right]\right\}} \right]^m \tag{2.13}$$

The material parameters $\dot{\gamma}_0$, m, N, and T_0 are a reference strain rate, rate sensitivity exponent, strain hardening exponent, and reference temperature. δ and k are thermal softening parameters. The above relations can be combined into the four governing equations which describe the evolution of the four unknown fields of velocity, stress, temperature and equivalent plastic strain. These are

$$\rho \dot{v_i} = \sigma_{ij,j} \tag{2.14}$$

$$\dot{\sigma_{ij}} = C^{elas}_{ijkl} \left(\frac{1}{2} \left[v_{k,l} + v_{l,k} \right] - \frac{3}{2} \frac{g\left(\bar{\sigma}, T, \bar{\gamma}^p\right)}{\bar{\sigma}} s_{kl} - \alpha \dot{T} \delta_{kl} \right) \tag{2.15}$$

$$\rho c \dot{T} = \kappa T_{,jj} + \chi \bar{\sigma} g\left(\bar{\sigma}, T, \bar{\gamma}^p\right) \tag{2.16}$$

$$\dot{\bar{\gamma}}^p = g\left(\bar{\sigma}, T, \bar{\gamma}^p\right) \tag{2.17}$$

Lastly the boundary conditions are

$$\begin{aligned} v_i &= \bar{v}_i \quad \text{on} \quad \Gamma^v \\ T &= \bar{T} \quad \text{on} \quad \Gamma^T \\ \sigma_{ij} n_j &= \bar{t}_i \quad \text{on} \quad \Gamma^t \\ q_i n_i &= \bar{q} \quad \text{on} \quad \Gamma^q \end{aligned} \tag{2.18}$$

Where $\bar{t}_i$ and $\bar{q}$ are the prescribed traction and prescribed flux respectively. This model considers small strains, and additionally neglects the effects of voids and microcracking that exist in a shear band [112].

2.1.2 The Discrete Model

The Discrete Residual

The weak form is obtained by multiplying the momentum equation, elastic constitutive equation, energy equation, and inelastic constitutive relation by the corresponding weight functions: w_v, w_σ, w_T, and $w_{\bar{\gamma}_p}$ respectively, and integrating over the problem domain. This defines the weak form of the residual $\mathbf{F} = \begin{bmatrix} \mathbf{F}^v & \mathbf{F}^\sigma & \mathbf{F}^T & \mathbf{F}^{\gamma_p} \end{bmatrix}^T$ where

$$\mathbf{F}^v = \int_\Omega w_i^v \rho \dot{v}_i + \nabla \cdot w_{i,j}^v \sigma_{ij} d\Omega - \int_{\Gamma^t} w_i^v \bar{t}_i d\Gamma^t = 0 \tag{2.19}$$

$$\mathbf{F}^\sigma = \int_\Omega w_{ij}^\sigma \left[\dot{\sigma}_{ij} - C_{ijkl}^{elas} \left(\frac{1}{2} \left[v_{k,l} + v_{l,k} \right] - \frac{3}{2} \frac{g\left(\bar{\sigma}, T, \bar{\gamma}^p\right)}{\bar{\sigma}} s_{kl} - \alpha \dot{T} \delta_{ij} \right) \right] d\Omega = 0 \tag{2.20}$$

$$\mathbf{F}^T = \int_\Omega w^T \left[\rho c \dot{T} - \chi \bar{\sigma} g\left(\bar{\sigma}, T, \bar{\gamma}^p\right) \right] + \kappa w_{,j}^T T_{,j} d\Omega - \int_{\Gamma^q} w^T \kappa \bar{q} d\Gamma^q = 0 \tag{2.21}$$

$$\mathbf{F}^{\gamma_p} = \int_\Omega w^{\bar{\gamma}_p} \left[\dot{\gamma}_p - g\left(\bar{\sigma}, T, \bar{\gamma}^p\right) \right] d\Omega = 0 \tag{2.22}$$

Note that the divergence theorem has been used where appropriate to reduce the order of the derivatives in the equations. This weak form contains spatial derivatives of velocity and temperature, and therefore these two fields must be approximated by

C^0 functions. On the other hand, spatial derivatives of the equivalent plastic strain and the stresses do not appear and thus C^{-1} functions will suffice. Thus, we seek to find $v_i \in S_v$, $\sigma_{ij} \in C^{-1}$, $T \in S_T$, and $\bar{\gamma}^p \in C^{-1}$ such that at any time t

$$\mathbf{F} = 0, \qquad \forall w^v \in S_v^0, \quad \forall w^\sigma \in C^{-1}, \quad \forall w^T \in S_T^0, \quad \forall w^{\gamma_p} \in C^{-1} \tag{2.23}$$

where

$$S_v = \{v_i\,(X,t)\,|v_i \in C^0, v_i = \bar{v}_i \text{ on } \Gamma^v\} \quad S_v^0 = \{w^v\,(X)\,|w^v \in C^0, w^v = 0 \text{ on } \Gamma^v\} \tag{2.24}$$

and

$$S_T = \left\{T\,(X,t)\,|T \in C^0, T = \bar{T} \text{ on } \Gamma^T\right\} \quad S_T^0 = \left\{w^T\,(X)\,|w^T \in C^0, w^T = 0 \text{ on } \Gamma^T\right\} \tag{2.25}$$

The weak form is discretized in time using the backward Euler method. The trapezoidal rule has not been used because for certain regimes of mesh size and time step for diffusion problems, this method can result in oscillations in the temperature field, which is undesirable for this problem due to the nonlinear coupling of temperature to other fields. The time discrete residual at time n+1 is then ${}_{n+1}\mathbf{F} = \left[\begin{array}{cccc} {}_{n+1}\mathbf{F}^v & {}_{n+1}\mathbf{F}^\sigma & {}_{n+1}\mathbf{F}^T & {}_{n+1}\mathbf{F}^{\gamma_p} \end{array}\right]^T$ where

$$\mathbf{F}^v = \int_\Omega w^v \rho \left[v_i - {}_n v_i \right] + \Delta t \nabla \cdot w^v_{i,j} \sigma_{ij} d\Omega - \int_{\Gamma^t} w^v_i \Delta t \bar{t}_i d\Gamma^t \tag{2.26}$$

$$\begin{aligned} \mathbf{F}^\sigma = & \int_\Omega w^\sigma_{ij} \left[\sigma_{ij} - {}_n \sigma_{ij} \right] \\ & - w^\sigma \Delta t C^{elas}_{ijkl} \left(\frac{1}{2} \left[v_{k,l} + v_{l,k} \right] - \frac{3}{2} \frac{g\left(\bar{\sigma}, T, \bar{\gamma}_p\right)}{\bar{\sigma}} s_{kl} - \alpha \dot{T} \delta_{kl} \right) d\Omega \end{aligned} \tag{2.27}$$

$$\begin{aligned} \mathbf{F}^T = & \int_\Omega w^T \left[\rho c \left(T - {}_n T \right) - \Delta t \chi \bar{\sigma}^{n+1} g\left(\bar{\sigma}, T, \bar{\gamma}_p\right) \right] \\ & + \Delta t \kappa \nabla w^T_{,j} \nabla T_{,j} d\Omega - \int_{\Gamma^q} \Delta t w^T \kappa \bar{q} d\Gamma^q \end{aligned} \tag{2.28}$$

$$\mathbf{F}^{\gamma_p} = \int_\Omega w^{\bar{\gamma}_p} \left[\bar{\gamma}_p - {}_n \bar{\gamma}_p - \Delta t g\left(\bar{\sigma}, T, \bar{\gamma}_p\right) \right] d\Omega \tag{2.29}$$

In the equation above and for the rest of this chapter, quantities are to be assumed to be taken at time step n+1, unless otherwise indicated by a subscript n.

For a single element, let the Galerkin approximation be

$$\begin{aligned} v_i &= N^v_{i\alpha} \hat{v}_\alpha & w^v_i &= N^v_{i\alpha} \hat{w}^v_\alpha \\ \sigma_{ij} &= N^\sigma_{ij\alpha} \hat{\sigma}_\alpha & w^\sigma_{ij} &= N^\sigma_{ij\alpha} \hat{w}^\sigma_\alpha \\ T &= N^T_\alpha \hat{T}_\alpha & w^T &= N^T_\alpha \hat{w}^T_\alpha \\ \bar{\gamma}^p &= N^{\bar{\gamma}_p}_\alpha \hat{\bar{\gamma}}^p_\alpha & w^{\bar{\gamma}_p} &= N^{\bar{\gamma}_p}_\alpha \hat{w}^{\bar{\gamma}_p}_\alpha \end{aligned} \tag{2.30}$$

Where N is a matrix containing the appropriate shape functions, and the hatted field variables are to be understood as vectors of nodal values belonging to one element. Substitution of the Galerkin approximation into the time discrete residual, Eqs. (2.26) - (2.29), leads to the fully discrete residual, which forms a set of coupled nonlinear algebraic equations:

$$\hat{\mathbf{F}}^{v}_{\alpha} = \mathbf{M}^{v}_{\alpha\beta}\left(\hat{v}_{\beta} - {}_{n}\hat{v}_{\beta}\right) + \Delta t\left(\mathbf{f}^{v,int}_{\beta} - \mathbf{f}^{v,ext}_{\beta}\right) = 0 \tag{2.31}$$

$$\hat{\mathbf{F}}^{\sigma}_{\alpha} = \mathbf{M}^{\sigma}_{\alpha\beta}\left(\hat{\sigma}_{\beta} - {}_{n}\hat{\sigma}_{\beta}\right) + \Delta t\mathbf{f}^{\sigma}_{\beta} = 0 \tag{2.32}$$

$$\hat{\mathbf{F}}^{T}_{\alpha} = \mathbf{M}^{T}_{\alpha\beta}\left(\hat{T}_{\beta} - {}_{n}\hat{T}_{\beta}\right) + \Delta t\left(\mathbf{f}^{T,int}_{\beta} - \mathbf{f}^{T,ext}_{\beta}\right) = 0 \tag{2.33}$$

$$\hat{\mathbf{F}}^{\gamma_p}_{\alpha} = \mathbf{M}^{\gamma_p}_{\alpha\beta}\left(\hat{\bar{\gamma}}^{p}_{\beta} - {}_{n}\hat{\bar{\gamma}}^{p}_{\beta}\right) + \Delta t\mathbf{f}^{\bar{\gamma}_p}_{\beta} = 0 \tag{2.34}$$

All matrices $\mathbf{M}$ are mass matrices, and vectors $\mathbf{f}$ are forcings defined by

$$\mathbf{f}^{v,int}_{\beta} = \int_{\Omega} N^{v}_{i\beta,j} N^{\sigma}_{ij\lambda}\hat{\sigma}_{\lambda} d\Omega \tag{2.35}$$

$$\mathbf{f}^{v,ext}_{\beta} = \int_{\Gamma^t} N^{v}_{i\beta}\bar{t}_i d\Gamma^t \tag{2.36}$$

$$\mathbf{f}^{\sigma}_{\beta} = -\int_{\Omega} N^{\sigma}_{ij\beta} C^{elas}_{ijkl}\left(\hat{d}_{kl} - \hat{d}^{p}_{kl} - \hat{d}^{t}_{kl}\right) d\Omega \tag{2.37}$$

$$\mathbf{f}^{T,int}_{\beta} = \int_{\Omega} \kappa N^{T}_{\beta,j} N^{T}_{\lambda,j}\hat{T}_{\lambda} d\Omega \tag{2.38}$$

$$\mathbf{f}^{T,ext}_{\beta} = \int_{\Omega} N^{T}_{\beta}\chi\hat{\bar{\sigma}} g\left(\hat{\bar{\sigma}}, N^{T}_{\lambda}\hat{T}_{\lambda}, N^{\gamma_p}_{\lambda}\hat{\bar{\gamma}}^{p}_{\lambda}\right) d\Omega + \int_{\Gamma^q} N^{T}_{\beta}\kappa\bar{q} d\Gamma^q \tag{2.39}$$

$$\mathbf{f}^{\bar{\gamma}_p}_{\beta} = -\int_{\Omega} N^{\gamma_p}_{\beta} g\left(\hat{\bar{\sigma}}, N^{T}_{\lambda}\hat{T}_{\lambda}, N^{\gamma_p}_{\lambda}\hat{\bar{\gamma}}^{p}_{\lambda}\right) d\Omega \tag{2.40}$$

Linearization of (2.31) - (2.34) is presented in the next section.

Consistent Linearization

A consistent linearization of the PDE system can be obtained by differentiating the time discrete residual (2.26) - (2.29), and substituting the Galerkin approximation afterwards. While tedious, this method of linearization is somewhat less so than differentiating the fully discrete residual (2.31) - (2.34). However, either method could be used to linearize the system without the need for numerical differentiation. The linearized system can be written in a partitioned form, at nonlinear iteration k

and time step n+1, as

$$\begin{bmatrix} \mathbf{J}_i^{vv} & \mathbf{J}_{ij}^{v\sigma} & \mathbf{J}^{vT} & \mathbf{J}^{v\bar{\gamma}_p} \\ \mathbf{J}_i^{\sigma v} & \mathbf{J}_{ij}^{\sigma\sigma} & \mathbf{J}^{\sigma T} & \mathbf{J}^{\sigma\bar{\gamma}_p} \\ \mathbf{J}_i^{Tv} & \mathbf{J}_{ij}^{T\sigma} & \mathbf{J}^{TT} & \mathbf{J}^{T\bar{\gamma}_p} \\ \mathbf{J}_i^{\bar{\gamma}_p v} & \mathbf{J}_{ij}^{\bar{\gamma}_p\sigma} & \mathbf{J}^{\bar{\gamma}_p T} & \mathbf{J}^{\bar{\gamma}_p\bar{\gamma}_p} \end{bmatrix}^k \begin{bmatrix} \delta v_i \\ \delta\sigma_{ij} \\ \delta T \\ \delta\bar{\gamma}^p \end{bmatrix} + \begin{bmatrix} \mathbf{F}^v \\ \mathbf{F}^\sigma \\ \mathbf{F}^T \\ \mathbf{F}^{\gamma_p} \end{bmatrix}^k = 0 \tag{2.41}$$

The Galerkin approximation of the Newton correction is also needed. This is written as

$$\begin{aligned} \delta v_i &= N_{i\beta}^v \delta\hat{v}_\beta \\ \delta\sigma_{ij} &= N_{ij\beta}^\sigma \delta\hat{\sigma}_\beta \\ \delta T &= N_\beta^T \delta\hat{T}_\beta \\ \delta\bar{\gamma}^p &= N_\beta^{\gamma_p} \delta\hat{\bar{\gamma}}_\beta^p \end{aligned} \tag{2.42}$$

The product of the Jacobian $\mathbf{J}$ and the Newton correction $\delta\mathbf{u}$ is the first variation of $\mathbf{F}$ in the direction of $\delta\mathbf{u}$. This is also known as the Gateaux derivative and is defined as

$$\mathbf{J}\delta\mathbf{u} = \delta\mathbf{F}\left[\mathbf{u}^k\right] = \lim_{\epsilon\to 0} \frac{\mathbf{F}\left[\mathbf{u}^k + \epsilon\delta u\right] - \mathbf{F}\left[\mathbf{u}^k\right]}{\epsilon} = \frac{d}{d\epsilon}\mathbf{F}\left[\mathbf{u}^k + \epsilon\delta\mathbf{u}\right]\Big|_{\epsilon=0} \tag{2.43}$$

This derivative can be computed analytically without numerical differentiation in blocks, for example the block

$$\mathbf{J}_i^{vv}\delta v_i = \lim_{\epsilon\to 0} \frac{\mathbf{F}^v\left[v_i + \epsilon\delta v_i\right] - \mathbf{F}^v\left[v_i\right]}{\epsilon} \tag{2.44}$$

Plugging (2.26) into (2.44) gives

$$\mathbf{J}_i^{vv}\delta v_i = \lim_{\epsilon\to 0}\frac{1}{\epsilon}\left\{\int_\Omega w^v\rho\left[v_i+\epsilon\delta v_i - {}_nv_i\right]+\Delta t w_{i,j}^v\sigma_{ij}-\int_{\Gamma^t}\Delta t w_i^v\bar{t}_i d\Gamma^t\right\} \tag{2.45}$$
$$-\frac{1}{\epsilon}\left\{\int_\Omega \rho w^v\left[v_i - {}_nv_i\right]+\Delta t w_{i,j}^v\sigma_{ij}-\int_{\Gamma^t}\Delta t w_i^v\bar{t}_i d\Gamma^t\right\}$$

Simplifying leads to the expression

$$\mathbf{J}_i^{vv}\delta v_i = \int_\Omega \rho w_i^v\delta v_i d\Omega \tag{2.46}$$

Substitution of the Galerkin approximation for the Newton correction into (2.46), leads to a vector of the Newton correction of the velocity field multiplied by a mass matrix. i.e

$$\mathbf{J}_{\alpha\beta}^{vv}\delta\hat{v}_\beta = \int_\Omega \rho N_{i\alpha}^v N_{i\beta}^v d\Omega\delta\hat{v}_\beta$$

Blocks arising from the linearization of the constitutive law can be computed similarly, for example

$$\mathbf{J}^{T\bar{\gamma}_p}\delta\bar{\gamma}^p = \lim_{\epsilon\to 0}\frac{\mathbf{F}^T\left[\bar{\gamma}^p+\epsilon\delta\bar{\gamma}^p\right]-F\left[\bar{\gamma}^p\right]}{\epsilon} \tag{2.47}$$

Using (2.26) gives

$$\begin{aligned}\mathbf{J}^{T\bar{\gamma}_p}\delta\bar{\gamma}^p &= \lim_{\epsilon\to 0}\frac{1}{\epsilon}\int_\Omega \Delta t\chi w^T\left[\bar{\sigma}g\left(\bar{\sigma},T,\bar{\gamma}^p\right)-\bar{\sigma}g\left(\bar{\sigma},T,\bar{\gamma}^p+\epsilon\delta\bar{\gamma}^p\right)\right]\\ &= \Delta t\int_\Omega w^T\frac{mn}{\gamma_0+\bar{\gamma}^p}\chi\bar{\sigma}g\left(\bar{\sigma},T,\bar{\gamma}^p\right)\delta\bar{\gamma}^p d\Omega\end{aligned} \tag{2.48}$$

Substituting the Galerkin approximation into (2.48) gives

$$\mathbf{J}_{\alpha\beta}^{T\bar{\gamma}^p}\delta\hat{\bar{\gamma}}_\beta^p = \Delta t\int_\Omega N_\alpha^T\frac{mn}{\gamma_0+N_\zeta^{\gamma_p}\hat{\bar{\gamma}}_\zeta^p}\chi\hat{\bar{\sigma}}g\left(\hat{\bar{\sigma}},N_\lambda^T\hat{T}_\lambda,N_\lambda^{\gamma_p}\hat{\bar{\gamma}}_\lambda^p\right)N_\beta^{\gamma_p}d\Omega\delta\hat{\bar{\gamma}}_\beta^p$$

Repeating this process for each block leads to a Jacobian with the following block structure:

$$\begin{bmatrix} \mathbf{M}^{v}_{\alpha\beta} & \Delta t\mathbf{K}^{v}_{\alpha\beta} & \mathbf{0} & \mathbf{0} \\ \Delta t\mathbf{K}_{\sigma} & \mathbf{M}^{\sigma}_{\alpha\beta} + \Delta t\mathbf{G}^{\sigma\sigma}_{\alpha\beta} & \Delta t\mathbf{G}^{\sigma T}_{\alpha\beta} & \Delta t\mathbf{G}^{\sigma\bar{\gamma}_p}_{\alpha\beta} \\ \mathbf{0} & \Delta t\mathbf{G}^{T\sigma}_{\alpha\beta} & \mathbf{M}^{T}_{\alpha\beta} + \Delta t\left(\mathbf{K}^{T}_{\alpha\beta} + \mathbf{G}^{TT}_{\alpha\beta}\right) & \Delta t\mathbf{G}^{T\bar{\gamma}_p}_{\alpha\beta} \\ \mathbf{0} & \Delta t\mathbf{G}^{\bar{\gamma}_p\sigma}_{\alpha\beta} & \Delta t\mathbf{G}^{\bar{\gamma}_p T}_{\alpha\beta} & \mathbf{M}^{\gamma_p}_{\alpha\beta} + \Delta t\mathbf{G}^{\bar{\gamma}_p\bar{\gamma}_p}_{\alpha\beta} \end{bmatrix}^{k} \begin{bmatrix} \delta\hat{v}_{\beta} \\ \delta\hat{\sigma}_{\beta} \\ \delta\hat{T}_{\beta} \\ \delta\hat{\bar{\gamma}}^{p}_{\beta} \end{bmatrix} + \begin{bmatrix} \hat{\mathbf{F}}^{v} \\ \hat{\mathbf{F}}^{\sigma} \\ \hat{\mathbf{F}}^{T} \\ \hat{\mathbf{F}}^{\gamma_p} \end{bmatrix}^{k} = 0 \tag{2.49}$$

The stiffness matrices arising from linearization of the inelastic constitutive law are denoted by $\mathbf{G}$. The structure of the Jacobian reflects the strongly coupled nature of the system of PDE's, and does not reveal any clear way to simplify or reduce the system by eliminating any of the four fields in $\mathbf{u}$. Note that the Jacobian is not symmetric.

2.1.3 Choice of Shape Functions

It is well known that for similar mixed finite element formulations (e.g. in computational fluid mechanics [132] or incompressible elasticity [72]), the Babuska-Brezzi (BB) condition [7, 36] applies, and hence the polynomial order of shape functions for the different primary fields should be carefully selected. In this case, we find that good performance can be obtained with discontinuous interpolations of stress and plastic strain. Thus, the element shape functions used here are those first proposed in [125], but with the addition of a temperature degree of freedom. The shape functions are standard bilinear functions for velocity and temperature, combined with the shape functions proposed by Pian and Sumihara [114] for stress and discontinuous bilinear shape functions for the equivalent plastic strain. In two dimensions under

plane strain conditions, the stress and equivalent plastic strain shape functions for a square element are given by

$$\begin{bmatrix} \sigma_{11} & \sigma_{12} & 0 \\ \sigma_{21} & \sigma_{22} & 0 \\ 0 & 0 & \sigma_{33} \end{bmatrix} = N^{\sigma}_{ij\alpha}\hat{\sigma}_{\alpha} = \begin{bmatrix} \hat{\sigma}_1 + \xi_2\hat{\sigma}_4 & \hat{\sigma}_3 & 0 \\ \hat{\sigma}_3 & \hat{\sigma}_2 + \xi_1\hat{\sigma}_5 & 0 \\ 0 & 0 & \hat{\sigma}_6 \end{bmatrix} \tag{2.50}$$

$$N^{\gamma_p i}_{\lambda}\left(\xi^j_1, \xi^j_2\right) = \delta_{ij} \qquad i, j = 1, ..., 4 \tag{2.51}$$

Where δ_{ij} is the Kroneker delta and ξ^j_1, ξ^j_2 are the isoparametric coordinates of the jth gauss point of a two by two quadrature rule. Thus σ_{11} is linear in the X_2 direction, σ_{22} is linear in the X_1 direction, and σ_{33} and σ_{12} are piecewise constant. All other stress components are zero due to plane conditions. Both the stress and the equivalent plastic strain shape functions are discontinuous from one element to the next. More details on the Pian Sumihara interpolants for unstructured meshes in the context of finite deformation is provided in chapter 4.

A rigorous mathematical study along the lines of the BB conditions is beyond the scope of this chapter. However, the attractiveness of the Pian-Sumihara (PS) element can be illustrated with the simpler constraint counting method [146] which shows that the element has the ideal number of constraints for plane conditions. The same analysis shows that piecewise constant stress shape functions will not be stable and bilinear stress shape functions will lead to an element that tends to lock.

These shape functions result in three degrees of freedom per node: two velocities and one temperature. The stress and equivalent plastic strain degrees of freedom are discontinuous across element boundaries, and are therefore associated with elements rather than nodes. The shape functions in equations (2.50) - (2.51) result in six stress and four equivalent plastic strain degrees of freedom per element. Thus the

total number of unknowns for the PS element is

$$n_{PS} = 3n_{node} + 10n_{elem} \tag{2.52}$$

Where n_{node} and n_{elem} are the number of nodes and elements in the mesh respectively. Clearly, there is a significant increase in the number of unknowns of the mixed element compared to the corresponding irreducible element. However, owing to the discontinuous functions, the Jacobian of the PS is very sparse.

2.2 Implementation

This INC formulation has been implemented in one dimension in MATLAB and in two dimensions as a user element in the FORTRAN based finite element program FEAP [131]. All 2D meshes were generated using Gmsh [59]. ParaView [67] and Matplotlib [74] were used to visualize the results.

A mesh refinement study has been conducted for a 20×20 μm^2 part in plane strain tension, and an alignment study has been conducted on the same part in plane strain shearing as shown in Figure 2.1. Additionally, a 1D mesh refinement study has been conducted for a $3 \cdot 10^{-3} m$ rod in tension.

Shear bands nucleate at material imperfections (or an inhomogeneity in the solution field such as a stress concentration), which is set for both the 1D and 2D tension examples by altering the yield stress and yield strain at various points in the material. For the shearing example, perturbing the material properties is not necessary because the loading conditions shown in 2.1 b) produce a stress concentration which triggers the shear band.

For each case, zero flux and zero traction boundary conditions are used. A time step of 1E-8 seconds was used for all meshes in each 2D example for the INC method, while a time step of 1E-9 was used for the 1D example. The conditionally stable

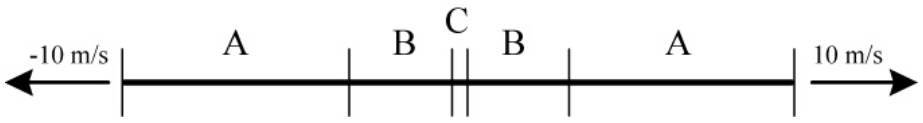

(a) 1D Tension

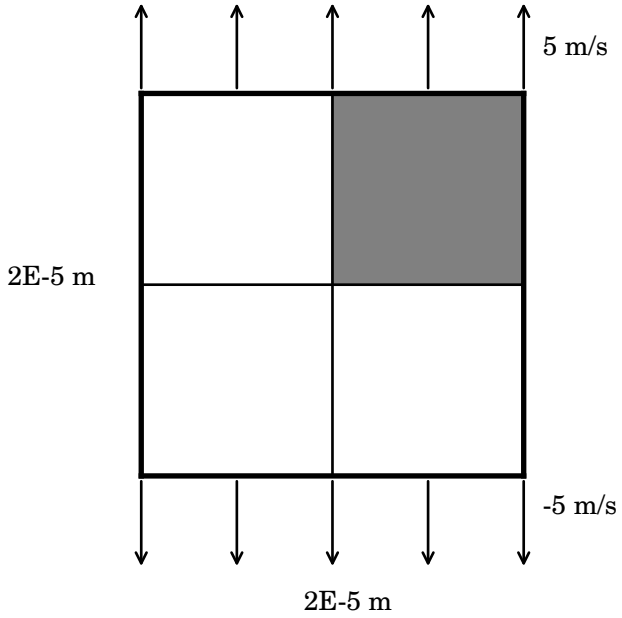

(b) Plane Strain Tension

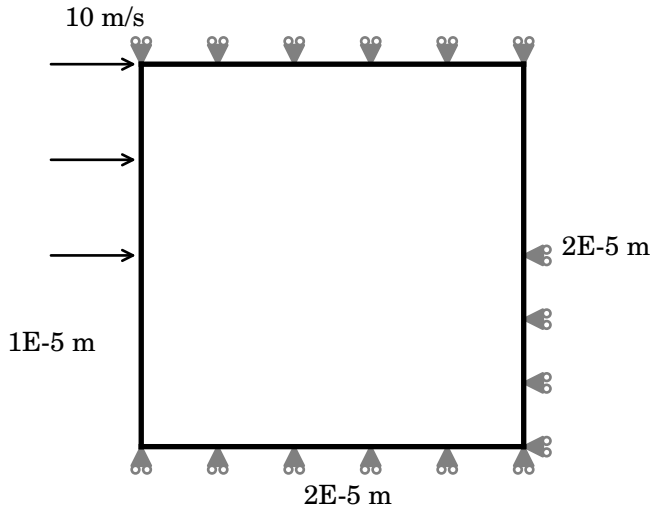

(c) Plane Strain Shearing

Figure 2.1: Problem Configurations for a) 1D tension example b) a 2D plane strain tension example with a shear band resulting in 45^o and c) a pure shearing example

Table 2.1: Material Properties and Parameters

Property Name	Symbol	Value	Unit
Young's Modulus	E	200E9	Pa
Poisson's Ratio	ν	0.3	-
Mass Density	ρ	7830	$\frac{kg}{m^3}$
Specific Heat	c	448	$\frac{J}{kgK}$
Taylor - Quinney Coefficient	χ	.9	-
Thermal Conductivity	κ	803.5	$\frac{W}{mK}$
Reference Strain Rate	$\dot{\gamma}_0$	.001	$\frac{1}{s}$
Rate Sensitivity Parameter	m	70	-
Yield Stress	σ_0	2000E6	Pa
Yield Strain	γ_0	.01	-
Strain Hardening Exponent	n	.01	-
Reference Temperature	T_0	293	K
Thermal Softening Parameter	δ	.8	-
Thermal Softening Parameter	k	500	K

Table 2.2: 1D Meshes are arranged to provide finer resolution in the center of the rod. The lengths of the partitions labeled A, B, and C (see Figure 2.1) are $400\mu m$, $98\mu m$, and $4\mu m$ respectively

1D Mesh Number	Elements in A	Elements in B	Elements in C	Total Elements
1	10	30	21	101
2	10	30	41	121
3	10	30	61	141
4	10	30	81	161

split method employs a time step according to the CFL condition explained below. Four meshes were tested for the 1D example, with the element distributions for each mesh shown in Table 2.2, with an applied velocity of 10 m/s to each end of the rod. These will be referred to as 1D Meshes 1-4. Four meshes were tested for the plane strain tension example, $10 \times 10, 20 \times 20, 40 \times 40$ and 80×80 elements, with an applied velocity of 5 m/s. These will be referred to as 2D Meshes 1-4, respectively. Two types of meshes were tested for the shearing case near the shear band zone: structured and unstructured (see Figure 2.2). An applied velocity of 10 m/s was set on the upper left edge of the pure shearing example shown in Fig. 2.1(b). These meshes were chosen so that there would be roughly ten elements in the y direction in the middle 1.6 μm

of the part. The applied velocity was ramped linearly from 0 to the full value over one microsecond. For the FEAP implementation, Newton iterations using Eq. (2.49) were terminated by the default FEAP tolerance, which is

$$E^k \leq 10^{-16} E^1 \tag{2.53}$$

Where

$$E_k = \delta \mathbf{u}_\beta^k \mathbf{F}_\beta^k \tag{2.54}$$

$$E_1 = \delta \mathbf{u}_\beta^1 \mathbf{F}^{1_\beta} \tag{2.55}$$

For the MATLAB implementation, Newton iterations were terminated when the L_2 norm of the residual reaches a tolerance of 10^{-13}.

For comparison, results were obtained using a split, explicit scheme, which proceeds in three main steps as follows: first, stresses and the equivalent plastic strain are updated using the semi-implicit stress update algorithm known as the Rate Tangent Modulus method [116], assuming adiabatic heat rise. Second, the velocities are updated according to the explicit scheme

$${}_n\hat{a}_\beta^v = \left(\mathbf{M}_{\alpha\beta}^{vL}\right)^{-1} {}_n\mathbf{f}_\beta^{v,int*} \tag{2.56}$$

$$\hat{v}_\beta = {}_n\hat{v}_\beta + \Delta t \; {}_n\hat{a}_\beta^v \tag{2.57}$$

where ${}_n\hat{a}_\beta^v$ are the accelerations at time step n and $\hat{v}_\beta$ are the velocities at step n+1. This is a Forward Euler update of the momentum balance with $\mathbf{M}_{\alpha\beta}^{vL}$ the lumped mass matrix. The star on the internal force vector in Eq. (2.56) is to distinguish it

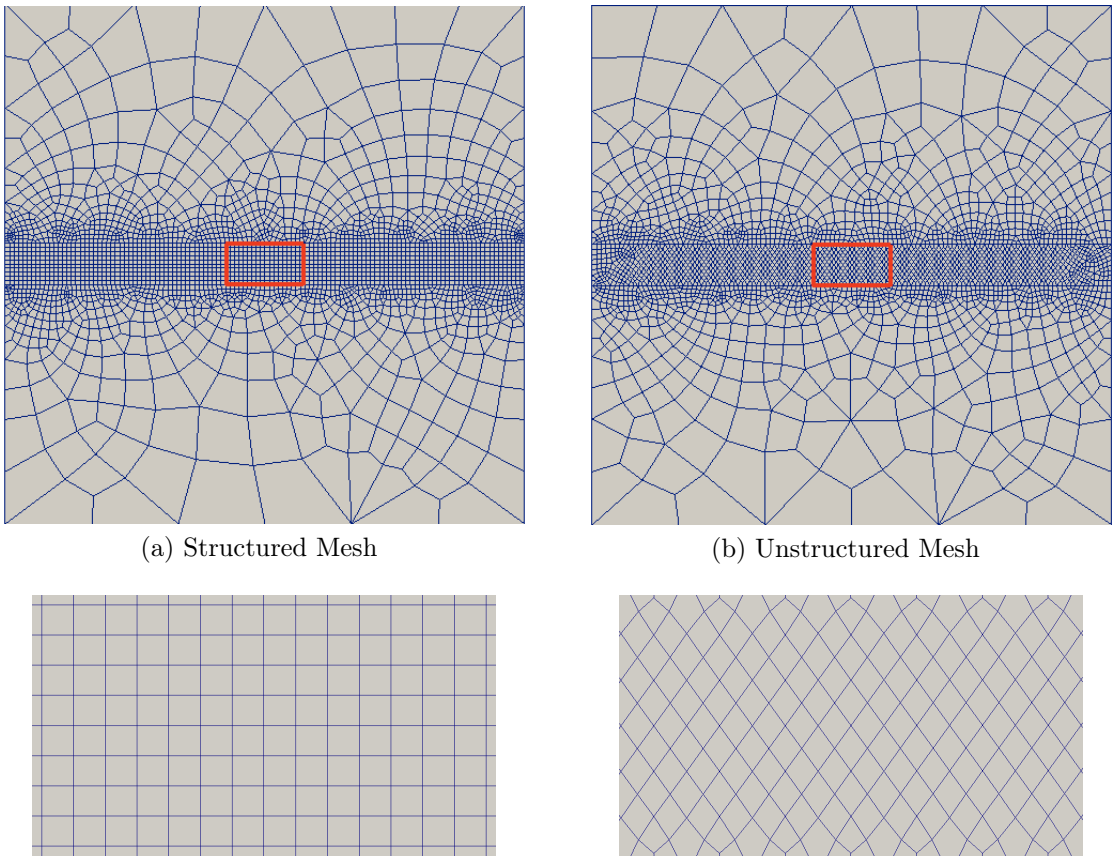

(a) Structured Mesh

(b) Unstructured Mesh

(c) Structured Mesh, zoomed to red box shown above

(d) Unstructured Mesh, zoomed to red box shown above

Figure 2.2: Meshes for the Shearing example

from the internal force defined in Eq. (2.35)

$$ {}_n\mathbf{f}_\beta^{v,int*} = \int_\Omega N^v_{i\beta,j}\ {}_n\sigma_{ij} d\Omega \tag{2.58} $$

The last step is to update the temperature field according to

$$ {}_n\hat{v}_\beta^T = \left(\mathbf{M}^{TL}_{\alpha\beta}\right)^{-1}\ {}_n\left(\mathbf{f}_\beta^{T,int} - \mathbf{f}_\beta^{T,ext*}\right) \tag{2.59} $$

$$ \hat{T}_\beta = {}_n\hat{T}_\beta + \Delta t\ {}_n\hat{v}_\beta^T \tag{2.60} $$

Again this is a Forward Euler update with lumped mass matrix $\mathbf{M_{TL}}$. The internal and body heating vectors given by

$$ {}_n\mathbf{f}_\beta^{T,ext*} = \int_\Omega N_\beta^T \; {}_n\bar{\sigma} \; {}_n g \left(\bar{\sigma}, N_\zeta^T \hat{T}_\zeta, N_\zeta^{\gamma_p} \hat{\bar{\gamma}}_\zeta^p \right) d\Omega \tag{2.61} $$

Note that here the stresses are not interpolated with their own shape functions, instead the stresses and equivalent plastic strains are sampled at the Gauss points during the numerical quadrature.

This method does not involve the factorization of any system matrices, nor does it require Newton iterations, either at the global or local level (as is the case in return mapping schemes) since the rate tangent modulus stress update is a one step method. Since this scheme is conditionally stable, a Courant number of .7 has been used, and thus the time step is obtained from is

$$ \Delta t = .7 \min \left(\Delta t_{crit}^{mechanical}, \Delta t_{crit}^{thermal} \right) \tag{2.62} $$

where the mechanical and thermal critical time steps are

$$ \Delta t_{crit}^{mechanical} = \frac{h}{\sqrt{\frac{E}{\rho}}} \tag{2.63} $$

$$ \Delta t_{crit}^{thermal} = \frac{\rho c h^2}{2\kappa} \tag{2.64} $$

where h is the shortest node to node distance for any element in the mesh. For the material properties and element sizes used, all cases are controlled by the mechanical critical time step.

2.3 Results

2.3.1 One Dimensional Tension

A single material imperfection was created in the rod by varying the yield stress and yield strain smooth function β_{1D} (see Figure 2.3) so that

$$\sigma_{yield}\left(X_1\right) = \sigma_0 \beta\left(X_1\right) \tag{2.65}$$

$$\gamma_{yield}\left(X_1\right) = \gamma_0 \beta\left(X_1\right) \tag{2.66}$$

$$\beta_{1D}\left(X_1\right) = 1 - 0.01\left[sech\left(\frac{X_1}{5 \cdot 10^{-5}}\right)\right]^2 \tag{2.67}$$

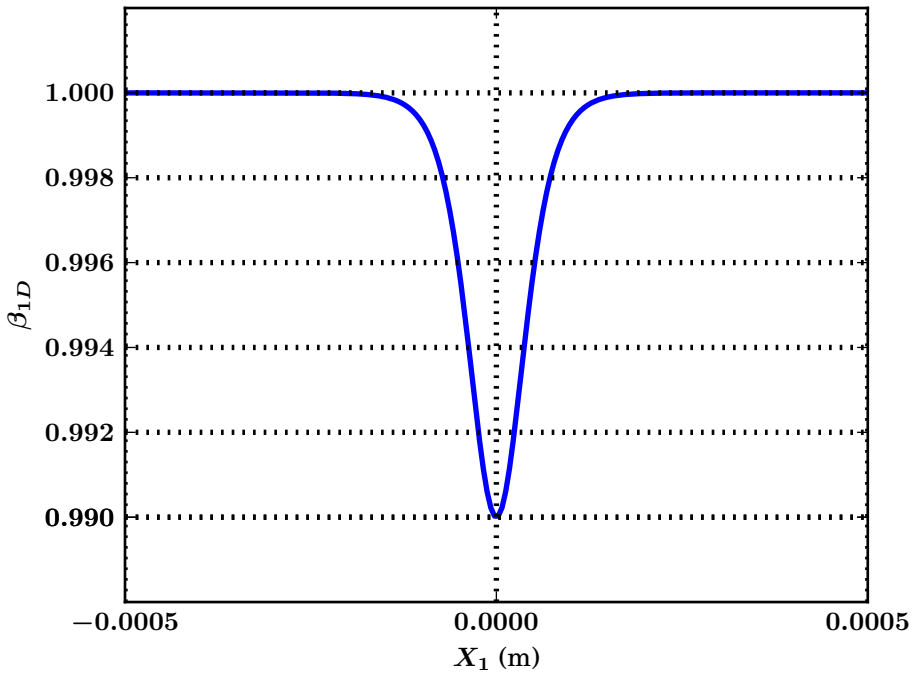

Figure 2.3: β_{1D} function defined by Eq. (2.67)

This causes the shear band to initiate at the center of the rod. The shape functions for the 1D element are linear for velocity and temperature, and piecewise constant for stress and plastic strain. Average stress vs. average strain as well as the plastic

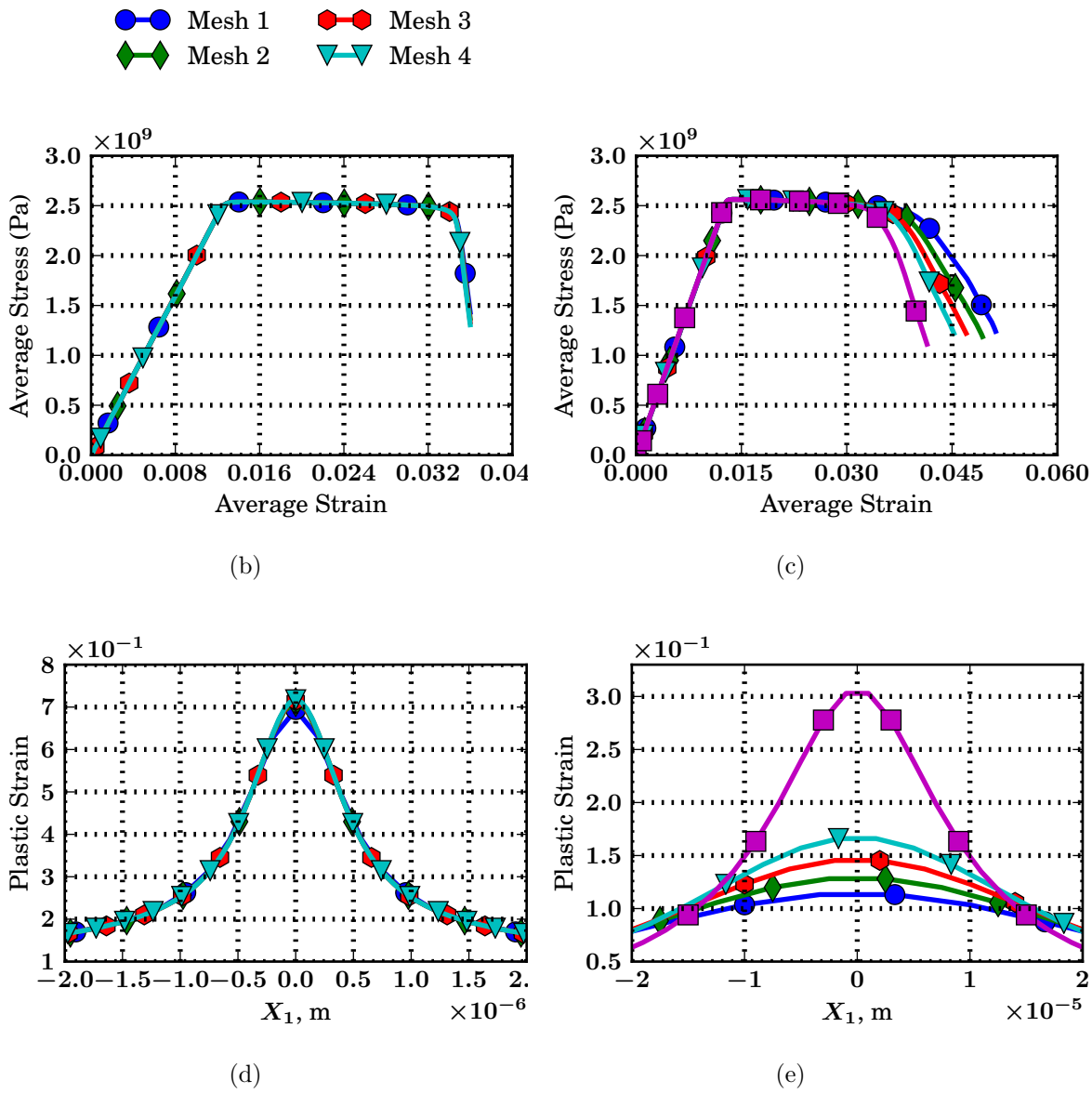

Figure 2.4: 1D solution fields using the coupled formulation developed in this study (shown on the left) and split scheme using the rate tangent modulus method (shown on the right). Figures (c) and (d) are shown at an average strain of .035

strain for the two methods are shown in Figure 2.4. The INC method produces nearly identical plots for each mesh configuration, even after stress collapse. On the other hand the split scheme shows that increasing mesh refinement leads to earlier onset and greater rapidity of stress collapse. In fact, due to this, results could not be obtained after the onset of stress collapse for any of the 1D meshes 1-4, where element sizes at the center of the domain are very small. Therefore, coarser meshes were used for the

split method and thus Figure 2.4 should not be viewed as a direct comparison of the two methods. The two methods are compared for identical meshes in the 2D tension and shearing examples.

It should be emphasized that the split scheme used here is not the only possible split solver. The scheme was chosen because it is commonly used in the literature, and has a low computational cost per time step because it does not require any nonlinear iterations. Possibilities for backward Euler split solvers include the Picard linearization, as well as field split linearizations. These can be viewed as solving the nonlinear equations (2.31) - (2.34) using some approximation $\mathbf{P}$ to the Jacobian $\mathbf{J}$. Three possibilities are

$$\mathbf{P}_{Picard} = \begin{bmatrix} \mathbf{M}^{v}_{\alpha\beta} & \Delta t\mathbf{K}^{v}_{\alpha\beta} & \mathbf{0} & \mathbf{0} \\ \Delta t\mathbf{K}_{\sigma} & \mathbf{M}^{\sigma}_{\alpha\beta} & \mathbf{0} & \mathbf{0} \\ \mathbf{0} & \mathbf{0} & \mathbf{M}^{T}_{\alpha\beta} + \Delta t\mathbf{K}^{T}_{\alpha\beta} & \mathbf{0} \\ \mathbf{0} & \mathbf{0} & \mathbf{0} & \mathbf{M}^{\gamma_p}_{\alpha\beta} \end{bmatrix} \tag{2.68}$$

$$\mathbf{P}_{FS1} = \begin{bmatrix} \mathbf{M}^{v}_{\alpha\beta} & \Delta t\mathbf{K}^{v}_{\alpha\beta} & \mathbf{0} & \mathbf{0} \\ \Delta t\mathbf{K}_{\sigma} & \mathbf{M}^{\sigma}_{\alpha\beta} + \Delta t\mathbf{G}^{\sigma\sigma}_{\alpha\beta} & \mathbf{0} & \mathbf{0} \\ \mathbf{0} & \mathbf{0} & \mathbf{M}^{T}_{\alpha\beta} + \Delta t\left(\mathbf{K}^{T}_{\alpha\beta} + \mathbf{G}^{TT}_{\alpha\beta}\right) & \mathbf{0} \\ \mathbf{0} & \mathbf{0} & \mathbf{0} & \mathbf{M}^{\gamma_p}_{\alpha\beta} + \Delta t\mathbf{G}^{\bar{\gamma}_p\bar{\gamma}_p}_{\alpha\beta} \end{bmatrix} \tag{2.69}$$

$$\mathbf{P}_{FS2} = \begin{bmatrix} \mathbf{M}^{v}_{\alpha\beta} & \Delta t\mathbf{K}^{v}_{\alpha\beta} & \mathbf{0} & \mathbf{0} \\ \Delta t\mathbf{K}_{\sigma} & \mathbf{M}^{\sigma}_{\alpha\beta} + \Delta t\mathbf{G}^{\sigma\sigma}_{\alpha\beta} & \mathbf{0} & \Delta t\mathbf{G}^{\sigma\bar{\gamma}_p}_{\alpha\beta} \\ \mathbf{0} & \mathbf{0} & \mathbf{M}^{T}_{\alpha\beta} + \Delta t\left(\mathbf{K}^{T}_{\alpha\beta} + \mathbf{G}^{TT}_{\alpha\beta}\right) & \mathbf{0} \\ \mathbf{0} & \Delta t\mathbf{G}^{\bar{\gamma}_p\sigma}_{\alpha\beta} & \mathbf{0} & \mathbf{M}^{\gamma_p}_{\alpha\beta} + \Delta t\mathbf{G}^{\bar{\gamma}_p\bar{\gamma}_p}_{\alpha\beta} \end{bmatrix} \tag{2.70}$$

The effectiveness of these matrices as an approximate Jacobian can be evaluated by examining the eigenvalues of the iteration matrix $\mathbf{T}$ defined by

$$\mathbf{T} = \mathbf{I} - \mathbf{P^{-1}J} \tag{2.71}$$

Eigenvalues of $\mathbf{T}$ with modulus close to zero correspond to modes which will be smoothed rapidly by updating the solution field with $\delta\mathbf{u}^P$ where

$$\delta\mathbf{u}^P = \mathbf{P}^{-1}\mathbf{F} \tag{2.72}$$

Eigenvalues with modulus close to, but less than one correspond to modes which will be smoothed very slowly, and eigenvalues with modulus greater than one correspond to modes which will be amplified by the iteration defined in Eq. (2.72).

At an average strain of 0.035, the INC method converges with 6 Newton iterations with a time step of 1E-9. Evaluating the iteration matrices for the three field split approximations to the Jacobian with the same time step shows that all of the three approximations will amplify, rather than smooth the error (see Figure 2.5). In order for all modes to reside within the ball of convergence, the time step needs to be reduced by three orders of magnitude for the Picard approximation, and one order of magnitude for the field split approximations. These results are summarized in Table 2.3. These three implicit split methods will thus require more linear solves than the INC method to simulate the same amount of physical time. Again, it should be emphasized that this does not exhaust the possibilities of split solvers. However, in light of the results just discussed as well as the fact that the INC solver is competitive in terms of computational cost (see next section), we contend that future efforts are better spent attempting to improve the efficiency of the INC solver, rather than improve the accuracy and convergence behavior of a split solver.

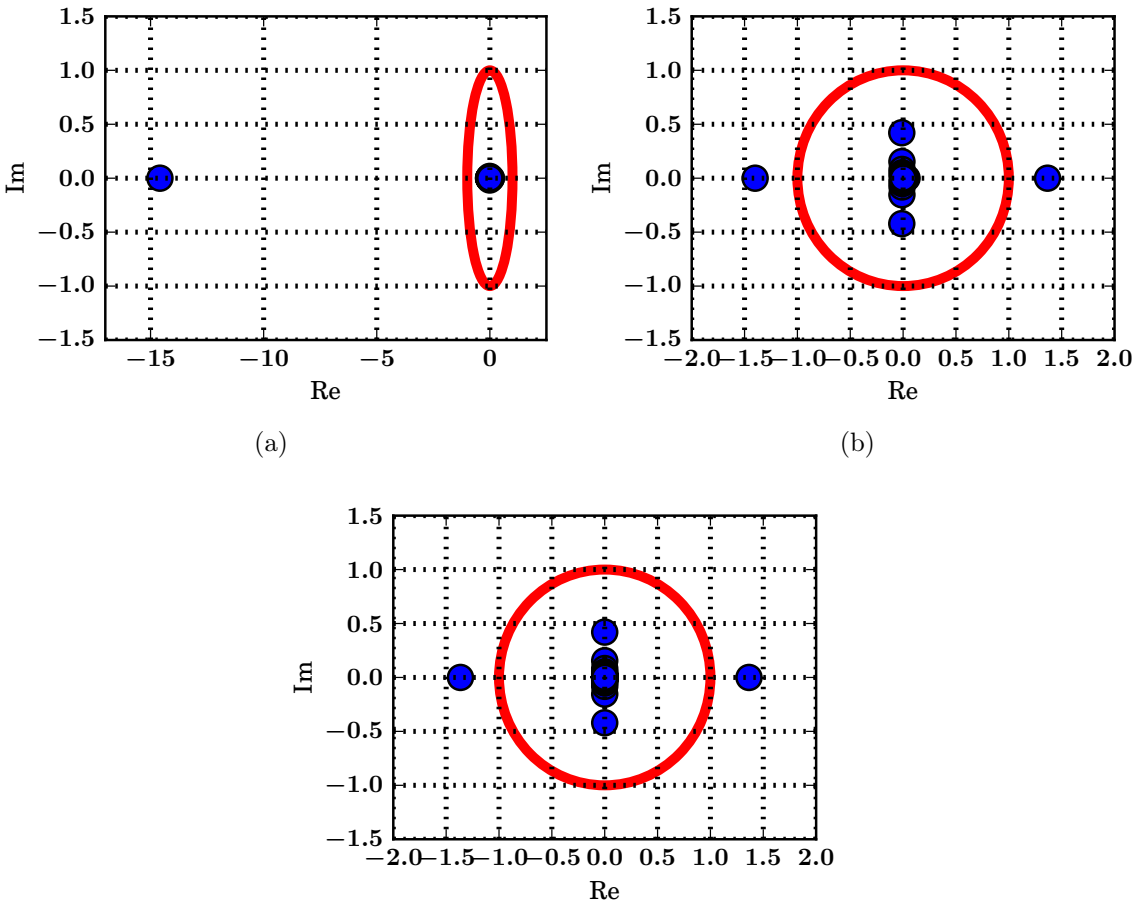

Figure 2.5: Eigenvalues of the iteration matrices for the a) Picard b) Field Split 1 and c) Field Split 2 approximations to the Jacobian. It is shown that if a time step of 10^{-9} s a few eigenvalues will be outside the convergence region (the red circle) and hence the methods will diverge. Note the two Field Split approximations are very similar.

Table 2.3: Time step required for all eigenvalues of the iteration matrices corresponding to the approximations to **J** defined in Eqs. (2.68) - (2.70) to have modulus less than one. The INC method converges in 6 iterations with a time step of 10^{-9}.

Approximation	Time Step Required for Convergence
Picard	$2 \cdot 10^{-12}$
Field Split 1	10^{-10}
Field Split 2	10^{-10}

2.3.2 Plane Strain Tension

To create a single material imperfection, the yield stress and yield strain was varied across the plate according to the smooth function β_{2D} (see Figure 2.6) so that

$$\sigma_{yield}\left(X_1, X_2\right) = \sigma_0 \beta\left(X_1, X_2\right) \tag{2.73}$$

$$\gamma_{yield}\left(X_1, X_2\right) = \gamma_0 \beta\left(X_1, X_2\right) \tag{2.74}$$

$$\beta_{2D}\left(X_1, X_2\right) = 1 - 0.04\left[sech\left(\frac{\sqrt{X_1^2 + X_2^2}}{5 \cdot 10^{-6}}\right)\right]^2 \tag{2.75}$$

This results in a weak spot at the center of the plate, which corresponds to the lower left corner of the modeled quadrant, upon which the shear band will nucleate. Figure 2.7 shows the σ_{22} vs the infinitesimal strain ϵ_{22} at the center of the plate. The INC scheme developed here converges quickly with refinement and is stable even at very large strains. Conversely, the split scheme shows very slow convergence, and additionally shows stability issues as localization becomes more severe. The plots show that at lower strains, the INC and split schemes give results that are very similar, however, as the system evolves the split scheme quickly diverges from the INC solution.

The reason for the stark differences in behavior is that the coupled method preserves the competition between heat conduction, which smooths temperature gradi-

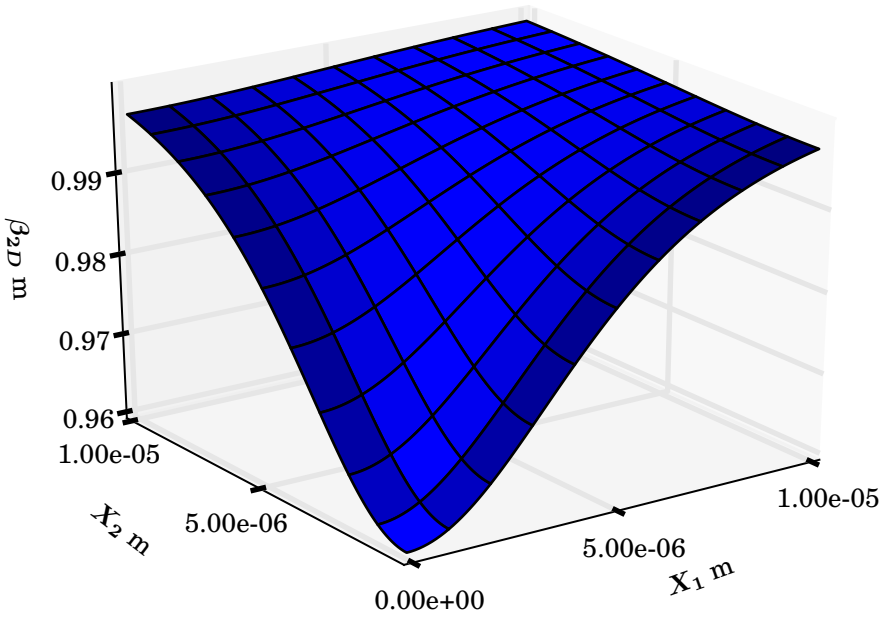

Figure 2.6: β_{2D} function defined by Eq. (2.75)

ents (and thus also stress and strain gradients through the coupling of the system), and heat production, which concentrates gradients. Due to this effect, any finite value of thermal conductivity will lead to the localization band evolving indefinitely, rather than showing a singularity [138] (However localization becomes stronger as the thermal conductivity is decreased and the response tends to a singularity as thermal conductivity tends to zero). Even with a very small value of thermal conductivity regularization is achieved, since the diffusion term becomes very large with strongly concentrated temperature gradients. Heat is thus removed from the shear band at a faster rate as the localization becomes stronger and a singular response is avoided. Split schemes such as the one described are not satisfactory because the coupling of fields is lost as the simulation progresses. Contributing to this is the fact that the function g (in Eq. 2.13) is very sensitive to small errors in temperature, leading to errors in the entire solution field. These errors accumulate as the system evolves

and cannot be recovered due to the history dependence of plasticity. Note that the split scheme will converge in the limiting case of infinitesimal time step, but convergence is so slow that for the practical choices of time step shown here, accuracy is unacceptably poor.

Assuming adiabatic conditions is not reasonable numerically since mesh sensitive results will be found, nor is it reasonable physically since the diffusive term and heat source term are of the same order of magnitude (Figure 2.9). Adiabatic conditions thus greatly over predict the rate of heating within the shear band, aside from eliminating the material nonlocality that results in a characteristic length.

Comparison of computational cost

CPU times for each method on the tension example are shown in Figure 2.10. Each of these computations were executed in FEAP version 8.2 [131] on a MacBook with a 2GHz Intel Core 2 Duo processor. The linear solver for the INC method is the PETSc version 2.3 sequential sparse direct LU decomposition routine [10]. Upon mesh refinement, the split method requires a smaller time step to meet the stability condition, adding a significant cost to the simulation. The INC method is not constrained by such a stability condition, although an arbitrarily large time step cannot be used since the Newton algorithm uses the converged values from the previous time step as the initial guess for the current time step. Thus the quadratic rate of convergence, or the convergence at all is not guaranteed. However in practice, Newton's method converges quickly for time steps several orders of magnitude larger than the critical time step of the split scheme (see for example Table 2.4). For example, 3-4 iterations are required with a time step of 10^{-8} s for a fully formed shear band.

Using the INC solution on the finest mesh, mesh 4, as a benchmark, the CPU time required to achieve a certain relative error can be computed. We define the error as the average of the relative errors of the effective stress, temperature, and equivalent

Table 2.4: Nonlinear Iterations and CPU times on the finest mesh for time step numbers 23, 32, and 130, which correspond to the onset of yield (stage I), the onset of softening (stage II), and a fully formed shear band (stage III), respectively. The time step is 10^{-8} s.

	Number of Nonlinear Iterations	CPU Time [seconds]	Cumulative CPU Time [seconds]
Stage I	7	26.13	228.97
Stage II	4	15.40	371.18
Stage III	3	11.84	1531.58

plastic strain taken at the lower left corner of the modeled domain, at $1.3\mu s$. This is plotted in 2.10 (b). Note that the highest level of resolution for the split method has higher error than that of the lowest level of resolution for the INC method. This translates to a reduction of cpu time by two orders of magnitude. Use of the split scheme has lead some authors to conclude that the type of constitutive law employed here is inappropriate for modeling behavior inside a shear band [102], and should only be used up to the point of shear band initiation. However, our results show the split scheme greatly under predicts the amount of plastic straining, suggesting this conclusion should be reinvestigated.

2.3.3 Plane Strain Shearing

In the plane strain shearing example, no material imperfection is used to trigger the shear band. The band is triggered by the stress concentration created by the boundary conditions. Figures 2.11 and 2.12 show that alignment sensitivity is present for both the split and INC methods since the shear band propagates more readily along element edges. This is due to limitations in the ability of the finite element interpolants to accurately approximate steep solution fields and gradients which occur in localization problems. The alignment sensitivity is less severe with the INC method and the Pian Sumihara quadrilateral, and it remains to be seen if this sensitivity can be eliminated completely using a combination of INC and some other choice of interpolation. For

example it has been noted by [85] that mesh free particle methods help in suppressing alignment sensitivity.

2.4 Conclusion

A mixed element formulation has been developed which couples the inelastic response to thermal diffusion. The strong form was discretized in time and the resulting nonlinear weak form was linearized to find a numerically consistent Jacobian. The Galerkin approximation was then used to obtain a fully discrete set of nonlinear algebraic equations and the corresponding Newton linearization. Implementation of the proposed algorithm yielded mesh insensitive results, owing to the fact that diffusion acts as a regularizing parameter. Since diffusion removes heat from the shear band at a faster rate when temperature gradients are steeper, a singular response is avoided and a physical length scale results. This can also be interpreted as a material nonlocality since the constitutive law at a certain point in the continuum depends on history variables in the vicinity of the point (not just at the point itself) through the diffusion operator. Mesh alignment sensitivity of the INC formulation is not eliminated completely, but the sensitivity is not as severe compared to explicit solvers. In the following chapter, this formulation is applied to the analysis of the energy absorption capability of friction stir welded aluminum joints. Chapter 4 extends this formulation to large deformations with remeshing.

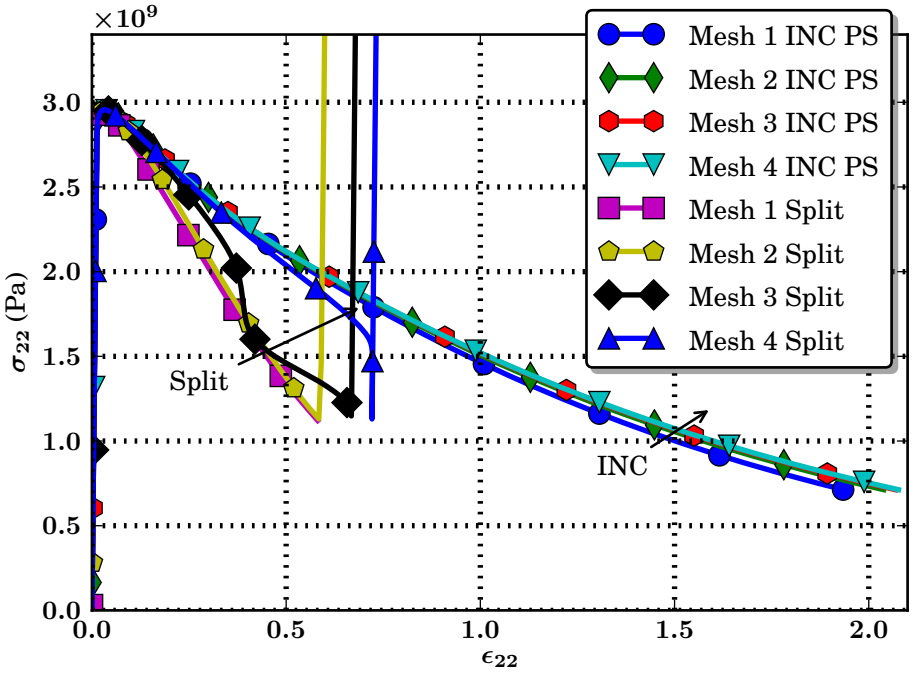

(a)

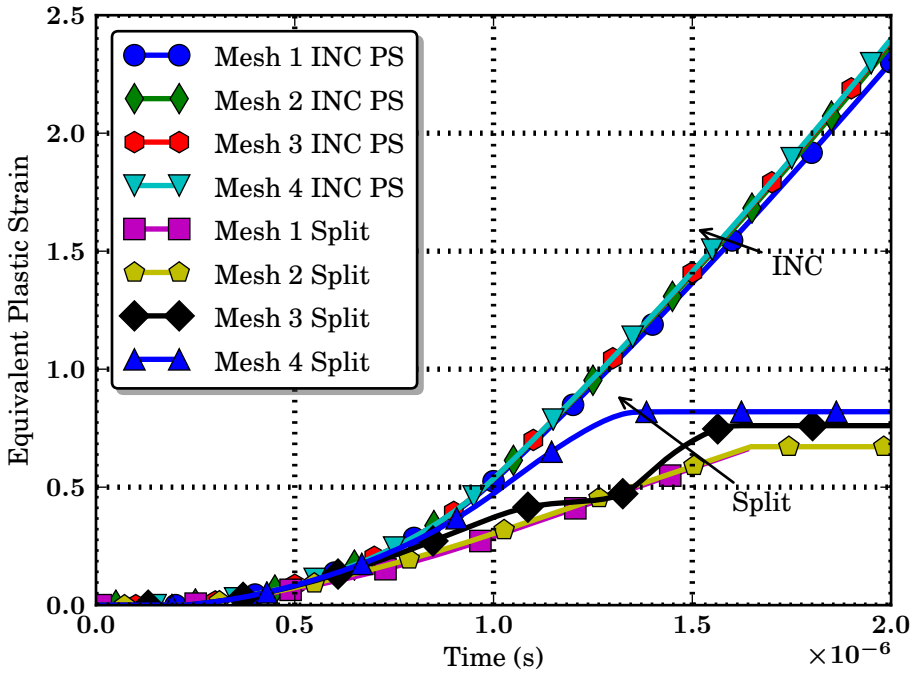

(b)

Figure 2.7: a) σ_{22} vs ϵ_{22} and b) Equivalent plastic strain vs time at the center of the plate. Only the Pian-Sumihara(PS) element and the split scheme are shown. The arrow indicates the direction of mesh refinement

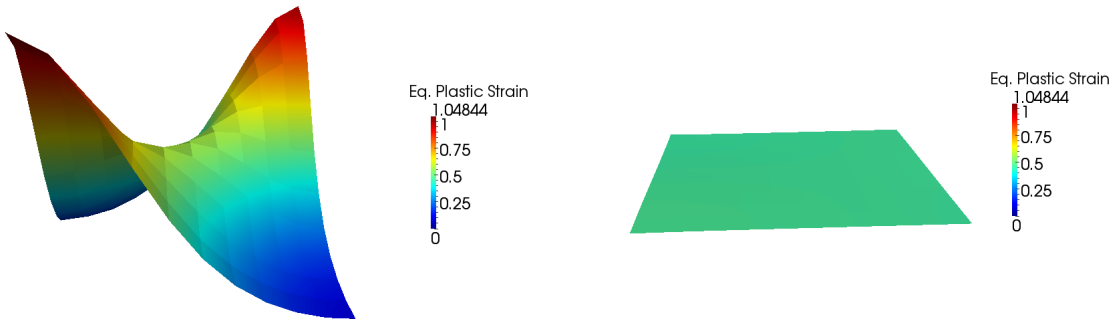

(a) Mesh 1 INC (b) Mesh 1 RTMM

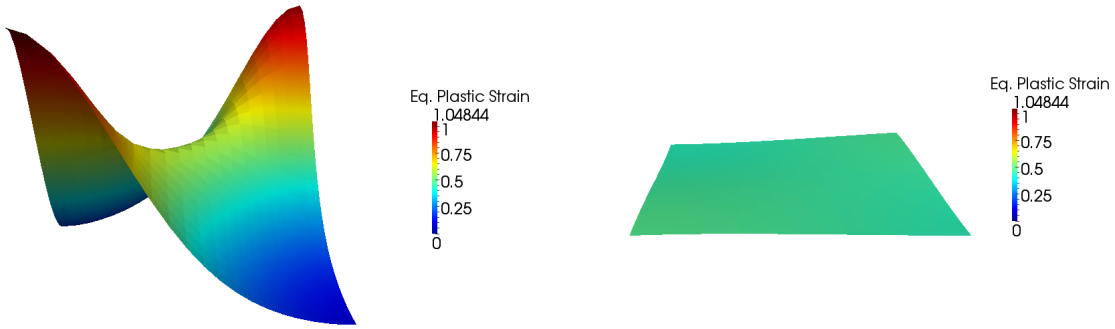

(c) Mesh 2 INC (d) Mesh 2 RTMM

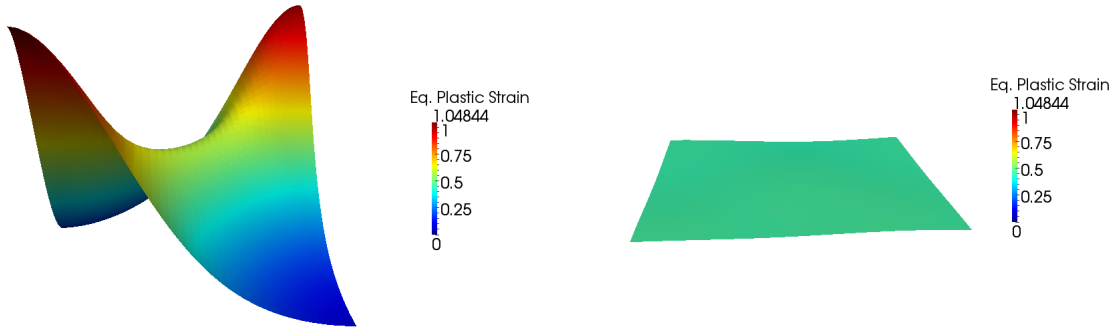

(e) Mesh 3 INC (f) Mesh 3 RTMM

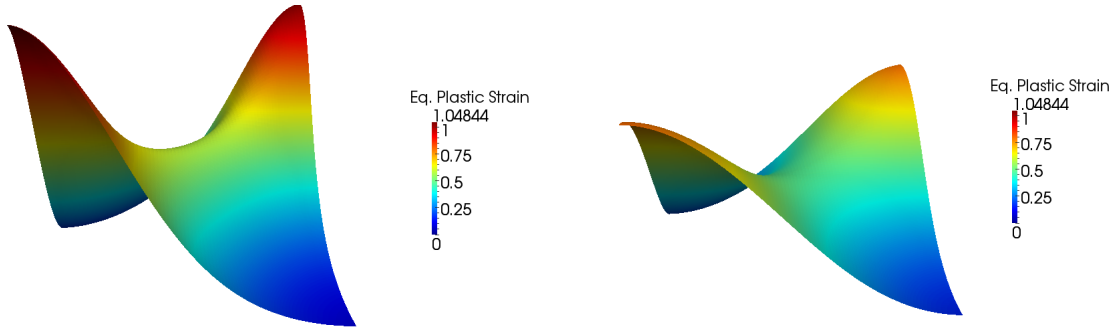

(g) Mesh 4 INC (h) Mesh 4 RTMM

Figure 2.8: Surface plots of the Equivalent plastic strain. For all plots, the simulation time is 1.3μs.

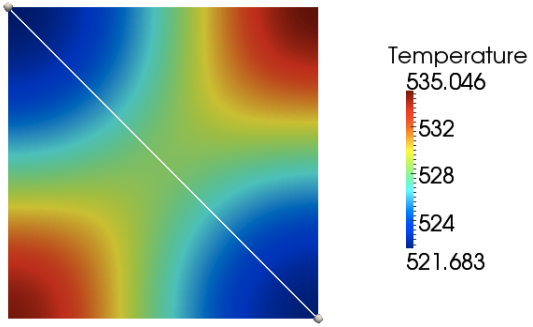

(b)

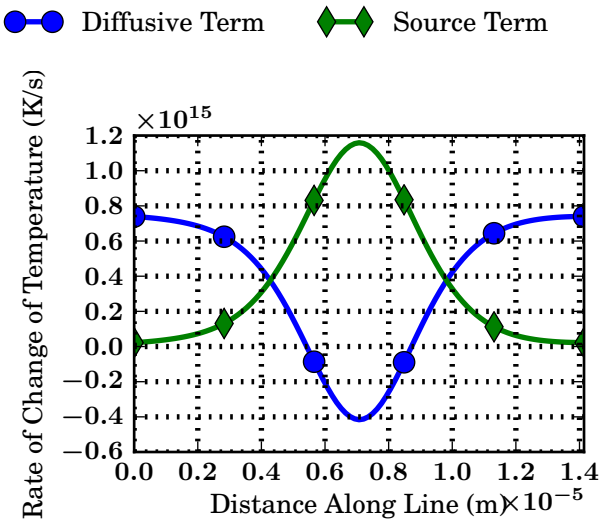

(c)

Figure 2.9: Comparison of the diffusive and source terms in the discrete energy equation (2.33) along the white line shown in a); $\mathbf{K_T}\hat{\mathbf{T}}^{\mathbf{n+1}}$ and $\mathbf{f_T}$ respectively. Note that the diffusive and source terms are the same order of magnitude within the shear band and thus assuming adiabatic conditions is not justified.

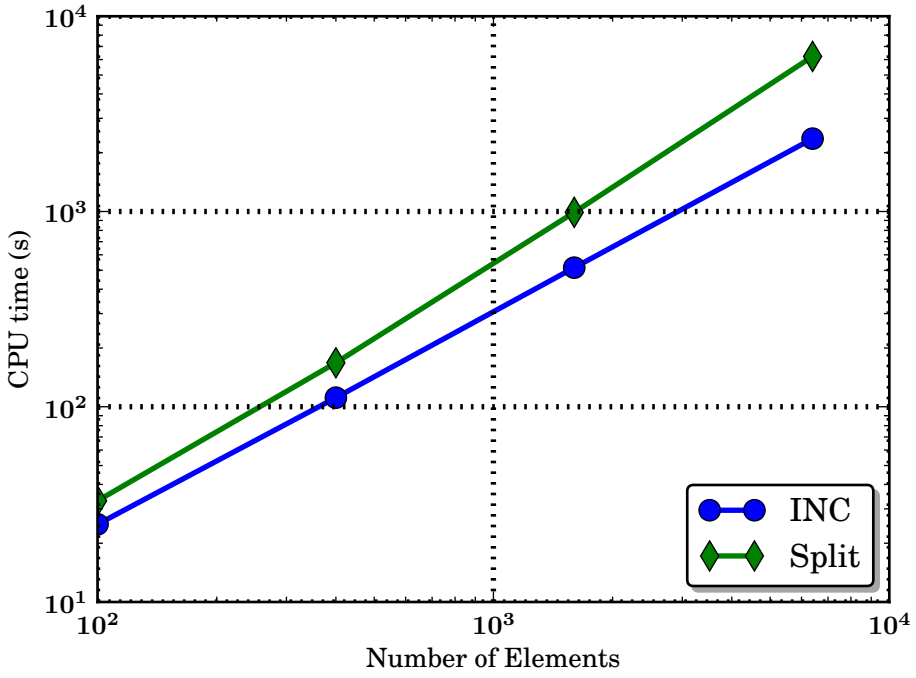

(a) CPU time vs number of elements

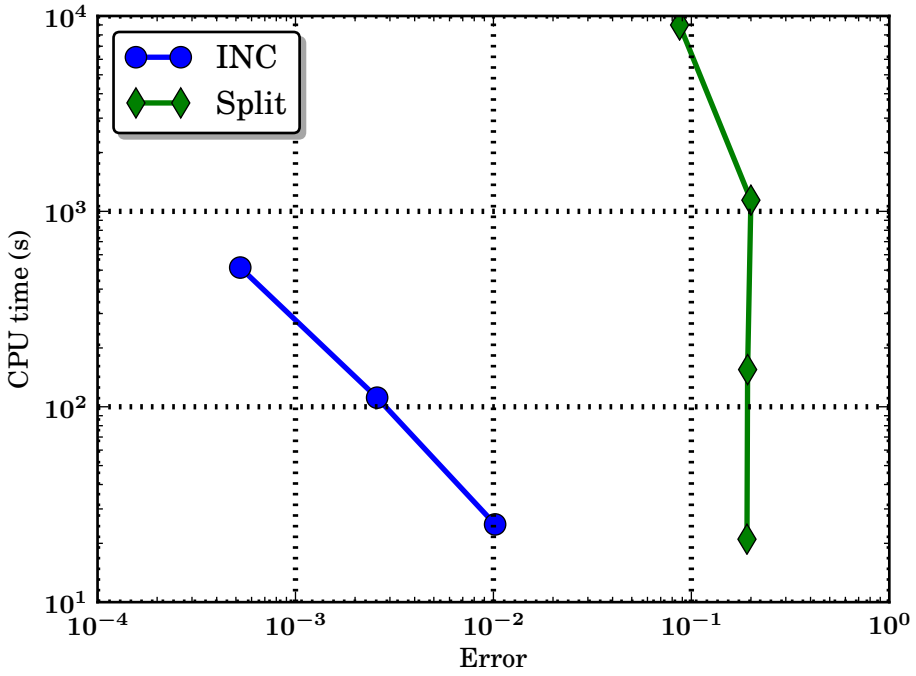

(b) CPU time vs error relative to INC solution on mesh 4

Figure 2.10: Performance Comparisons for the plane strain tension example.

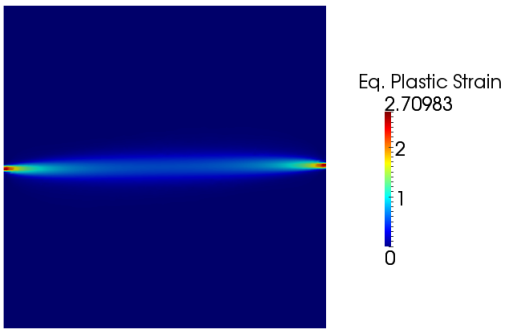

(a) Structured Mesh, INC

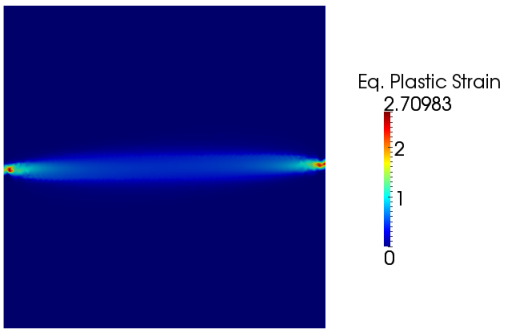

(b) Unstructured Mesh, INC

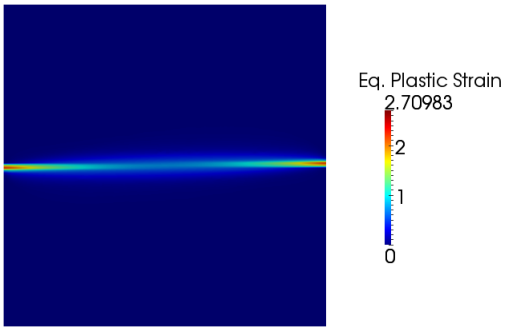

(c) Structured Mesh, RTMM

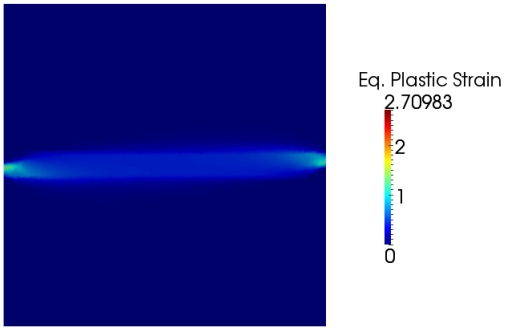

(d) Unstructured Mesh, RTMM

Figure 2.11: Plots of the equivalent plastic strain for the shearing example. The INC Method using the Pian-Sumihara quad is shown on the left and the split method is shown on the right. The time is 0.6μs.

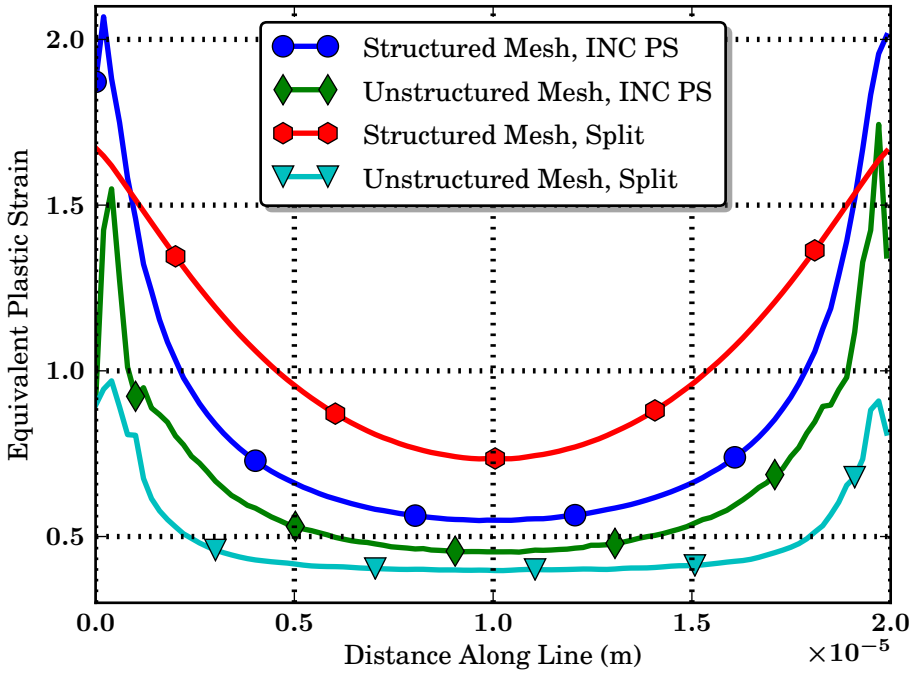

Figure 2.12: Equivalent plastic strain across the length of the shear band for the two methods and meshes. The time is 0.6 μs

Chapter 3

Application of the Monolithic Shear Band Solver to the Analysis of Friction Stir Welded Aluminum Joints Under High Rate Loading

High strength lightweight aluminum alloys offer potential advantages as replacements for traditional steels in many Army vehicles in terms of weight specific mechanical properties. Unibody chassis construction, as opposed to body on frame construction, is being pursued to lend enhanced rigidity to maintain structural integrity during potential under-body blast events. Since unibody construction requires the elimination of bolted joints, weldability of the chassis material is crucial. Alloys from the aluminum 2XXX and 5XXX series are notoriously difficult to weld with conventional techniques, but can be joined with Friction Stir Welding (FSW) [46].

FSW is a solid state joining process, which has recently been shown to be capable of producing joints in aluminum up to 3 inches thick [133, 135]. The FSW tool consists mainly of a shank, shoulder, and pin (shown in Figure 3.1), which rotate as

they advance, stirring the material together. Significant inelastic deformation, heat production, and dynamic recrystallization occur during this process, which results in the formation of several zones with distinct microstructure and material properties [89, 129, 134].

Figure 3.2 shows a cross-section of a typical FSW joint which illustrates the nature of these distinct material zones. The material zone most immediately surrounding the high-torque tool pin, inserted between the welded plates, is characterized by an upper and lower weld nugget. The upper and lower weld nuggets are zones B and A respectively in Figure 3.2. This comes both as a direct influence of the tool pin on the material grain structure as well as the thermal properties of the material and recrystallization processes. The tool shoulder creates a great deal of friction in contact with the plate surface during the FSW process which generates an inordinate amount of heat in comparison to the bottom of the plate. The difference in thermal inputs and boundary conditions thus creates a through thickness variation in recrystallization which leads to the distinct lower and upper weld nugget, marked as zones A and B, respectively in Fig. 3.2. Just outside of the weld nugget, zone C in Figure 3.2, is a third material zone which is still subject to both the mechanical and thermal influence of the FSW stirring pin. Further from the tool is a fourth material zone, too distant to be influenced by mechanical stirring, but still subject to thermal microstructural effects as heat is conducted away from the FSW joint during processing. This is known as the thermal affected zone and is marked by zone D in Figure 3.2 Computational modeling of the FSW process, aimed at numerically predicting the FSW joint zones, have been carried out by [62–64]. The importance of accounting for these variations must be noted, and they will play a significant role in the simulations below.

In this chapter, the physical and numerical formulation of chapter 2 is employed to model high rate loading of a small cross section of a stir welded joint. The goal is to develop a predictive capacity for energy absorption and failure of FSW joints in

dynamic loading, as well as to gain an understanding of the relationship between an FSW joint microstructure and the resulting energy absorption capability and failure strain.

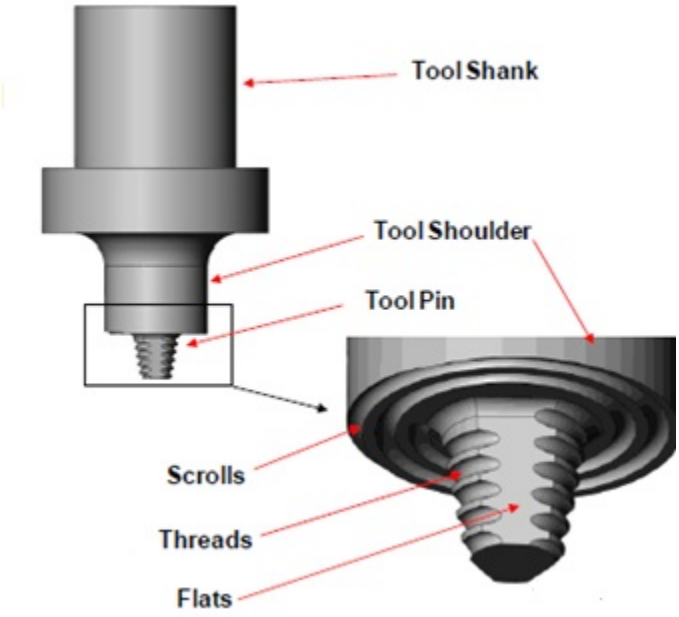

Figure 3.1: FSW tool. The tool shoulder is butted against the workpiece and the tool is rotated as it advances. This process mechanically stirs the workpiece metals together at elevated temperature, but without melting.

3.1 Model Configuration for FSW Joint Simulation

A symmetric model of the FSW joint has been created, as seen in Figure 3.3, which also shows the loading configurations tested. The model accounts for property variations in each FSW zone as shown in Table 3.1. These parameters were fit from the experimental data by [78, 79]. The stir weld process involves extensive inelastic deformation as well as dynamic recrystallization in the upper weld nugget. Due to the recrystallization, the grain size in the upper nugget is larger than that of lower nugget. However, contrary to expectation given the grain size in the respective regions, the

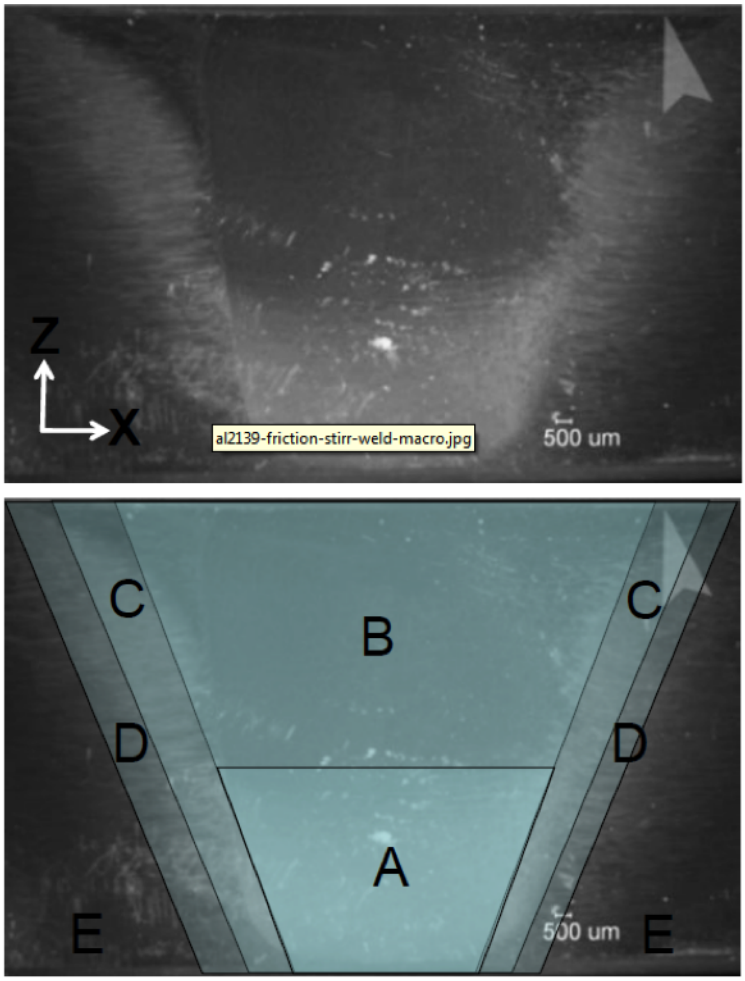

Figure 3.2: FSW Cross section. The labeled areas correspond to different weld zones which have distinct microstructural and mechanical properties. Zone A is the lower weld nugget, B the upper weld nugget, C the thermo-mechanical affected zone, and D the thermal affected zone.

experimental data show that the upper weld nugget has a higher yield strength than the lower weld nugget. It is suspected that the reason for this is a higher dislocation density in the upper nugget [141]. At present, transmission electron microscopy which could confirm this hypothesis is not available, but this is not crucial to the numerical results presented here.

The 5 mm by 5 mm region includes the key region of interest with greatest property mismatches and potential for failure initiation. Dynamic loading using a velocity boundary condition was employed to simulate the major components of a blast event,

Zone Name	Yield Stress (Pa)	Hardening Parameter
Unaffected Aluminum	414E6	0.05
Lower Weld Nugget	250E6	0.05
Upper Weld Nugget	300E6	0.01
Thermo-Mechanical Affected Zone	274E6	0.05

Table 3.1: Material Properties for the Weld Zones

Configuration Name	Zone 1	Zone 2	Zone 3
Stir Weld (SW)	Upper Weld Nugget	Lower Weld Nugget	TMAZ
Lower Nugget (LN)	Lower Weld Nugget	Lower Weld Nugget	Lower Weld Nugget
Unaffected Aluminum (UA)	Unaffected Al	Unaffected Al	Unaffected Al

Table 3.2: Material Properties for the problem configurations. See also Figure 3.3.

i.e. in-plane tension, through-thickness compression, and transverse shear, as illustrated in Figure 3.3. Two loading rates of 1E3 s^{-1} and 1e4 s^{-1} were investigated. By way of comparison to the actual FSW material configuration (referred to as "SW" in all results to follow), a region of uniform monolithic untreated aluminum material was tested (referred to as "UA"). Further, as the lower weld nugget possesses the nominally weakest material properties of the FSW joint, a test case investigating a region of uniform aluminum with lower weld nugget properties was investigated (referred to as "LN"). The purpose of this is to further gauge the effect of non-uniformity in the material properties of the weld joint on the energy absorption.

The graphs in the following section show two measures of energy absorption by the part, the rate of strain energy, ($\dot{\mathcal{W}}$) and the strain energy ($\mathcal{W}$). These quantities are integrated over the part so that

$$\dot{\mathcal{W}}(t) = \int_V \sigma_{ij} d_{ij} dV \tag{3.1}$$

$$\mathcal{W}(t) = \int_0^t \dot{\mathcal{W}}(\tau)\, d\tau \tag{3.2}$$

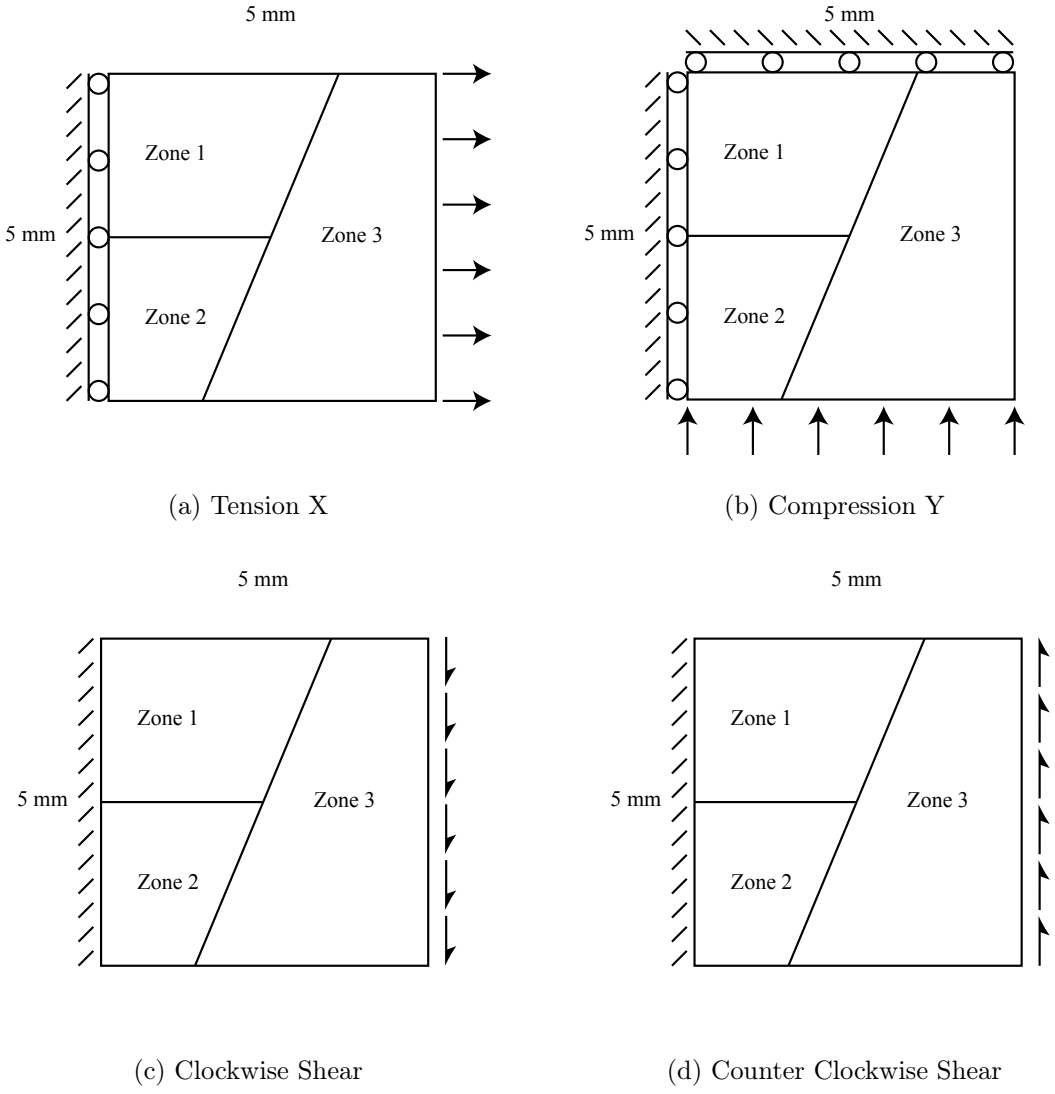

(a) Tension X

(b) Compression Y

(c) Clockwise Shear

(d) Counter Clockwise Shear

Figure 3.3: Problem configurations showing boundary conditions and weld zones.

where, V is the volume element, t is time, σ_{ij} is the stress and d_{ij} is the rate of deformation. $\dot{\mathcal{W}}$ at a given time, can be interpreted as the rate at which the part is storing energy.

Following the experimental work of Marchand and Duffy [96], shear band formation occurs in three stages. Stage 1 consists of homogeneous deformations, and includes the linear elastic range, yielding point, and the inelastic strain hardening range. Stage 2 occurs after the stress has passed through a peak, leading to initial strain softening that corresponds to localized deformations, and is often referred to

as localization. Stage 3, also known as stress collapse, is marked by significant strain softening and precipitous drop in the load carrying capability of the material, leading to strong localization and intense plastic deformation associated with shear bands. Note that it is possible for Stage 3 deformations to develop at a material point, or neighborhood of material points while the joint has reserve capacity. Since our main concern here is the energy absorption capacity of the joint as a whole, we define global failure when $\dot{\mathcal{W}}$ drops below 90% of its peak value, which indicates the material has lost significant ability to dissipate energy. The capacity of the material is then defined as $\mathcal{W}$ at failure. Since $\dot{\mathcal{W}}$ is a volume averaged quantity, it represents a global failure criterion. It is also of interest to identify from which weld zone or zone interface failure originates. For this purpose, identification of Stage 3 deformations as a local failure criterion is also useful. In the results below, this information is tabulated showing the nominal strain and $\mathcal{W}$ at global failure, using the criterion $\dot{\mathcal{W}}(t) \leq 0.9 \max \dot{\mathcal{W}}(t)$. In addition, the failure origin is noted by determining which area of the weld is the first to enter Stage 3 deformation.

3.2 Results

3.2.1 Cross weld tension

Results of the cross weld tension simulations (see Figure 3.3a) at two different strain rates are shown below in Figures 3.4-3.5. Figure 3.4 shows characteristic contour plots of equivalent plastic strain at the time of failure, and Von-Mises stress at the time of peak $\dot{\mathcal{W}}$. Contour plots are shown side by side for a uniform region of untreated aluminum followed by a plot of the simulated weld zone region in Figure 3.4. The shear band pattern for the UA and SW cases are clearly different, with the shear band in the SW case being contained entirely in zones 1 and 2. For the stir weld case, Yielding is first observed in the zone 2, which corresponds to the lower weld nugget. Localization is also first observed in this zone, but shear band initiation, as indicated by a precipitous drop in the local stress level during loading, originates from the upper weld nugget. This behavior is observed for both loading rates in the numerical simulation. Quasi static experiments on FSW samples were reported in [78, 79]. They concluded that the failure origin zone would be determined by which zone reaches strain hardening saturation first and in the quasi static case, this was found to be the LN. The dynamic case is somewhat more complicated, with rate effects and thermal softening being present. Strain hardening saturation is not an adequate indicator for failure because strain softening and localization does not necessarily imply failure, which has been noted in the experimental work of Marchand and Duffy [96], and is evident in the numerical results presented here. The nominal strain to failure, strain energy at failure, and the zone in which failure initiates, as shown in Table 3.3.

Perhaps the most important feature of Figure 3.4 is the buildup of stresses that occur near the material zone boundary. This is essentially an interfacial stress directly due to the material inhomogeneity and property mismatch, which leads to failure of the SW joint at lower strains compared to the unaffected aluminum. This effect

leads to significant differences in the overall stress strain response of the joint, which is shown in Figure 3.5, where the domain averaged stress σ_{22} is plotted against the nominal strain. The oscillations present in these plots are due to elastic wave reflections, which are damped quickly by plastic deformation. This illustrates that in an averaged sense, the FSW joint is marginally stronger than the lower weld nugget, but at the cost of significant ductility, failing at less than half the nominal strain of the untreated aluminum. The loss of mechanical capacity of the weld can clearly be seen in comparing the FSW weld performance (SW) to that of unwelded aluminum (UA) in Figure 3.6. The FSW joint fails at approximately 5 times lower mechanical energy for the strain rate of 1E3 s^{-1} and 3 times lower for the rate of 1E4 s^{-1}, due both to softening (and lower initial rate of strain energy) and a lower strain capacity before failure initiation see Table 3.3. Though thermo-mechanical property degradation due to FSW processing clearly weaken the FSW joint strength, it is readily apparent that inhomogeneity of the joint and interfacial stress risers are the key drivers for loss of mechanical capacity. This is evidenced by the fact that if the entire region were comprised of the nominally weakest material of the lower weld nugget, this would still outperform the actual FSW. This comparison is clearly seen in Figure 3.6, in which the rate of strain energy is comparable, yet the duration of significant energy absorption prior to failure is much larger for monolithic LN material as compared to the actual FSW joint. The reduction in energy absorption at the strain rate of 1E3 s^{-1} is greater than the reduction at the strain rate 1E4 s^{-1}. This indicates that the effect of material inhomogeneity decreases with increasing strain rate. This is due to the fact that the material zones have the same rate hardening characteristics, which become increasingly prevalent relative to the inhomogeneous strain hardening characteristics as the applied strain rate increases.

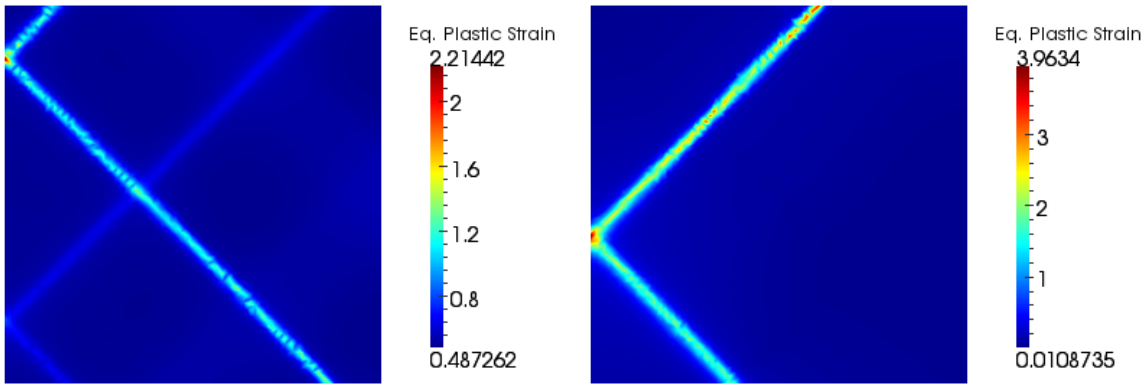

(a) Unaffected Aluminum at failure, Nominal Strain Rate 1E3

(b) Stir Weld at failure, Nominal Strain Rate 1E3

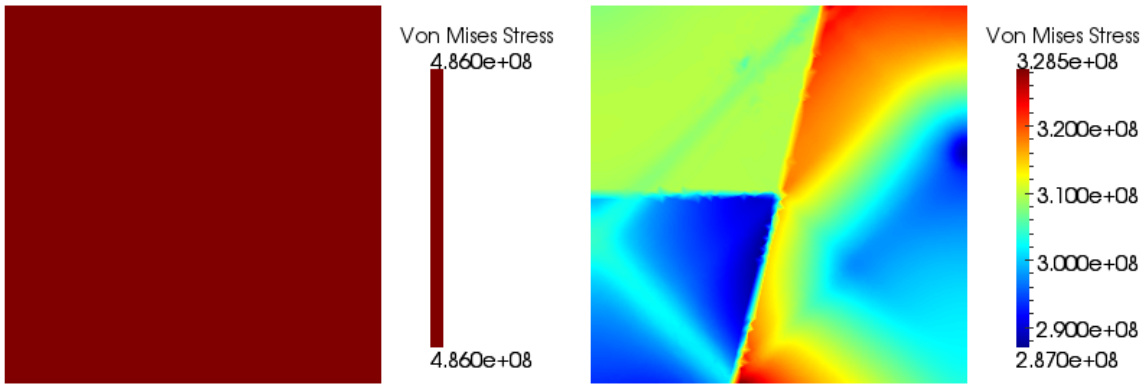

(c) Unaffected Aluminum at peak $\dot{\mathcal{W}}$, Nominal Strain Rate 1E3

(d) Stir Weld at peak $\dot{\mathcal{W}}$, Nominal Strain Rate 1E3

Figure 3.4

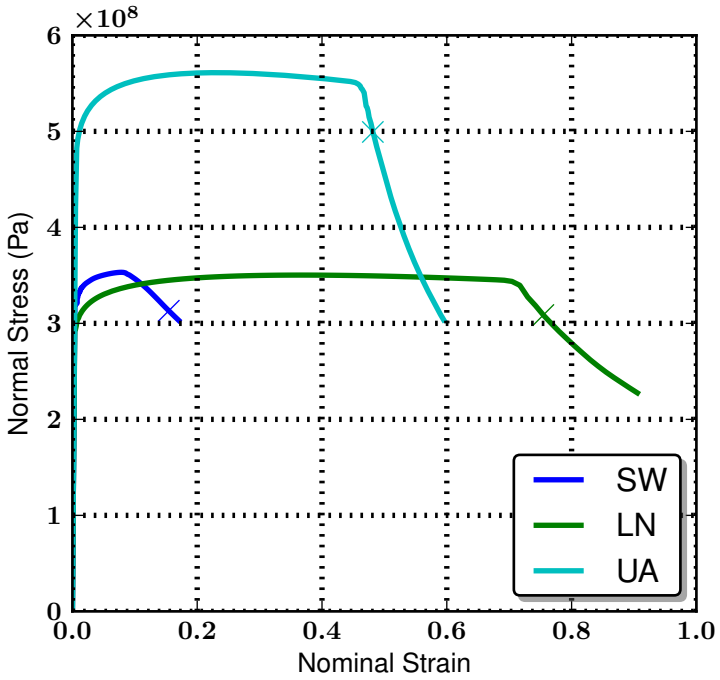

(a) Tensile Stress in the Direction of Loading, Nominal Strain Rate 1E3

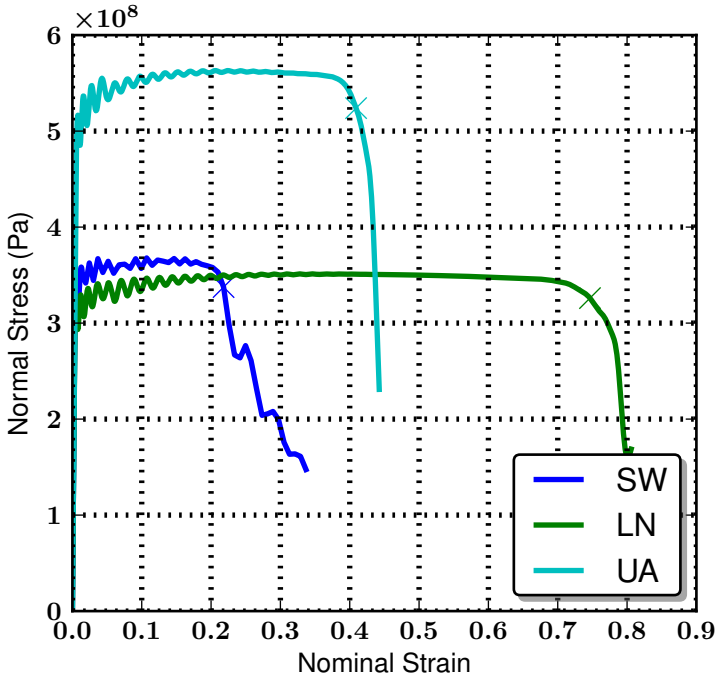

(b) Tensile Stress in the Direction of Loading, Nominal Strain Rate 1E4

Figure 3.5: Domain averaged tensile stress in the direction of loading vs nominal strain for each loading case. The x on the plot indicates the failure point.

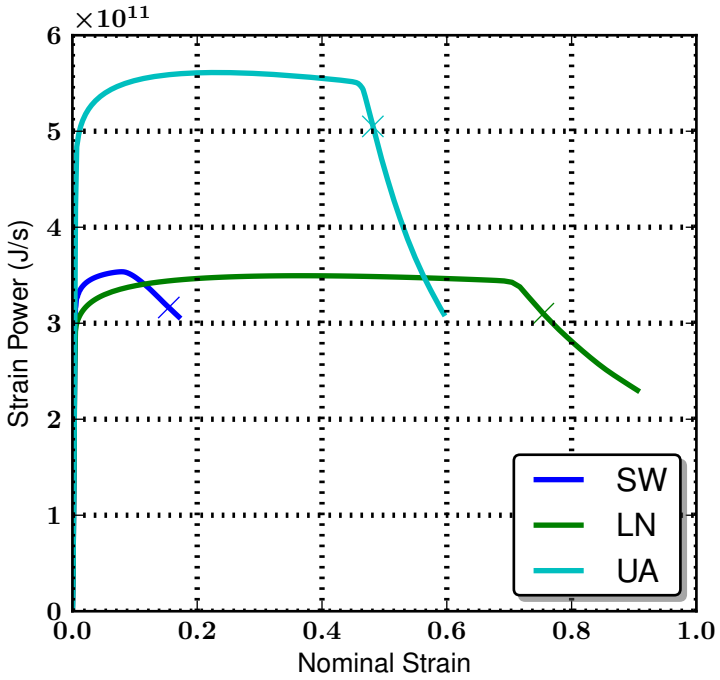

(a) $\dot{\mathcal{W}}$, Nominal Strain Rate 1E3

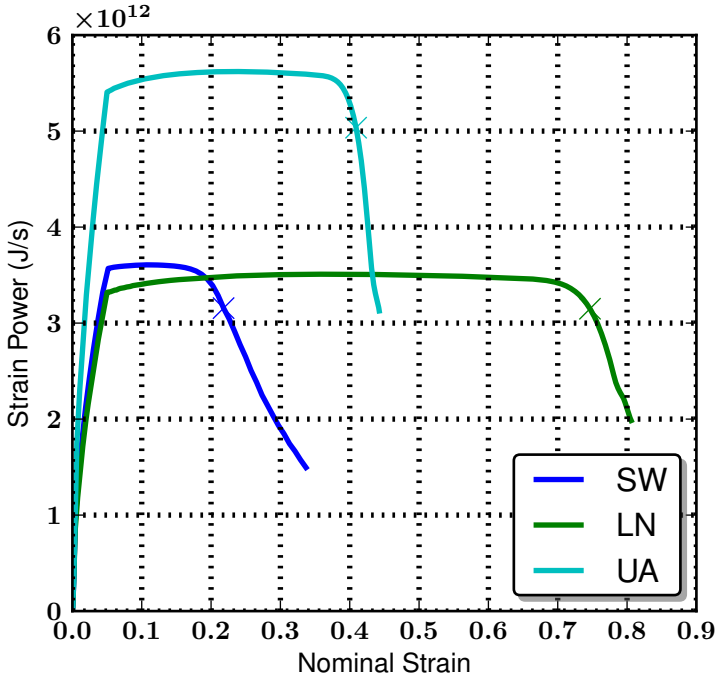

(b) $\dot{\mathcal{W}}$, Nominal Strain Rate 1E4

Figure 3.6: Rate of stress working for each case. The x on the plot indicate the failure point

Load Config. →	Cross Weld Tension		
Nom strain rate →	1E3		
Mat Config. ↓	Nom. Failure Strain	$\mathcal{W}$ at Failure	Failure Origin
UA	0.48	2.64e+08	N/A
LN	0.75	2.58e+08	N/A
SW	0.15	5.23e+07	UN-TMAZ Interface
Nom strain rate →	1E4		
Mat Config. ↓	Nom. Failure Strain	$\mathcal{W}$ at Failure	Failure Origin
UA	0.41	2.24e+08	N/A
LN	0.75	2.57e+08	N/A
SW	0.22	7.62e+07	UN-TMAZ Interface

Table 3.3: Results summary for the cross weld tension test: nominal strain at failure, $\mathcal{W}$ at failure, and failure initiation zone ae tabulated

3.2.2 Through thickness compression

The through-thickness compression test cases, illustrated in Figure 3.3b, again evidence the distinctive features of strain localization and shear band formation. The exact morphology of the shear bands and resulting stress field are quite different for this different loading case. As was observed for the cross weld tension case, yielding and localization are first observed in the LN of the stir weld. Additionally, the trend that increasing the strain rate slightly mitigates the loss in energy absorption is also observed. However, in the compression test, failure originates from the point where the UN, LN, and TMAZ meet. Despite these differences, the trends shown in the stress strain curves in Figure 3.8 are very similar to that of the tensile case, where the FSW experiences a loss significant loss of ductility due to stress risers at the material interfaces. The traces of rate of strain energy in Figure 3.9 are also relatively similar, likely due to the fact that both loading cases are driven by normal strains as applied at the macro level. More quantitatively, Table 3.4 shows that while a significant reduction occurs in both the strain to failure and the energy capacity, the reduction is not as severe as it was in the cross weld tension case.

Load Config. $\rightarrow$	Through Thickness Compression		
Nom strain rate $\rightarrow$	1E3		
Mat Config. $\downarrow$	Nom. Failure Strain	$\mathcal{W}$ at Failure	Failure Origin
UA	0.54	2.88e+08	N/A
LN	0.84	2.87e+08	N/A
SW	0.33	1.19e+08	UN-LN-TMAZ Point
Nom strain rate $\rightarrow$	1E4		
Mat Config. $\downarrow$	Nom. Failure Strain	$\mathcal{W}$ at Failure	Failure Origin
UA	0.53	2.91e+08	N/A
LN	0.83	2.85e+08	N/A
SW	0.46	1.67e+08	UN-LN-TMAZ Point

Table 3.4: Results summary for the through thickness compression test: nominal strain at failure, $\mathcal{W}$ at failure, and failure initiation zone ae tabulated

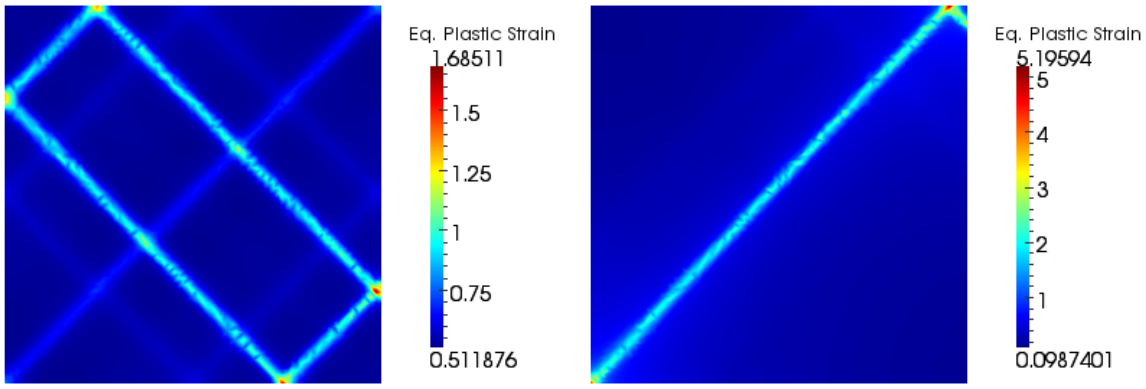

(a) Unaffected Aluminum at failure, Nominal Strain Rate 1E3

(b) Stir Weld at failure, Nominal Strain Rate 1E3

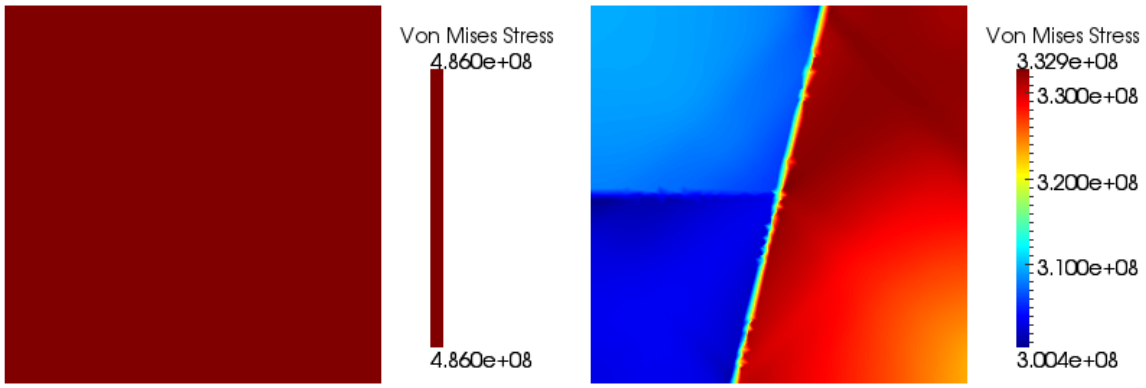

(c) Unaffected Aluminum at peak $\dot{\mathcal{W}}$, Nominal Strain Rate 1E3

(d) Stir Weld at peak $\dot{\mathcal{W}}$, Nominal Strain Rate 1E3

Figure 3.7

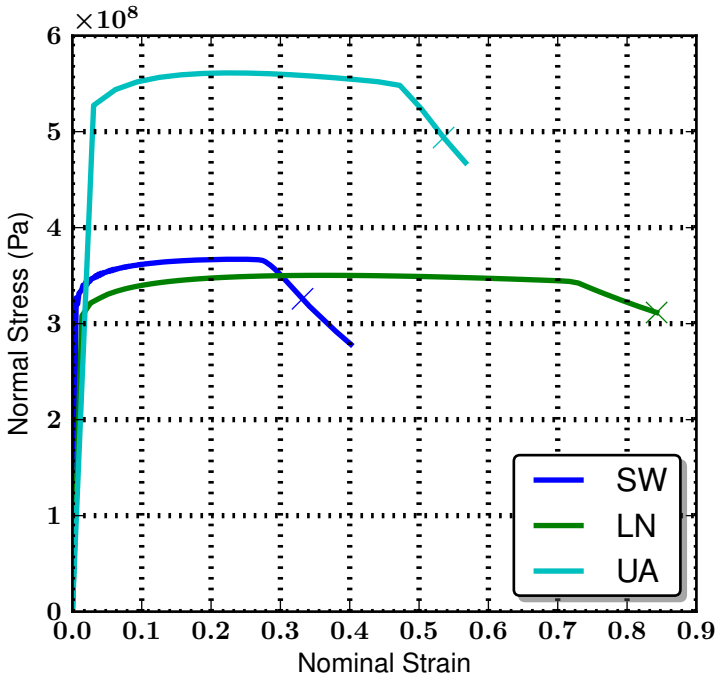

(a) Compressive Stress in the Direction of Loading, Nominal Strain Rate 1E3

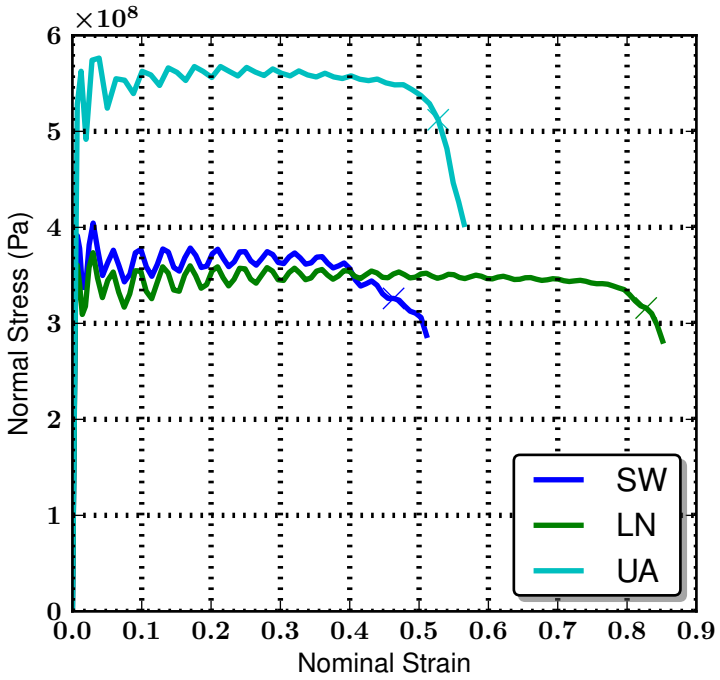

(b) Compressive Stress in the Direction of Loading, Nominal Strain Rate 1E4

Figure 3.8

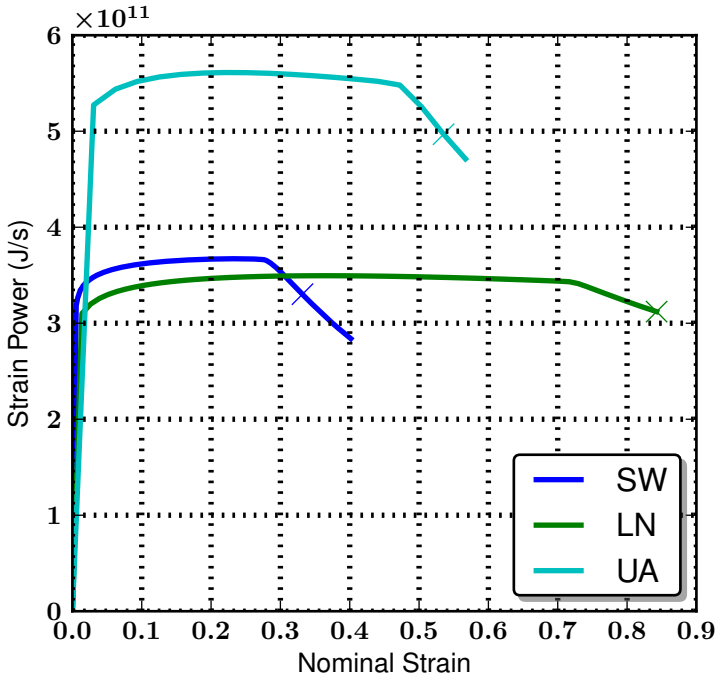

(a) $\dot{\mathcal{W}}$, Nominal Strain Rate 1E3

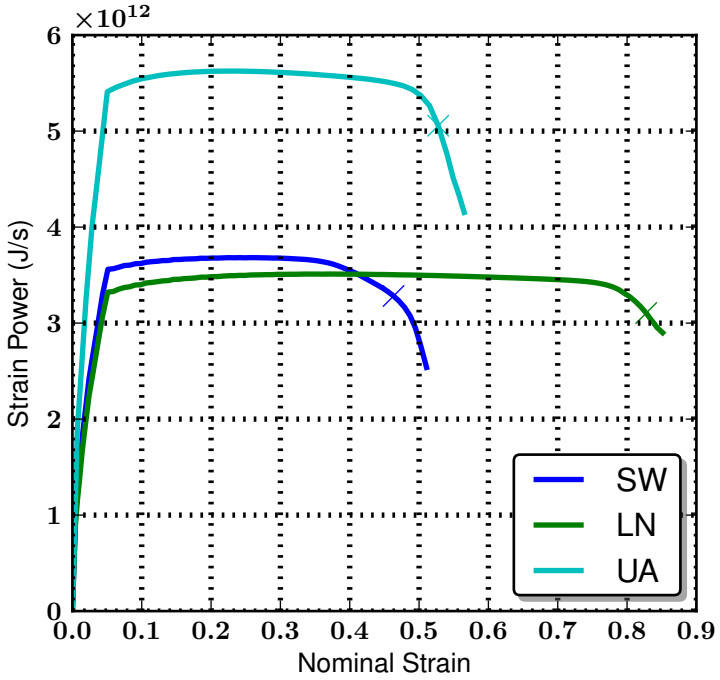

(b) $\dot{\mathcal{W}}$, Nominal Strain Rate 1E4

Figure 3.9: Rate of stress working for each case. The x on the plot indicate the failure point

3.2.3 Shear loadings

The FSW geometry is asymmetric, and therefore two cases of "clockwise" and "counterclockwise" shear loading have been investigated. Both clockwise and counterclockwise cases produce very similar results both qualitatively and quantitatively, so only the clockwise shear case is shown. Here, we observe that the strength reduction due to the weld zones is much smaller than the normal loading cases, see Table 3.5. This is due to the loading conditions producing high stress concentrations on the upper and lower left corners of the weld, which are not adjacent to any material interface. The stress concentrations produced at the material interfaces are thus less significant than those produced due to the loading configuration; note the similar Von Mises stress contour in Figure 3.10. In other words, we observe a failure which is localized within a specific zone, in contrast to the normal loading cases where failure involved strong interaction between zones resulting in failure initiation at the zone interface. This is further evidenced by the shear stress response shown in Figure 3.11 and the rate of strain energy plot in Figure 3.12. The overall trends of the normal loading cases are reproduced, but the final results are much less drastic, with a slight reduction in capacity being present for the FSW joint.

Load Config. $\rightarrow$	Clockwise Shear		
Nom strain rate $\rightarrow$	1E3		
Mat Config. $\downarrow$	Nom. Failure Strain	$\mathcal{W}$ at Failure	Failure Origin
UA	0.36	7.30e+07	N/A
LN	0.72	1.09e+08	N/A
SW	0.51	6.86e+07	UN
Nom strain rate $\rightarrow$	1E4		
Mat Config. $\downarrow$	Nom. Failure Strain	$\mathcal{W}$ at Failure	Failure Origin
UA	0.17	3.37e+07	N/A
LN	0.29	3.66e+07	N/A
SW	0.20	2.48e+07	UN

Table 3.5: Results summary for the clockwise shear test: nominal strain at failure, $\mathcal{W}$ at failure, and failure initiation zone ae tabulated

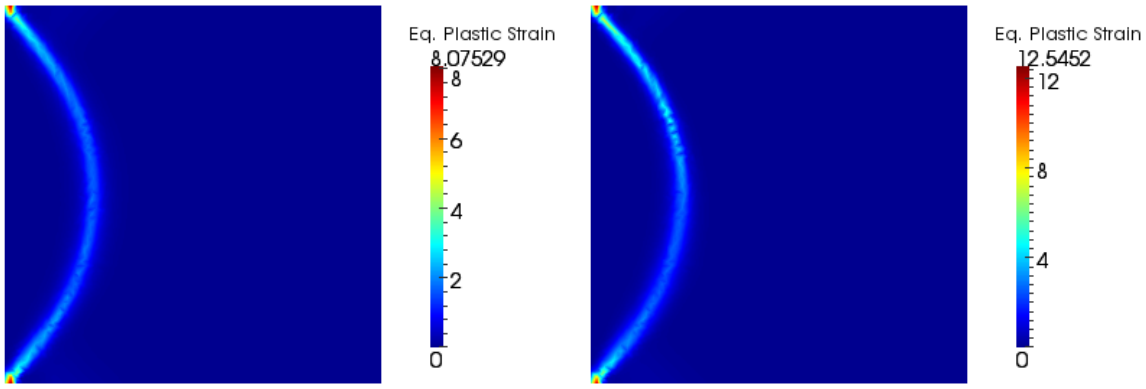

(a) Unaffected Aluminum at failure, Nominal Strain Rate 1E3

(b) Stir Weld at failure, Nominal Strain Rate 1E3

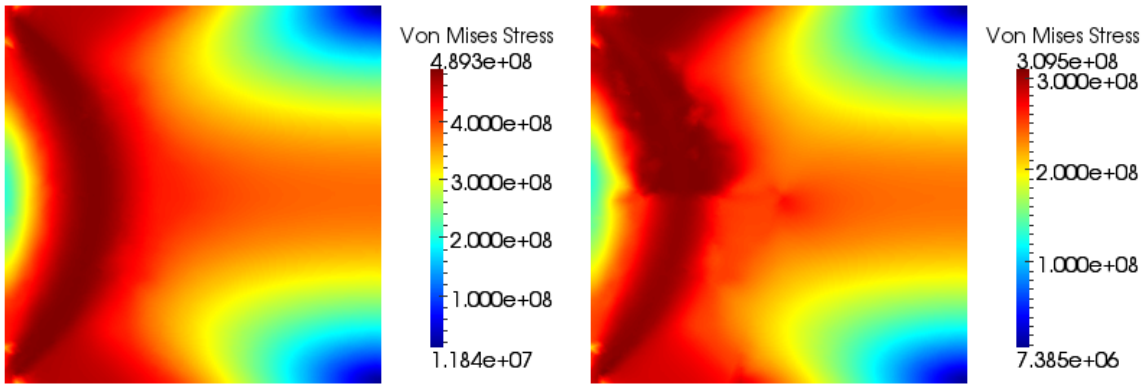

(c) Unaffected Aluminum at peak $\dot{\mathcal{W}}$, Nominal Strain Rate 1E3

(d) Stir Weld at peak $\dot{\mathcal{W}}$, Nominal Strain Rate 1E3

Figure 3.10: Surface plots for the shear loading case

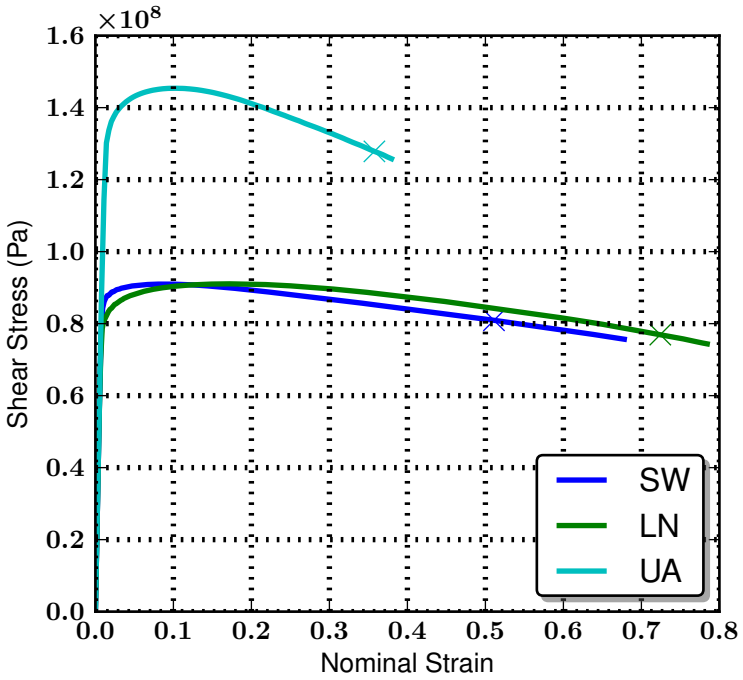

(a) Shear Stress, Nominal Strain Rate 1E3

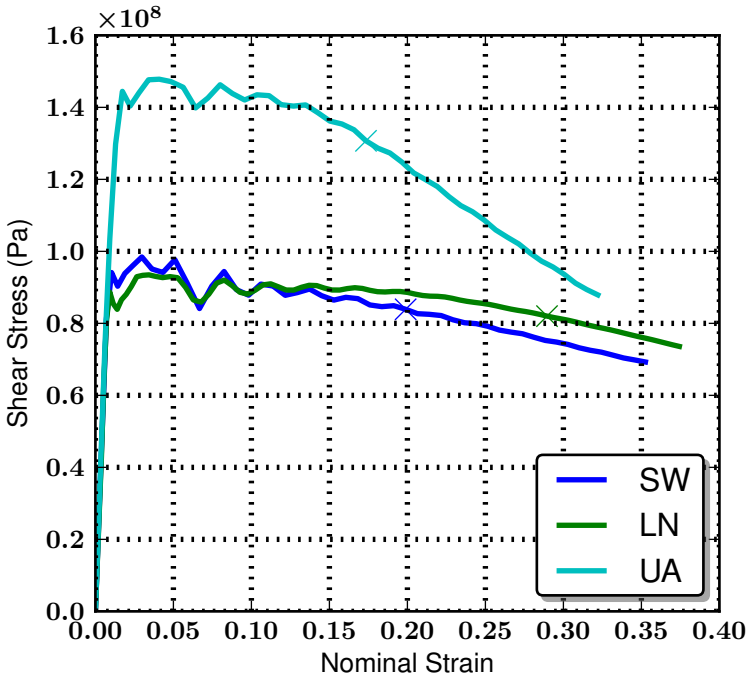

(b) Shear Stress, Nominal Strain Rate 1E4

Figure 3.11

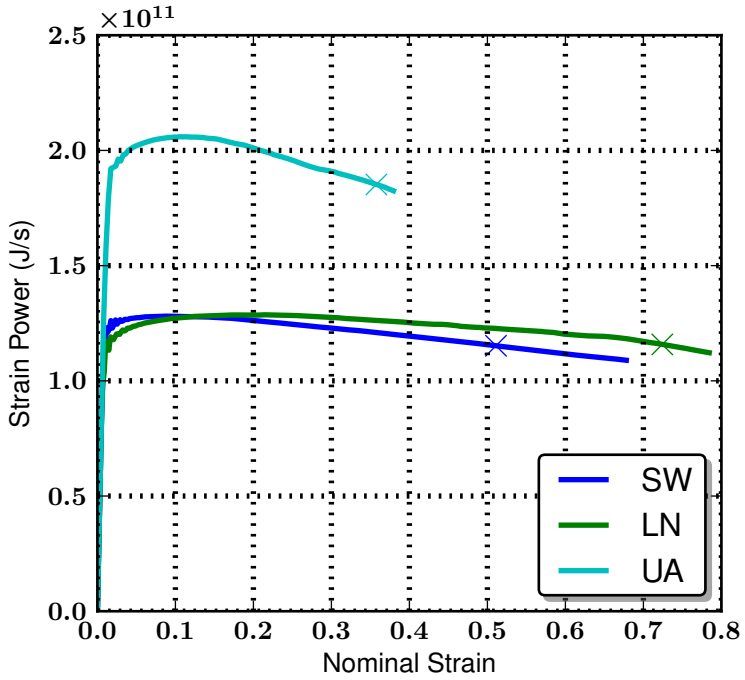

(a) $\dot{\mathcal{W}}$, Nominal Strain Rate 1E3

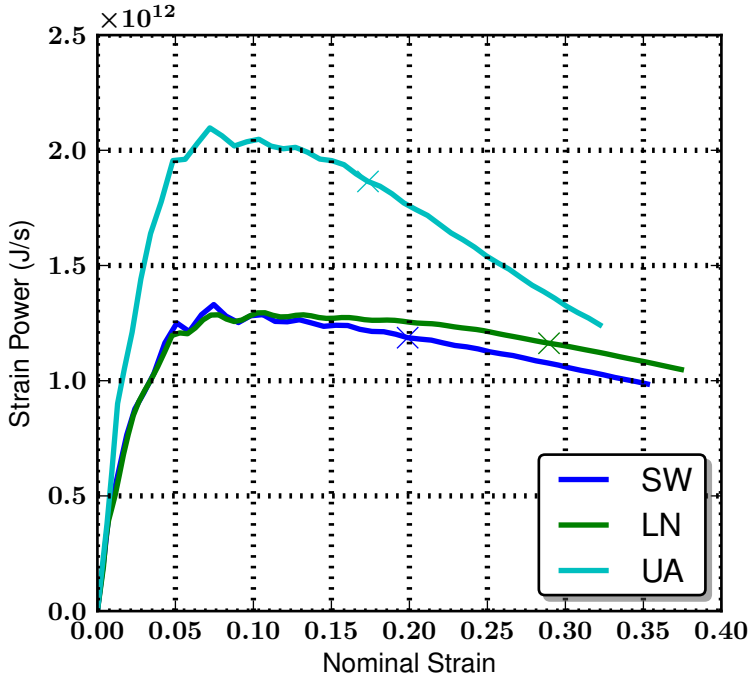

(b) $\dot{\mathcal{W}}$, Nominal Strain Rate 1E4

Figure 3.12: Rate of stress working for each case. The x on the plot indicate the failure point

3.3 Conclusion

We have investigated Friction Stir Welded (FSW) joint under various high strain rate loading conditions using a thermal softening, rate dependent plasticity model. The model accounts for thermal diffusion which regularizes the problem in the softening region and is solved using a monolithic, (also known as implicit nonlinearly consistent, or simultaneous) nonlinear solver. As a benchmark, the loading cases were also run with the uniform material properties of the untreated aluminum (UA), and of the lower weld nugget (LN), which is nominally the weakest constituent of a FSW joint. Calculation of the strain to failure and strain energy at failure show decreased ductility and energy absorption capacity for FSW joint in comparison to the UA and LN cases. This is due to the mismatch of inelastic material properties, namely the yield stress and hardening properties of the material zones. Such a mismatch lead to stress risers which cause early failure.

Two factors were found to mitigate the effect of the material mismatch, the first of which was increasing the strain rate. Since this leads to an increased prevalence on strain rate hardening, which is the same for all weld zones, the mismatch caused by the different strain hardening properties was less apparent. The second factor was the loading configuration. In the shear tests, large stress concentrations were produced by the loading conditions within a zone locally and not near to a material interface. This lead to a failure which was localized to a zone, where again the material mismatch was less apparent.

Quasi static experiments have identified the lower weld nugget as the typical zone of failure origin in the stir weld. In contrast, the present dynamic analysis shows that the early failure of the stir welded joint is primarily caused by the stress risers at the material interfaces, and not due a single weld zone behaving as a weak link. This presents a key point of the current analysis and immediately suggests that FSW joint strength can be improved by minimization of interfacial stresses, which could

theoretically be achieved through a variety of process modifications, alleviation of abrupt property changes, and introduction of greater functional gradients within the material.

Chapter 4

A Pian-Sumihara Type Element for Modeling Shear Bands at Finite Deformation

4.1 Introduction

In chapter 2, it was shown that regularization through thermal diffusion in conjunction with a monolithic nonlinear solver will yield mesh insensitive results for a small strain shear band model. The monolithic solver was found to converge significantly faster than a field split solution of the same PDE model, which tended to grossly underestimate the amount of plastic straining in the test problem examined. Note that both methods are equivalent in the limiting case of infinitesimal mesh size and time step. The stark difference in performance was concluded to be the result of splitting errors, which arise due to sequential solution of the governing and constitutive equations in the two way coupled shear band model. Due to these errors, the monolithic method was able to achieve higher levels of accuracy for roughly two orders of magnitude less computational cost. For several other problems, splitting errors have

been found to lead to significantly degraded accuracy compared to monolithic solvers of similar mesh size and time step in nonlinear and multiphysics problems such as radiation-diffusion, magnetohydrodynamics, and shallow water flow [82]. It should be mentioned that the steep gradients produced during localization problems are not well resolved by coarse meshes. Thus inaccurate results can be obtained even if a mesh insensitive formulation is used without sufficient mesh refinement. See [113] for a method which aims to improve the behavior of isoparametric elements used in localization problems.

In this chapter, a large strain, incrementally objective formulation for a thermal softening, rate dependent inelastic material with diffusive regularization, is presented. This problem gives rise to a set of coupled, nonlinear PDEs, which are discretized and linearized in a mixed finite element formulation. The results section of the chapter focuses on comparing two types of elements, both of which employ a fully monolithic, global constitutive update which occurs simultaneously with the update of the displacements and the temperatures. The first element is the Irreducible Shear Band Quad (ISBQ), which employs the same interpolations as the irreducible quad, where history variables such as stress and equivalent plastic strain are sampled at the element gauss points. The second is the Pian Sumihara Shear Band Quad (PSSBQ), which is a mixed, assumed stress element using the stress interpolations first proposed by Pian and Sumihara [114].

The PSSBQ, developed in this chapter can thus be viewed as an extension of [125], who developed a mixed finite element method for elastoplasticity where displacement, stress, and equivalent plastic strain are interpolated degrees of freedom. They linearized the resulting nonlinear residual at the semi discrete level to develop a numerical solution using global Newton iterations at the fully discrete level. This is in contrast to classical methods for plasticity such as return mapping algorithms [124], where Newton iterations are carried out locally at the gauss points during the stress

update procedure. Here we extend the methodology of Simo et al. [125] to account for a rate dependent, thermal softening flow rule and finite thermal conductivity by including a solution to the energy equation, where temperature is considered as an additional degree of freedom in the coupled multiphysics model. The algorithmic approximation to the Lie derivative and Jaumann rate of Kirchhoff stress are derived for an incrementally objective implementation of the PSSBQ.

Among the celebrated features of the Pian-Sumihara element are the suppression of volumetric locking and reduced stiffening with mesh distortion for linear elasticity [146]. Under the same conditions of linear elasticity, volumetric locking is suppressed for four noded quad elements with the FBar or Bbar method, but distortion induced stiffening is still present. We show the same behavior occurs for the shear band problem by comparing results from the ISBQ and PSSBQ each with and without remeshing. While transferring solution variables from mesh to mesh is standard for the ISBQ, an additional step is required for the PSSBQ. This extra step is described in the text.

4.2 The Numerical Formulation

4.2.1 The PDE Model

The equations describing conservation of momentum and energy, as well as the elastic and inelastic constitutive relations and boundary conditions can be written as a set of coupled PDEs, as follows. The Momentum Equation, which includes inertial effects but ignores body forces

$$\rho_0 \ddot{u}_i = J \left(F^{-1}_{Aj} \sigma_{ij} \right)_{,A} \tag{4.1}$$

Here the displacement is u, the time t, the Cauchy stress tensor σ_{ij}, and the reference material density ρ_0. The deformation gradient is given by $F_{iA} = x_{i,A}$ and its determinant by J. Capital subscripts have been used for quantities on the initial configuration and lowercase subscripts are used for quantities on the current configuration. The Energy Equation, which accounts for diffusion as well as heat production in proportion to the plastic work, $\tau_{ij} d^p_{ij}$ [130], is written as

$$\rho_0 c\dot{T} = \kappa J F^{-1}_{Aj} F^{-1}_{Bj} T_{,AB} + \chi \tau_{ij} d^p_{ij} \tag{4.2}$$

Where T is the temperature, and κ, c, and χ are the conductivity, specific heat and the Taylor-Quinney coefficient, respectively. The Kirchhoff stress τ_{ij} is the Cauchy stress weighted by J so that $\tau_{ij} = J\sigma_{ij}$.

To develop the constitutive relations, we begin with a multiplicative decomposition of the deformation gradient into elastic (superscript e), thermal (superscript t) and inelastic (superscript p) parts, see also Figure 4.1

$$F_{iA} = F^e_{ia} F^t_{aq} F^p_{qA} \tag{4.3}$$

the velocity gradient $l_{ij} = \dot{F}_{iA} F^{-1}_{Aj}$ can thus be expanded as

$$l_{ij} = \dot{F}^e_{ia} F^{e,-1}_{aj} + F^e_{ia} \dot{F}^t_{aq} F^{t,-1}_{qb} F^{e,-1}_{bj} + F^e_{ia} F^t_{aq} \dot{F}^p_{qA} F^{p,-1}_{Ar} F^{t,-1}_{rb} F^{e,-1}_{bj} \tag{4.4}$$

This can be viewed as an additive split of the velocity gradient, where the first term on the right hand side of (4.4) is the elastic part of l_{ij}, the second term is the thermal part and the third term is the inelastic part. Note, some authors prefer to include the thermal part of the deformation gradient in F^e [86]. Thus, the rate of deformation d_{ij}, which is the symmetric part of the velocity gradient, is additively decomposed

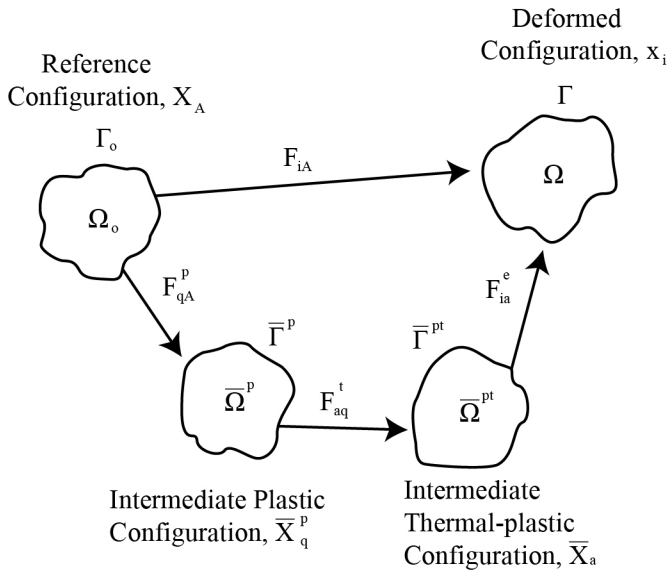

Figure 4.1: Multiplicative Split of F per equation (4.3)

into elastic, inelastic and thermal parts, so that

$$d_{ij} = \frac{1}{2}\left(l_{ij} + l_{ji}\right) = d^e_{ij} + d^p_{ij} + d^t_{ij} \tag{4.5}$$

Where d^e_{ij}, d^p_{ij} and d^t_{ij} are the elastic, inelastic and thermal rates of deformation, respectively. This particular decomposition of d_{ij} assumes that the elastic and thermal parts of the strain are small, an assumption appropriate for metals subjected to the loading conditions studied here.

An objective stress rate is employed so that the material derivative of Kirchhoff stress, $\dot{\tau}_{ij} = J\dot{\sigma}_{ij}$, is defined as

$$\dot{\tau}_{ij} = \overset{\nabla}{\tau}_{ij} + \left(\omega_{ik}\tau_{kj} - \tau_{ik}\omega_{kj}\right) \tag{4.6}$$

where $\overset{\nabla}{\tau}_{ij}$ is the Jaumann rate of Kirchhoff stress and $\omega_{ij} = \frac{1}{2}\left(l_{ij} - l_{ji}\right)$ is the spin tensor. In the rotation free reference frame, the elastic constitutive relation is given by

$$\overset{\nabla}{\tau}_{ij} = C^{elas}_{ijkl}\left(d_{kl} - d^{p}_{kl} - d^{t}_{kl}\right) \tag{4.7}$$

Then replacing $\overset{\nabla}{\tau}_{ij}$ in (4.6) with the right hand side of (4.7) results in

$$\dot{\tau}_{ij} = C^{elas}_{ijkl}\left(d_{kl} - d^{p}_{kl} - d^{t}_{kl}\right) + \left(\omega_{ik}\tau_{kj} - \tau_{ik}\omega_{kj}\right) \tag{4.8}$$

Where C^{elas}_{ijkl} is the tensor of elastic moduli and the thermal rate of deformation is

$$d^{t}_{ij} = \alpha\dot{T}\delta_{ij} \tag{4.9}$$

The inelastic constitutive relation is defined by

$$\dot{\bar{\gamma}}^{p} = \sqrt{\frac{2}{3}d^{p}_{ij}d^{p}_{ij}} \tag{4.10}$$

where $\dot{\bar{\gamma}}^{p}$ is the time rate of change of the equivalent plastic strain. J2 plasticity is employed, and thus the following additional constitutive relations are used:

$$d^{p}_{ij} = \frac{3}{2\bar{\tau}}g\left(\bar{\tau}, T, \bar{\gamma}^{p}\right)s_{ij} \tag{4.11}$$

where the deviatoric Kirchhoff stress s_{ij} is

$$s_{ij} = \tau_{ij} - \frac{1}{3}\tau_{kk}\delta_{ij} \tag{4.12}$$

the effective, or Von - Mises stress is then

$$\bar{\tau} = \sqrt{\frac{3}{2}s_{ij}s_{ij}} \tag{4.13}$$

using (4.10) along with (4.11) and (4.12) the inelastic work rate term in the energy equation (4.2) can be simplified to

$$\tau_{ij} d^p_{ij} = \frac{3}{2\bar{\tau}} g\left(\bar{\tau}, T, \bar{\gamma}^p\right) s_{ij} s_{ij} = \bar{\tau}\, g\left(\bar{\tau}, T, \bar{\gamma}^p\right) \tag{4.14}$$

Similarly, the right hand side of (4.10) can be reduced

$$\sqrt{\frac{2}{3} d^p_{ij} d^p_{ij}} = \frac{1}{\bar{\tau}} g\left(\bar{\tau}, T, \bar{\gamma}^p\right) \sqrt{\frac{3}{2} s_{ij} s_{ij}} = g\left(\bar{\tau}, T, \bar{\gamma}^p\right) \tag{4.15}$$

Lastly, we define the flow law g, which has been used in the computations [86, 144, 145], by

$$g\left(\bar{\tau}, T, \bar{\gamma}^p\right) = \dot{\gamma}_0 \left[\frac{\bar{\tau}}{\sigma_0 \left[1 + \gamma^p/\gamma_0\right]^N \left\{1 - \delta \left[\exp\left(\frac{T - T_0}{k}\right) - 1\right]\right\}} \right]^m \tag{4.16}$$

The parameters $\dot{\gamma}_0$, m, N, and T_0 are a reference strain rate, rate sensitivity exponent, strain hardening exponent, and reference temperature, respectively. δ and k are thermal softening parameters. See also Table 2 for a complete parameter list used in the model. Here we use a single constitutive model for the entire process, however use of different material models for different stages of deformation have been explored by [102]. The above equations can be combined into four governing equations which describe the evolution of the four unknown fields of displacement, stress, temperature and equivalent plastic strain. These are

$$\rho_0 \ddot{u}_i = \left(F_{Aj}^{-1}\tau_{ij}\right)_{,A} \tag{4.17}$$

$$\dot{\tau}_{ij} = C_{ijkl}^{elas}\left(d_{kl} - \frac{3}{2\bar{\tau}} g\left(\bar{\sigma}, T, \bar{\gamma}_p\right) s_{kl} - \alpha \dot{T}\delta_{kl}\right) + \left(\omega_{ik}\tau_{kj} - \tau_{ik}\omega_{kj}\right) \tag{4.18}$$

$$\rho_0 c\dot{T} = \kappa J F_{Aj}^{-1} F_{Bj}^{-1} T_{,AB} + \chi \bar{\tau} g\left(\bar{\tau}, T, \bar{\gamma}^p\right) \tag{4.19}$$

$$\dot{\bar{\gamma}}^p = g\left(\bar{\tau}, T, \bar{\gamma}^p\right) \tag{4.20}$$

Lastly the boundary conditions are

$$\begin{aligned} u &= \bar{u} \quad \text{on} \quad \Gamma^u \\ T &= \bar{T} \quad \text{on} \quad \Gamma^T \\ n_i\sigma_{ij} &= \bar{t}_j \quad \text{on} \quad \Gamma^t \\ n_i q_i &= \bar{q} \quad \text{on} \quad \Gamma^q \end{aligned} \tag{4.21}$$

Where $\bar{t}_j$ and $\bar{q}$ are the prescribed traction and prescribed heat flux on the deformed boundary. The effects of voids and microcracking that exist in a shear band [101, 112] are not modeled in this study.

Before moving on to the discrete model, we note that there will be four configurations of interest: the isoparametric, the reference, the deformed configuration at time n+1, and the deformed configuration at time n, depicted in Figure 4.2. These configurations are associated with the coordinates ξ_p, X_A, ${}_{n+1}x_i$, and ${}_{n}x_a$, respectively. The associated stress measures are the isoparametric stress Σ_{pq} for the isoparametric configuration, the second Piola Kirchhoff Stress S_{AB} for the reference configuration, and the Cauchy stress ${}_{n+1}\sigma_{ij}$ and ${}_{n}\sigma_{ab}$ for the deformed configurations at n+1 and n, respectively. The isoparametric configuration, upon which gauss quadrature is performed, does not change with time, while the deformed configuration does. The reference configuration is arbitrary, and for convenience in the implementation of the

numerical formulation outlined below, we take the reference configuration at time n+1 as the deformed configuration at time step n.

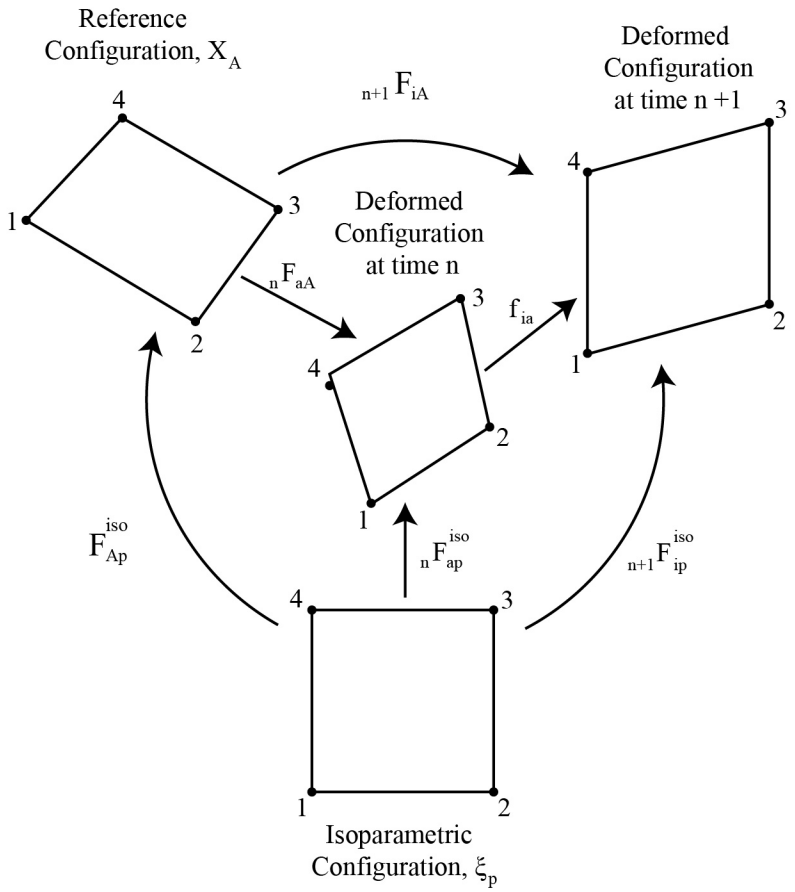

Figure 4.2: Geometric configurations used in the numerical implementation. For convenience we let the reference configuration coincide with the deformed configuration at time n.

4.2.2 The Discrete Model

The Discrete Residual

The weak form is obtained by multiplying the momentum equation, elastic constitutive equation, energy equation, and inelastic constitutive relation by the weight functions w^u, w^σ, w^T, and $w^{\tilde{\gamma}^p}$ respectively, and integrating over the problem do-

main in the initial configuration. This defines the weak form of the residual $\mathbf{R} = \begin{bmatrix} R^u & R^\sigma & R^T & R^{\bar{\gamma}^p} \end{bmatrix}^{\mathbf{T}}$ where

$$R^u = \int_{\Omega_0} \left[w_i^u \rho_0 \ddot{u}_i + w_{i,A}^u F_{Aj}^{-1} \tau_{ij} \right] d\Omega_0 - \int_{\Gamma_0^T} w_i^u \bar{T}_i d\Gamma_0^{\bar{T}} = 0 \tag{4.22}$$

$$R^\sigma = \int_{\Omega_0} w_{ij}^\sigma \left[\dot{\tau}_{ij} - C_{ijkl}^{elas} \left(d_{kl} - \frac{3}{2\bar{\tau}} g\left(\bar{\tau}, T, \bar{\gamma}_p\right) s_{kl} - \alpha \dot{T} \delta_{kl} \right) - \left(\omega_{ik}\tau_{kj} - \tau_{ik}\omega_{kj} \right) \right] d\Omega_0 = 0 \tag{4.23}$$

$$R^T = \int_{\Omega_0} \left\{ w^T \left[\rho_0 c \dot{T} - \chi \bar{\tau} g\left(\bar{\tau}, T, \bar{\gamma}^p\right) \right] + \kappa J F_{Aj}^{-1} F_{Bj}^{-1} w_{,A}^T T_{,A} \right\} d\Omega_0 - \int_{\Gamma_0^q} \kappa w^T \bar{q} d\Gamma_0^q = 0 \tag{4.24}$$

$$R^{\bar{\gamma}^p} = \int_{\Omega_0} w^{\bar{\gamma}^p} \left[\dot{\bar{\gamma}}^p - g\left(\bar{\tau}, T, \bar{\gamma}^p\right) \right] d\Omega_0 = 0 \tag{4.25}$$

Note that integration by parts has been used where appropriate. Also bold letters are use indicate a matrix or a vector and a bold uppercase $^{\mathbf{T}}$ indicates the transpose operation. This weak form contains spatial derivatives of displacement and temperature, and therefore these two fields must be approximated by C^0 functions. On the other hand, spatial derivatives of the equivalent plastic strain and the stresses do not appear and thus C^{-1} functions will suffice. Thus, with these minimum continuity requirements in mind, we seek to find $u \in S_u$, $\sigma \in C^{-1}$, $T \in S_T$, and $\bar{\gamma}^p \in C^{-1}$ such that at any time t

$$R = 0, \qquad \forall w^u \in S_u^0, \qquad \forall w^\sigma \in C^{-1}, \qquad \forall w^{\bar{\gamma}_p} \in S_T^0, \qquad \forall w^{\gamma_p} \in C^{-1} \tag{4.26}$$

Where

$$S_u = \left\{ u\left(X,t\right) | u \in C^0, u = \bar{u} \text{ on } \Gamma^u \right\} \quad S_u^0 = \left\{ w^u\left(X\right) | w^u \in C^0, w^u = 0 \text{ on } \Gamma^u \right\} \tag{4.27}$$

and

$$S_T = \left\{ T\left(X,t\right) | T \in C^0, T = \bar{T} \text{ on } \Gamma^T \right\} \quad S_T^0 = \left\{ w^T\left(X\right) | w^T \in C^0, w^T = 0 \text{ on } \Gamma^T \right\} \tag{4.28}$$

The weak form is discretized in time using Newmark's method for the momentum equation with integration parameters $\mathcal{B}$ and $\mathcal{G}$. The backward Euler method is used for the remaining three equations. The trapezoidal rule has not been used because for certain regimes of mesh size and time step for diffusion problems, this method can result in oscillations in the temperature field, which is undesirable for this problem due to the nonlinear coupling of temperature to other fields.

The time discrete residual at time n+1 is then ${}_{n+1}\mathbf{R} = \left[\begin{array}{cccc} {}_{n+1}R^u & {}_{n+1}R^\sigma & {}_{n+1}R^T & {}_{n+1}R^{\bar{\gamma}^p} \end{array} \right]^{\mathbf{T}}$. Note, for the rest of this chapter, quantities to the right of an equal sign shall be assumed to be evaluated at time step n+1 unless otherwise noted by a left subscript.

In order to ensure incremental objectivity, time stepping for the elasticity equation is performed as follows: first, quantities associated with the current configuration are pulled back to the reference configuration. Time discretization with backward Euler is performed on the pulled back quantities, and the results are then pushed to the current configuration. Details can be found in [124]. The incrementally objective, algorithmic approximation to the rate of deformation becomes

$$\Delta t \; d_{ij} = \frac{1}{2} \left[\delta_{ij} - f_{ai}^{-1} f_{aj}^{-1} \right] \tag{4.29}$$

where the incremental deformation gradient f_{ia} maps from the deformed configuration at time step n to the deformed configuration at time step n+1 so that

$$f_{ia} = F_{iB} \; {}_nF_{Ba}^{-1} \tag{4.30}$$

Objective algorithmic approximations for the Jaumann rate of Kirchhoff is obtained by first defining the algorithmic approximation to the Lie derivative of Kirchhoff stress . The Lie derivative of Kirchhoff stress is the push forward of the time derivative of the pull back of the Kirchhoff stress, namely

$$L_v\tau_{ij} = F_{iA}F_{jB}\frac{\partial}{\partial t}\left[F^{-1}_{Ak}F^{-1}_{Bl}\tau_{kl}\right] \tag{4.31}$$

Using the relationship between the Kirchhoff and second Piola Kirchhoff stress

$$S_{AB} = F^{-1}_{Ai}F^{-1}_{Bj}\tau_{ij} \tag{4.32}$$

the Lie derivative can also be written as

$$L_v\tau_{ij} = F_{iA}F_{jB}\frac{\partial}{\partial t}\left[S_{AB}\right] \tag{4.33}$$

The algorithmic approximation to the Lie derivative of Kirchhoff stress is given by [124] as

$$L_v\ \tau_{ij} = \frac{1}{\Delta t}\left(\tau_{ij} - \tilde{\tau}_{ij}\right) \tag{4.34}$$

where $\tilde{\tau}$ is the Kirchhoff stress at time n, which is associated with the deformed configuration at time n, pushed to the deformed configuration at time n+1 so that

$$\tilde{\tau}_{ij} = f_{ia}f_{jb}\ {}_n\tau_{ab} \tag{4.35}$$

The Lie derivative and the Jaumann rate are related by

$$\overset{\nabla}{\tau}_{ij} = L_v\tau_{ij} + \left(d_{ik}\tau_{kj} + \tau_{ik}d_{kj}\right) \tag{4.36}$$

combining (4.36) with (4.34) the algorithmic approximation to the Jaumann rate becomes

$$\overset{\nabla}{\tau}_{ij} = \frac{1}{\Delta t}\left(\tau_{ij} - \tilde{\tau}_{ij}\right) + \left(d_{ik}\tau_{kj} + \tau_{ik}d_{kj}\right) \tag{4.37}$$

The time stepping procedure results in the following semi discrete residuals

$$R^u = \int_{\Omega_0}\left[w_i^u \frac{\rho_0}{\beta\Delta t^2}\left[u_i - \ \tilde{u}_i\right] + w_{i,A}^u F_{Aj}^{-1}\ \tau_{ij}\right] d\Omega_0 - \int_{\Gamma_0^T} w_i^u\ \bar{T}_i d\Gamma_0^{\bar{T}} \tag{4.38}$$

$$R^\sigma = \int_{\Omega_0} w_{ij}^\sigma[\frac{1}{\Delta t}\left(\tau_{ij} - \tilde{\tau}_{ij}\right) - C_{ijkl}^{elas}\left(d_{kl} - \frac{3}{2\bar{\tau}} g\left(\bar{\tau}, T, \bar{\gamma}^p\right) s_{kl} - \alpha\dot{T}\delta_{kl}\right) \tag{4.39}$$

$$- \left(d_{ik}\tau_{kj} + \tau_{ik}d_{kj}\right)]d\Omega_0$$

$$R^T = \int_{\Omega_0}\left[w^T\left[\frac{\rho_0 c}{\Delta t}\left(T - {}_nT\right) - \chi\bar{\tau} g\left(\bar{\tau}, T, \bar{\gamma}^p\right)\right] + \kappa J F_{Aj}^{-1} F_{Bj}^{-1} w_{,A}^T T_{,B}\right] d\Omega_0 \tag{4.40}$$

$$- \int_{\Gamma_0^Q} \kappa w^T \bar{Q} d\Gamma_0^Q$$

$$R^{\bar{\gamma}^p} = \int_{\Omega_0} w^{\bar{\gamma}^p}\left[\frac{1}{\Delta t}\left(\bar{\gamma}^p - {}_n\bar{\gamma}^p\right) - g\left(\bar{\tau}, T, \bar{\gamma}^p\right)\right] d\Omega_0 \tag{4.41}$$

Where $\bar{T}_i$ and $\bar{Q}$ are the prescribed traction and heat flux on the reference configuration. The momentum equation uses a second order time stepping procedure where

$$\tilde{u}_i = {}_nu_i + \Delta t\ {}_nv_i + \frac{\Delta t^2}{2}\left(1 - 2\mathcal{B}\right)\ {}_na_i \tag{4.42}$$

For a single element, let the Galerkin approximation be

$$\begin{aligned} u_i &= N_{i\alpha}^u \hat{u}_\alpha & w_i^u &= N_{i\alpha}^u \hat{w}_\alpha^u \\ \sigma_{ij} &= N_{ij\alpha}^\sigma \hat{\lambda}_\alpha & w_{ij}^\sigma &= N_{ij\alpha}^\sigma \hat{w}_\alpha^\sigma \\ T &= N_\alpha^T \hat{T}_\alpha & w^T &= N_\alpha^T \hat{w}_\alpha^T \\ \bar{\gamma}^p &= N_\alpha^{\bar{\gamma}_p} \hat{\bar{\gamma}}_\alpha^p & w^{\bar{\gamma}_p} &= N_\alpha^{\bar{\gamma}_p} \hat{w}_\alpha^{\bar{\gamma}_p} \end{aligned} \tag{4.43}$$

Where N is a tensor containing the appropriate shape functions. Note the number of indices for N depends on whether the field is a scalar, vector, or tensor. The

subscript α is always associated with the number of degrees of freedom, the range of which depends on the field in question and its associated shape functions. The ranges of α for the elements implemented in this study are given in Table 4.1. The hatted field variables are to be understood as vectors of degrees of freedom belonging to one element. Substitution of the Galerkin approximation into the time discrete residual, Eqs. (4.38)- (4.41), leads to the fully discrete residual, which forms a set of coupled nonlinear algebraic equations:

$$\hat{\mathbf{R}}^u_\alpha = \mathbf{M}^u_{\alpha\beta}\left(\hat{u}_\beta - \tilde{\hat{u}}_\beta\right) + \mathbf{f}^{u\ int}_\beta - \mathbf{f}^{u\ ext}_\beta = 0 \tag{4.44}$$

$$\hat{\mathbf{R}}^\sigma_\alpha = \mathbf{M}^\sigma_{\alpha\beta}\left(\hat{\lambda}_\beta - \tilde{\hat{\lambda}}_\beta\right) + \mathbf{f}^\sigma_\beta = 0 \tag{4.45}$$

$$\hat{\mathbf{R}}^T_\alpha = \mathbf{M}^T_{\alpha\beta}\left(\hat{T}_\beta - {}_n\hat{T}_\beta\right) + \left(\mathbf{f}^{T\ int}_\beta - \mathbf{f}^{T\ ext}_\beta\right) = 0 \tag{4.46}$$

$$\hat{\mathbf{R}}^{\bar{\gamma}^p}_\alpha = \mathbf{M}^{\bar{\gamma}^p}_{\alpha\beta}\left(\hat{\bar{\gamma}}^p_\beta - {}_n\hat{\bar{\gamma}}^p_\beta\right) + \mathbf{f}^{\bar{\gamma}^p}_\beta = 0 \tag{4.47}$$

All matrices $\mathbf{M}$ are mass matrices. Linearization of (4.44) - (4.47) is presented in the next section.

Consistent Linearization

A consistent linearization of the PDE system can be obtained in one of two ways. The first is by differentiating the time discrete (but spatially continuous) residual (4.38) - (4.41), and substituting the Galerkin approximation into the result. The second method is to differentiate the fully discrete residual (4.44) - (4.47). In this study, the former method is used, however, either method could be used to linearize the system without the need for numerical differentiation. The linearized system can be written

in a partitioned form, at nonlinear iteration k and time step n+1, as

$$\begin{bmatrix} J_i^{uu} & J_{ij}^{u\sigma} & J^{uT} & J^{u\bar{\gamma}^p} \\ J_i^{\sigma u} & J_{ij}^{\sigma\sigma} & J^{\sigma T} & J^{\sigma\bar{\gamma}^p} \\ J_i^{Tu} & J_{ij}^{T\sigma} & J^{TT} & J^{T\bar{\gamma}^p} \\ J_i^{\bar{\gamma}_p u} & J_{ij}^{\bar{\gamma}^p\sigma} & J^{\bar{\gamma}^p T} & J^{\bar{\gamma}^p\bar{\gamma}^p} \end{bmatrix}^k \begin{bmatrix} \delta u_i \\ \delta\sigma_{ij} \\ \delta T \\ \delta\bar{\gamma}^p \end{bmatrix} + \begin{bmatrix} R^u \\ R^\sigma \\ R^T \\ R^{\bar{\gamma}^p} \end{bmatrix}^k = \mathbf{0} \tag{4.48}$$

The Galerkin approximation of the Newton correction is also needed. This is

$$\delta u_i = N_{i\alpha}^u \delta\hat{u}_\alpha \qquad \delta\sigma_{ij} = N_{ij\alpha}^\sigma \delta\hat{\lambda}_\alpha \qquad \delta T = N_\alpha^T \delta\hat{T}_\alpha \qquad \delta\bar{\gamma}^p = N_\alpha^{\bar{\gamma}_p} \delta\hat{\bar{\gamma}}_\alpha^p \tag{4.49}$$

The product of the Jacobian J and the Newton correction δp is the first variation of R in the direction of δp, where $p = [u_i \ \sigma_{ij} \ T \ \bar{\gamma}^p]^{\mathbf{T}}$. This is also known as the Gateaux derivative and is defined as

$$J\delta p = \delta R\left[p^k\right] = \lim_{\epsilon\to 0} \frac{1}{\epsilon}\left(R\left[p^k + \epsilon\delta p\right] - R\left[p^k\right]\right) = \frac{d}{d\epsilon} R\left[p^k + \epsilon\delta p\right]\Big|_{\epsilon=0} \tag{4.50}$$

This derivative can be computed analytically without numerical differentiation in blocks, and subsequently the Galerkin approximation can be introduced, leading to the fully discrete Jacobian. Detailed derivations for a few blocks can be found in Appendix C. The resulting fully discrete linearized system is then

$$\begin{bmatrix} \mathbf{M}_{\alpha\beta}^u + \mathbf{L}_{\alpha\beta}^u & \mathbf{K}_{\alpha\beta}^u & \mathbf{0} & \mathbf{0} \\ \mathbf{K}_{\alpha\beta}^\sigma + \mathbf{L}_{\alpha\beta}^\sigma & \mathbf{M}_{\alpha\beta}^\sigma + \mathbf{S}_{\alpha\beta}^\sigma + \mathbf{G}_{\alpha\beta}^{\sigma\sigma} & \mathbf{G}_{\alpha\beta}^{\sigma T} & \mathbf{G}_{\alpha\beta}^{\sigma\bar{\gamma}_p} \\ \mathbf{L}_{\alpha\beta}^T & \mathbf{G}_{\alpha\beta}^{T\sigma} & \mathbf{M}_{\alpha\beta}^T + \left(\mathbf{K}_{\alpha\beta}^T + \mathbf{G}_{\alpha\beta}^{TT}\right) & \mathbf{G}_{\alpha\beta}^{T\bar{\gamma}_p} \\ \mathbf{0} & \mathbf{G}_{\alpha\beta}^{\bar{\gamma}_p\sigma} & \mathbf{G}_{\alpha\beta}^{\bar{\gamma}_p T} & \mathbf{M}_{\alpha\beta}^{\bar{\gamma}_p} + \mathbf{G}_{\alpha\beta}^{\bar{\gamma}_p\bar{\gamma}_p} \end{bmatrix}^k \begin{bmatrix} \delta\hat{\mathbf{u}}_\beta \\ \delta\hat{\lambda}_\beta \\ \delta\hat{\mathbf{T}}_\beta \\ \delta\hat{\bar{\gamma}}_\beta^{\mathbf{p}} \end{bmatrix} + \begin{bmatrix} \mathbf{R}_\alpha^u \\ \mathbf{R}_\alpha^\sigma \\ \mathbf{R}_\alpha^T \\ \mathbf{R}_\alpha^{\bar{\gamma}^p} \end{bmatrix}^k = 0 \tag{4.51}$$

M denotes mass matrices, **K** stiffness matrices arising from linear material behavior, **G** matrices arising from nonlinear material behavior, **L** matrices arising from non-

linear geometric behavior, and $\mathbf{S}$ is due to the spin correction term in the Jaumann rate. The structure of the Jacobian reflects the strongly coupled nature of the system of PDEs, and does not reveal any clear way to simplify or reduce the system by eliminating any of the four fields in $\mathbf{p}$. Note that the Jacobian is not symmetric.

4.2.3 Shape Functions

The preceding formulation has been presented as a general mixed formulation which permits the use of a monolithic thermo-mechanical solver. Choice of shape functions should be made carefully taking into consideration the continuity requirements in equations (4.27) and (4.28), and the Babuška-Brezzi conditions [7, 36]. Additionally, careful choice of shape functions can be used to develop a locking free formulation, an important feature for simulating large, nearly incompressible deformations, as is the case with shear bands. It is also possible to reduce the formulation to one with identical interpolation as an irreducible element while retaining the fully monolithic thermo-mechanical solver. For a four node quad this is done by choosing the following shape functions for equivalent plastic strain and each stress component

$$N_i\left(\xi_1^j, \xi_2^j\right) = \delta_{ij} \qquad i, j = 1, 2, 3, 4 \tag{4.52}$$

Where ξ_1, ξ_2 are the isoparametric coordinates, and $\left(\xi_1^j, \xi_2^j\right)$ are the typical gauss quadrature points. Note that in this case the history variables are sampled at the gauss points. Thus in the linearized system (4.51), the Newton corrections for stresses and equivalent plastic strains $\delta\hat{\sigma}$ and $\delta\hat{\bar{\gamma}}^p$ are vectors containing stress and equivalent plastic strains at the gauss points. However, in contrast with common implementations of a four noded quad, where history variables are updated locally on the gauss points, here the updates are done on the global level by solving for all gauss points at once.

This local technique is inappropriate for the thermo mechanical shear band model where the temperature dependent constitutive law at one gauss point is coupled to other gauss points through the flow of heat caused by thermal diffusion. We will refer this element, where the interpolation is identical to the irreducible four node quad, but where the history variable update is fully monolithic as defined in (4.51), as the Irreducible Shear Band Quad (ISBQ). For more details of this type of interpolation in the context of plasticity, see [42]

The second 2D element we have implemented we term the Pian-Sumihara Shear Band Quad (PSSBQ). The equivalent plastic strains are sampled at the gauss points according to (4.52), in the same way as the ISBQ. However the PSSBQ uses the Pian-Sumihara functions for interpolating stress [114], which are known to be free of locking in the incompressible limit, and to perform well with a distorted mesh [146]. Recall that there are three configurations of interest, the isoparametric, the reference, and the deformed configurations, which have associated with them the isoparametric stress Σ_{ab}, the Second Piola Kirchhoff Stress S_{AB} and the Cauchy stress σ_{ij}, respectively (see Figure 4.2). In order to complete the formulation of the PSSBQ we need to define the algorithmic approximation to the Cauchy stress, as well as the incrementally objective approximations to the Lie derivative and Jaumann rate of the Kirchhoff stress using the Pian-Sumihara functions for stress. First, the isoparametric stress is defined as

$$\Sigma_{ab} = N^{\Sigma}_{ab\alpha}\hat{\lambda}_{\alpha} \tag{4.53}$$

and expanded to

$$\begin{bmatrix} \Sigma_{11} & \Sigma_{12} & 0 \\ \Sigma_{21} & \Sigma_{22} & 0 \\ 0 & 0 & \Sigma_{33} \end{bmatrix} = \begin{bmatrix} \hat{\lambda}_1 + \xi_2\hat{\lambda}_4 & \hat{\lambda}_3 & 0 \\ \hat{\lambda}_3 & \hat{\lambda}_2 + \xi_1\hat{\lambda}_5 & 0 \\ 0 & 0 & \hat{\lambda}_6 \end{bmatrix} \tag{4.54}$$

Where the degrees of freedom defining the stress field are $\hat{\lambda}$, and the shape functions $N^{\Sigma}_{ab\alpha}$ interpolate the isoparametric stress. The Cauchy stress is then computed by pushing these stresses to the current configuration with the isoparametric map F^{iso}_{ia}, evaluated at the center of the element, i.e.

$$\sigma_{ij} = F^{iso}_{ia} F^{iso}_{jb} \Sigma_{ab} \tag{4.55}$$

substituting (4.54) into (4.55) the algorithmic approximation to the Cauchy stress is

$$\sigma_{ij} = F^{iso}_{ia} F^{iso}_{jb} N^{\Sigma}_{ab\alpha} \hat{\lambda}_{\alpha} \tag{4.56}$$

Alternatively, we can define the shape functions interpolating the Cauchy stress $N^{\sigma}_{ij\alpha}$ as

$$N^{\sigma}_{ij\alpha} = F^{iso}_{ia} F^{iso}_{jb} N^{\Sigma}_{ab\alpha} \tag{4.57}$$

resulting in

$$\sigma_{ij} = N^{\sigma}_{ij\alpha} \hat{\lambda}_{\alpha} \tag{4.58}$$

Next, the objective approximations to the Lie derivative and Jaumann rate of Kirchhoff stress are derived. Recalling equation (4.33), the definition of the second Piola Kirchhoff stress is needed. Substituting (4.55) into (4.32) we have

$$S_{AB} = J F^{-1}_{Ai} F^{-1}_{Bj} N^{\sigma}_{ij\alpha} \hat{\lambda}_{\alpha} \tag{4.59}$$

Then using (4.57) and defining the map from the isoparametric to the reference configuration $F^{iso}_{Aa} = F^{-1}_{Ai} F^{iso}_{ia}$ the algorithmic approximation to the second Piola Kirchhoff stress is

$$S_{AB} = J F^{iso}_{Aa} F^{iso}_{Bb} N^{\Sigma}_{ab\alpha} \hat{\lambda}_{\alpha} \tag{4.60}$$

Similar to (4.57), the shape functions interpolating the second Piola Kirchhoff stress, $N^S_{AB\alpha}$, can be defined as

$$N^S_{AB\alpha} = F^{iso}_{Aa} F^{iso}_{Bb} N^{\Sigma}_{ab\alpha} \tag{4.61}$$

resulting in

$$S_{AB} = J N^S_{AB\alpha} \hat{\lambda}_\alpha \tag{4.62}$$

and

$${}_nS_{AB} = {}_nJ N^S_{AB\alpha}\ {}_n\hat{\lambda}_\alpha \tag{4.63}$$

With (4.61), (4.60), and (4.32), the Cauchy stress can be written in terms of the second Piola Kirchhoff stress interpolants as

$$\sigma_{ij} = N^S_{AB\alpha} F_{iA} F_{jB} \hat{\lambda}_\alpha \tag{4.64}$$

Which is the form of the Cauchy stress employed in our implementation. Next the algorithmic approximation to the Lie derivative of Kirchhoff stress can then be defined as

$$F^{-1}_{Ai} \left(L_v\ \tau_{ij}\right)\ F^{-1}_{Bj} = \frac{1}{\Delta t} \left(S_{AB} - {}_nS_{AB}\right) \tag{4.65}$$

then substituting (4.62) and (4.63) for S_{AB} and ${}_nS_{AB}$ respectively

$$F^{-1}_{Ai} \left(L_v\ \tau_{ij}\right)\ F^{-1}_{Bj} = \frac{1}{\Delta t} \left(N^S_{AB\alpha} \left[J\hat{\lambda}_\alpha - {}_nJ\ {}_n\hat{\lambda}_\alpha\right]\right) \tag{4.66}$$

By moving the deformation gradient terms from the left to the right hand side, the algorithmic approximation for the Lie derivative of Kirchhoff stress is

$$L_v\ \tau_{ij} = \frac{1}{\Delta t} \left(N^{\sigma}_{ij\alpha} \left[J\hat{\lambda}_\alpha - \ {}_nJ\ {}_n\hat{\lambda}_\alpha\right]\right) \tag{4.67}$$

Using the same spin correction in (4.36), the Jaumann rate of Kirchhoff stress is then

$$\overset{\nabla}{\tau}_{ij} = \left(N^{\sigma}_{ij\alpha} \left[J\hat{\lambda}_{\alpha} - {}_{n}J \, {}_{n}\hat{\lambda}_{\alpha} \right] \right) + J\Delta t \left(d_{ik} N^{\sigma}_{kj\alpha} + N^{\sigma}_{ik\alpha} d_{kj} \right) \hat{\lambda}_{\alpha} \tag{4.68}$$

Note that equation (4.68) is equivalent to equation (4.37), with $\tau_{ij} = JN^{\sigma}_{ij\alpha}\hat{\lambda}_{\alpha}$ and $\tilde{\tau}_{ij} = {}_{n}JN^{\sigma}_{ij\alpha} \, {}_{n}\hat{\lambda}_{\alpha}$ Since the shape functions $N^{\sigma}_{ij\alpha}$ are deformation dependent, the reference configuration is used to compute the weight and shape functions $N^{S}_{IJ\alpha}$, with the Cauchy stress computed from (4.64). Note that now wherever the Cauchy stress appears, additional geometric linearization terms will arise due the deformation gradients in (4.64). With the shape functions fully defined, the number of degrees of freedom for each field in each element are then given in Table 4.1

Table 4.1: Degrees of freedom for each element

Field	DoF for PSSBQ	DoF for ISBQ
$\hat{u}_{\alpha}$	8	8
$\hat{\lambda}_{\alpha}$	6	16
$\hat{T}_{\alpha}$	4	4
$\hat{\bar{\gamma}}^{p}_{\alpha}$	4	4

4.3 Results

4.3.1 Implementation Details

The ISBQ and the PSSBQ have been implemented as user elements in the finite element code FEAP [131]. Meshes were generated using gmsh [59], and ParaView [67] and Matplotlib [74] were used to visualize the results. A mesh refinement study has been conducted for a 20×20 μm^2 part in plane strain tension on 20 by 20, 40 by 40, 80 by 80 and 160 by 160 meshes, which will be referred to as meshes 1 - 4. Only the upper right quadrant is modeled due to symmetry, as shown in Figure 4.3. The linear problem (4.51) is assembled using PETSc version 3.4 [10] and solved using

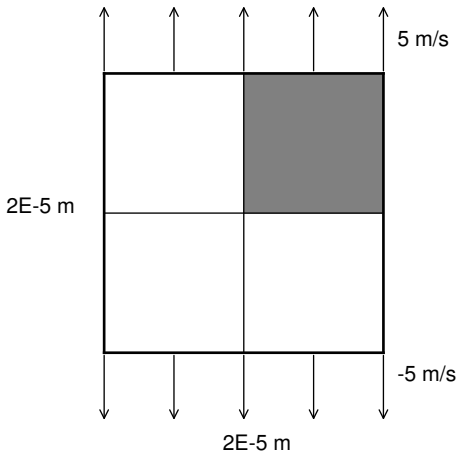

Figure 4.3: Problem Statement

the PETSc interface to UMFPACK [45], a sparse direct solver. Newton iterations are terminated using the criterion

$$\max\left\{\left\|\frac{\mathbf{R}^u}{\mathbf{R}_0^u}\right\|,\left\|\frac{\mathbf{R}^\sigma}{\mathbf{R}_0^\sigma}\right\|,\left\|\frac{\mathbf{R}^T}{\mathbf{R}_0^T}\right\|,\left\|\frac{\mathbf{R}^{\gamma^p}}{\mathbf{R}_0^{\gamma^p}}\right\|\right\}\leq tol \tag{4.69}$$

Where $tol = 1.0E-8$. The material parameters used in this study are shown in Table 4.2.

Table 4.2: Material Properties and Parameters [145]

Property Name	Symbol	Value	Unit
Young's Modulus	E	200E9	Pa
Poisson's Ratio	ν	0.3	-
Mass Density	ρ	7830	$\frac{kg}{m^3}$
Specific Heat	c	448	$\frac{J}{kgK}$
Taylor - Quinney Coefficient	χ	0.9	-
Thermal Conductivity	κ	803.5	$\frac{W}{mK}$
Reference Strain Rate	$\dot{\gamma}_0$	0.001	$\frac{1}{s}$
Rate Sensitivity Parameter	m	70	-
Yield Stress	σ_0	2000E6	Pa
Yield Strain	γ_0	0.01	-
Strain Hardening Exponent	n	0.01	-
Reference Temperature	T_0	293	K
Thermal Softening Parameter	δ	0.8	-
Thermal Softening Parameter	k	500	K

A material imperfection in the form of a depreciated yield stress and strain is applied at the lower left corner of the modeled domain, which creates an inhomogeneity in the solution field, upon which the shear band will nucleate. The yield stress and strain are varied according to the smooth function Y (see chapter 2 for more details), so that

$$\begin{aligned} \sigma_{yield}\left(X_1, X_2\right) &= \sigma_0 Y\left(X_1, X_2\right) \\ \gamma_{yield}\left(X_1, X_2\right) &= \gamma_0 Y\left(X_1, X_2\right) \end{aligned} \tag{4.70}$$

where

$$Y\left(X_1, X_2\right) = 1 - 0.04\left[sech\left(\frac{\sqrt{X_1^2 + X_2^2}}{5 \cdot 10^{-6}}\right)\right]^2 \tag{4.71}$$

The PSSBQ can be shown to posses the ideal constraint ratio for the displacement - stress formulation [146], and is thus free of volumetric locking in the incompressible limit. The ISBQ, on the other hand, is known to lock and therefore the $\bar{F}$ method [126], the finite deformation extension of the $\bar{B}$ method [71], is employed. With this method, the dilatation J is replaced with the mean dilation $\bar{J}$, so that

$$\bar{J} = \frac{\int_{\Omega_0} J d\Omega_0}{\int_{\Omega_0} d\Omega_0} \tag{4.72}$$

This approach was originally suggested by Nagtegaal et. al. [107]. The deformation gradient F_{iI} is then replaced with $\bar{F}_{iI}$

$$\bar{F}_{iI} = \left(\frac{\bar{J}}{J}\right)^{\frac{1}{3}} F_{iI} \tag{4.73}$$

Lastly, the derivatives of the displacement shape functions $N^u_{i\alpha,j}$ are replaced with $\bar{N}^u_{i\alpha,j}$ so that

$$\bar{N}^u_{i\alpha,j} = N^u_{i\alpha,j} + \delta_{ij}\left(\hat{N}^u_{k\alpha,k} - N^u_{k\alpha,k}\right) \tag{4.74}$$

Where the dilatational part of the derivatives $N^u_{k\alpha,k}$ are replaced by the mean dilatational part $\hat{N}^u_{k\alpha,k}$

$$\hat{N}^u_{k\alpha,k} = \frac{\int_{\Omega_0} J N^u_{k\alpha,k} d\Omega_0}{\int_{\Omega_0} J d\Omega_0} \tag{4.75}$$

The two elements have been implemented with a remeshing procedure, in an attempt to minimize the effect of mesh distortion degrading solution accuracy. The remeshing procedure is as follows: first, nodes are rezoned with several sweeps of the algorithm given by [65]. See figure 4.4 for images of the distorted and rezoned meshes. Note, the connectivity is unchanged, and only the nodal positions of the mesh are changed. Next, the stresses and equivalent plastic strains are projected from the gauss points to the nodes using an L2 projection [131]. The nodal velocities, accelerations, temperatures, and the projected values of stress and plastic strain are then transferred from the nodes of the old mesh, to the nodes of the new mesh. This requires evaluation of the inverse isoparametric map, which is given in [66]. The displacements are not transferred, and instead are set to zero since the remeshed configuration simply becomes the new reference configuration. The stresses and equivalent plastic strains are transferred from the nodes of the new mesh, to the gauss points of the new mesh. For the ISBQ, the remeshing procedure is now complete, but the PSSBQ requires an additional step to recover the stress parameters $\hat{\lambda}_\alpha$ from the stress at the gauss points. This is achieved by solving the following linear system

$$M^e_{\alpha\beta} \hat{\lambda}^e_\beta = P^e_\beta \tag{4.76}$$

where

$$M^e_{\alpha\beta} = \int_{\Omega^e} N^\sigma_{ij\alpha} N^\sigma_{ij\beta} d\Omega^e \tag{4.77}$$

and

$$P^e_\beta = \int_{\Omega^e} N^\sigma_{ij\beta} \sigma_{ij} d\Omega^e \tag{4.78}$$

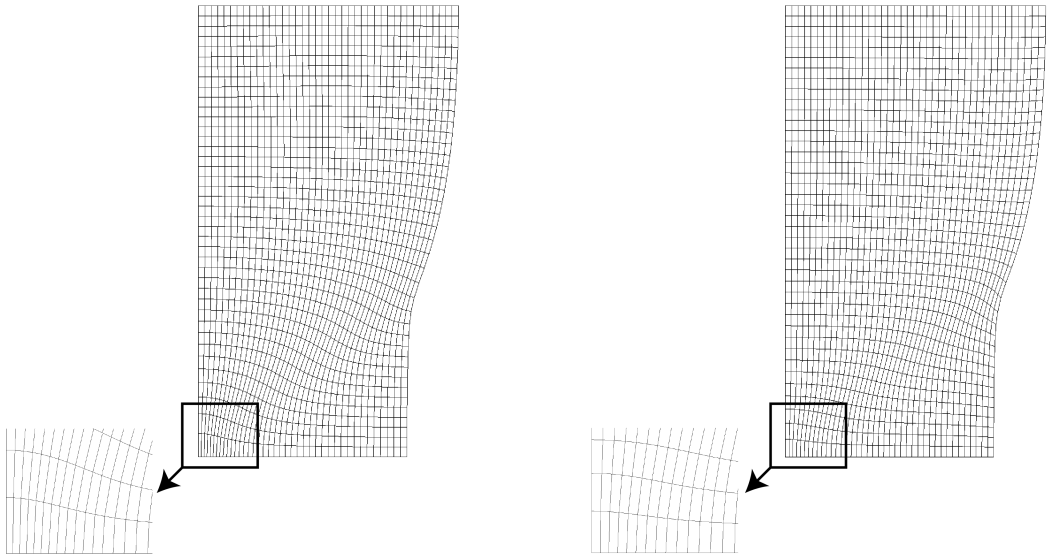

(a) (b)

Figure 4.4: Final mesh for the PSSBQ without remeshing shown on the left, and with remeshing shown on the right. Note the extremely poor aspect ratio of the elements in the zoomed region on the left and the improvement after remeshing on the right.

The superscript e indicates this process is carried out locally for each individual element. Now, all computations are done on the rezoned mesh, which reduces mesh distortion as a source of error. On the other hand, the mesh to mesh transfer introduces an artificial diffusion to the solution, which is a source of error. Remeshing is thus a trade off between these two types of error. For the PSSBQ, remeshing at every time step degrades the results due to the diffusion effect described above. Therefore, when remeshing is used for this element, it is done every 10 time steps. On the other hand, the results of the ISBQ improve with more frequent remeshing, and so remeshing for this element is done at every time step. Results are shown in the next section.

4.3.2 Solution Plots and Discussion

Solution plots of the equivalent plastic strain at the time of 1.3 μs are shown in Figure 4.5, with the ISBQ without remeshing shown in the left column, the ISBQ with remeshing at every time step in the center column, and the PSSBQ without

remeshing is in the right column. The Von Mises stress histories are very similar for all elements, however, some differences are very apparent in Figure 4.6 which gives a more detailed look at the convergence of the each element by plotting the equivalent plastic strain history. The plots are taken at the lower left corner of the modeled domain, where the plastic strain is highest, and the PSSBQ on a 220 by 220 mesh without remeshing is used as a reference. The times shown are 1.0 μs to 1.3 μs, since before 1.0 μs there is very little difference in the plots. The results of all methods appear to be converging to the same result, with the PSSBQ converging very quickly. Remeshing at every time step significantly improves the results of the ISBQ, while remeshing every 10 time steps slightly improves the results for the PSSBQ. As mentioned previously, remeshing the PSSBQ at every time steps leads to degraded convergence due to the prevalence of the artificial diffusion caused by the mesh to mesh transfer procedure. The effect of this diffusion decreases with decreasing mesh size however. The Pian Sumihara quad has been shown to have greater robustness under mesh distortion than the irreducible quad for elasticity problems [146]. The same behavior regarding robustness under distortion is observed for the shear band problem. While the PSSBQ will still fail with very severely distorted meshes, the decreased sensitivity of the results to small distortions is clearly advantageous.

Figure 4.7 shows the equivalent plastic strain profile across the shear band at a time of 1.3 μs. Note that for the PSSBQ the width of the shear band, which can be estimated from the figure at 4 - 5 microns, is unchanged with mesh refinement. The ISBQ on the other hand, tends to significantly smear out the shear band with coarser meshes, though with finer meshes, the same width as the PSSBQ is observed. The use of remeshing with ISBQ gives results which match the PSSBQ better at the center of the shear band, but the width and shape of the shear band seem to be slightly altered due to the error introduced by the mesh to mesh transfer.

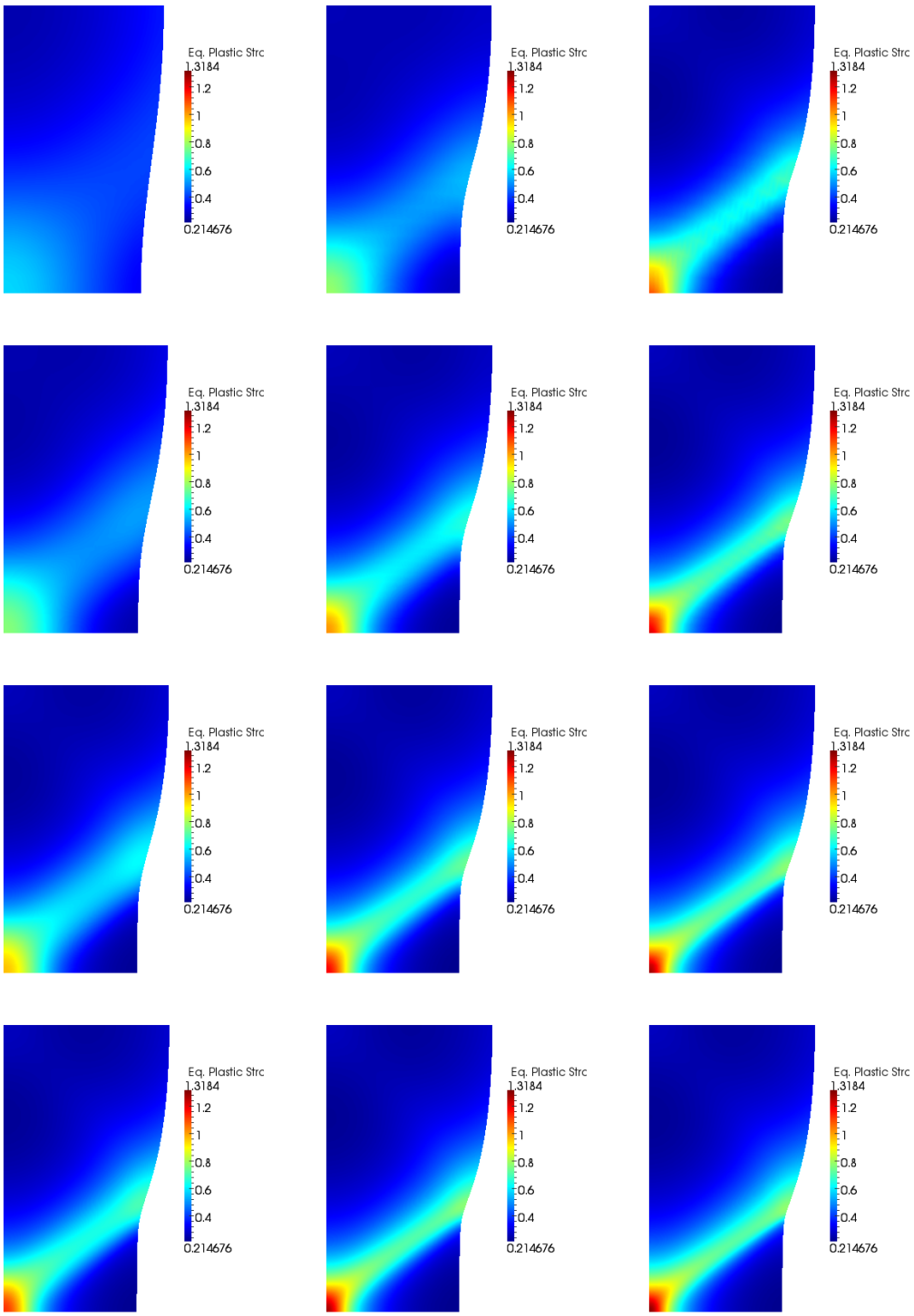

Figure 4.5: Equivalent Plastic Strain Field at 1.3 μs. ISBQ without remeshing is in the left column, ISBQ with remeshing is in the center column, and PSSBQ without remeshing is in the right column

The computational resources required to execute simulations with either of the two elements is ultimately controlled by the linear solution of the system, Eq. (4.51). Contributing to the processing and storage costs are the sparsity structure of the Jacobian, and the number of unknowns in the system. Both elements lead to very sparse Jacobians, owing to the discontinuous functions for stress and equivalent plastic strain. The number of unknowns for the two elements are

$$n_{unknowns}^{ISBQ} = 3n_{nodes} + 20n_{elements} \tag{4.79}$$

$$n_{unknowns}^{PSSBQ} = 3n_{nodes} + 10n_{elements} \tag{4.80}$$

While the size of the linearized system obtained by PSSBQ is significantly smaller compared to ISBQ, the PSSBQ tends to more linear iterations per simulation , which partly negates this benefit, see Figure 4.8 and Table 4.3. Overall, the PSSBQ is slightly faster and slightly less memory intensive when comparing the resources used for a given mesh. When we account for the rate of convergence however, the cost advantage of the PSSBQ becomes very significant. Figure 4.8 shows such a comparison using as an error measure the sum of the errors in the equivalent plastic strain, Von Mises stress, and Temperature with respect to the reference solution run at the lower left corner of the modeled domain. The reference solution is obtained by running the problem with PSSBQ without remeshing on a very fine mesh, consisting of 240 by 240 elements. The error for the PSSBQ on mesh 1 is comparable to the error for the ISBQ on mesh 4, but with the required resources reduced by roughly 2 orders of magnitude.

4.4 Conclusion

A monolithic formulation for simulation of shear bands has been developed. The formulation accounts for large deformations, with an incrementally objective treatment

Table 4.3: Total Linear Iterations

	PSSBQ no rem.	PSSBQ w. rem.	ISSBQ no rem	ISSBQ w. rem
Mesh1	411	414	385	409
Mesh2	414	418	395	410
Mesh3	418	419	398	408
Mesh4	419	419	398	404

of the hypoplastic constitutive law. Two elements have been assessed, the first is the Irreducible Shear Band Quad (ISBQ), which employs the same interpolation as the four noded quad used in irreducible finite elements, but with the history variables updated simultaneously with the displacements and temperatures. The $\bar{F}$ method was implemented with the ISBQ to prevent volumetric locking. The second is the Pian Sumihara Shear Band Quad (PSSBQ), a mixed, assumed stress element which again employs a fully monolithic constitutive update. The incrementally objective, algorithmic approximation to the Lie derivative of Kirchhoff stress was derived for this element. The formulation was linearized analytically at the time discrete level, to provide an exact Jacobian.

Both elements were implemented in FEAP and run on a test problem: a plate in plane strain tension with four meshes of increasing refinement. Both elements appear to be converging to the same result, but the PSSBQ, likely owing to its robustness under distorted meshes, converged faster than the ISBQ. The elements were also implemented with a remeshing procedure, which improved performance by minimizing mesh distortions, but also introduced a diffusive error as solution variables were transferred from the old mesh to the new mesh. Future work will continue to evaluate the most efficient interpolations and mesh-to-mesh transfer operators for the monolithic shear band formulation.

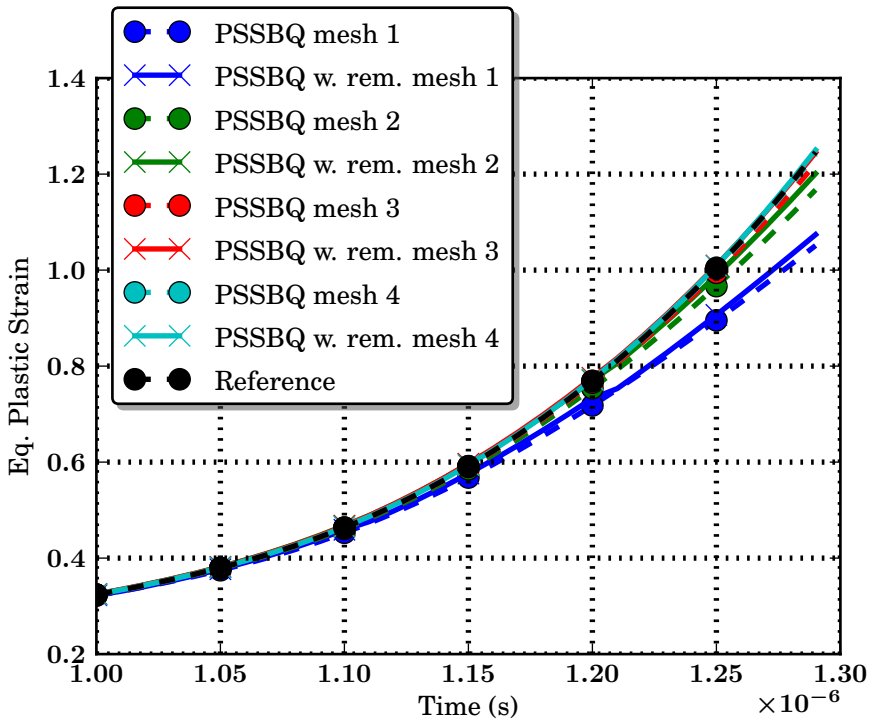

(a) PSSBQ without remeshing and PSSBQ with remeshing

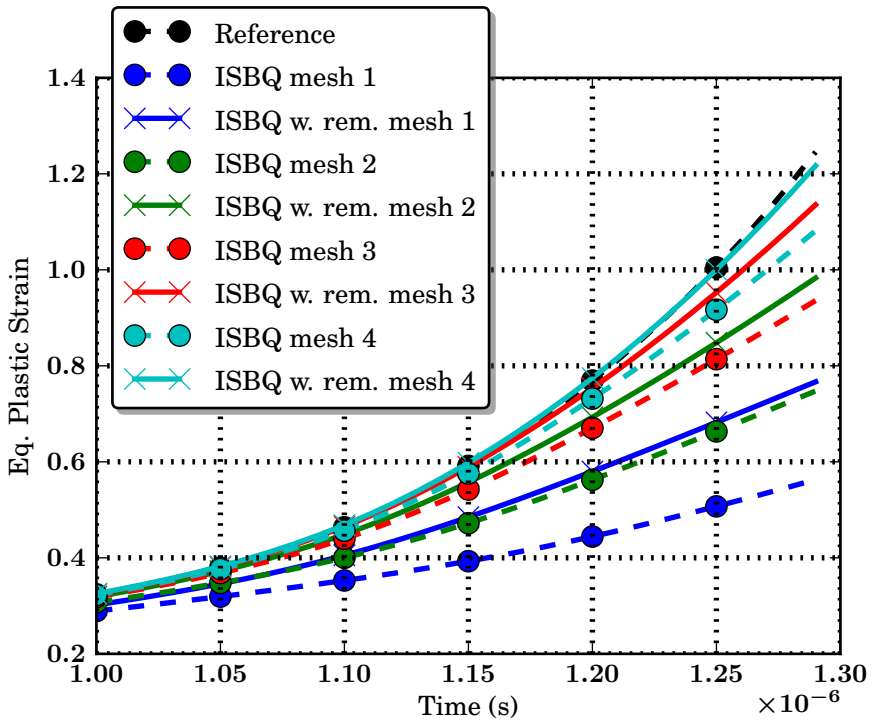

(b) ISBQ without remeshing and ISBQ with remeshing

Figure 4.6: Equivalent Plastic Strain vs Time at the lower left corner of the modeled domain 100 remeshing steps were taken when remeshing was used with the ISBQ and 10 remeshing steps were taken when remeshing was used with the PSSBQ

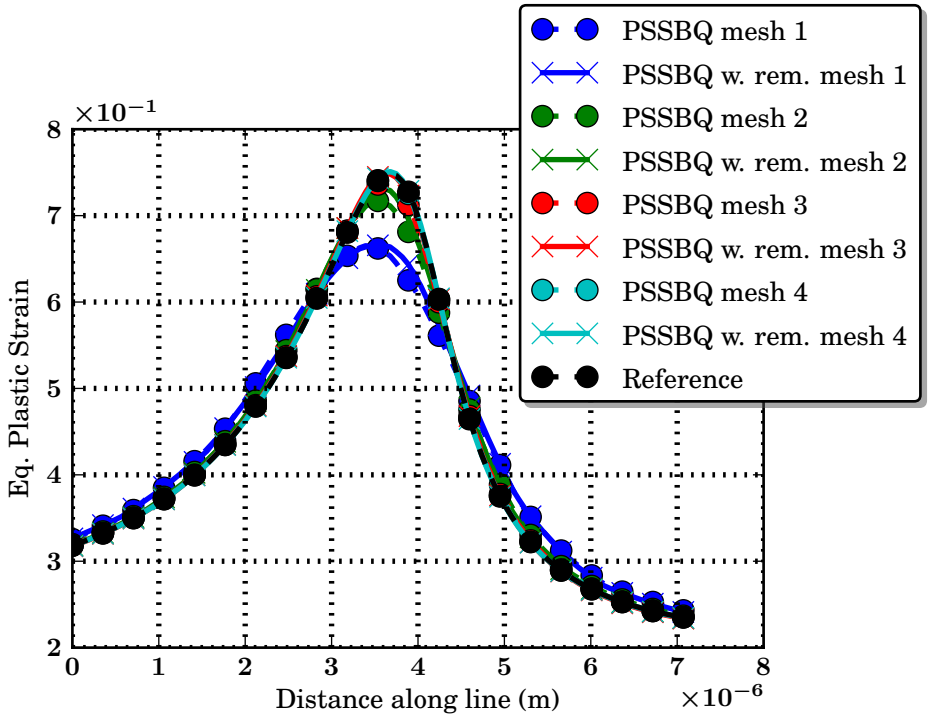

(a) PSSBQ without remeshing and PSSBQ with remeshing

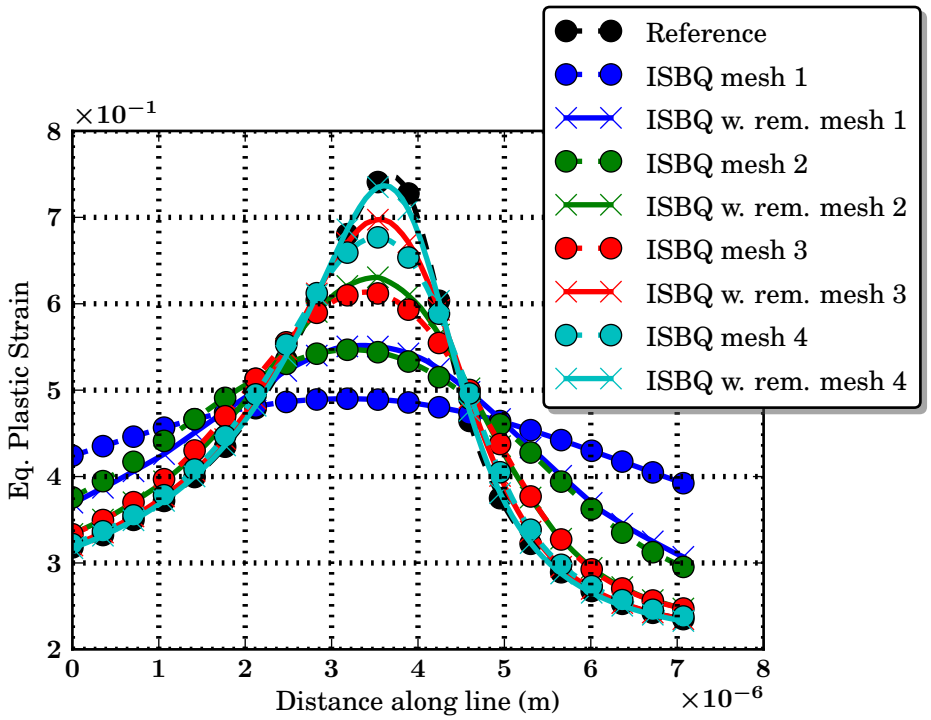

(b) ISBQ without remeshing and ISBQ with remeshing

Figure 4.7: Equivalent Plastic Strain across the shear band, the time is 1.3 μs

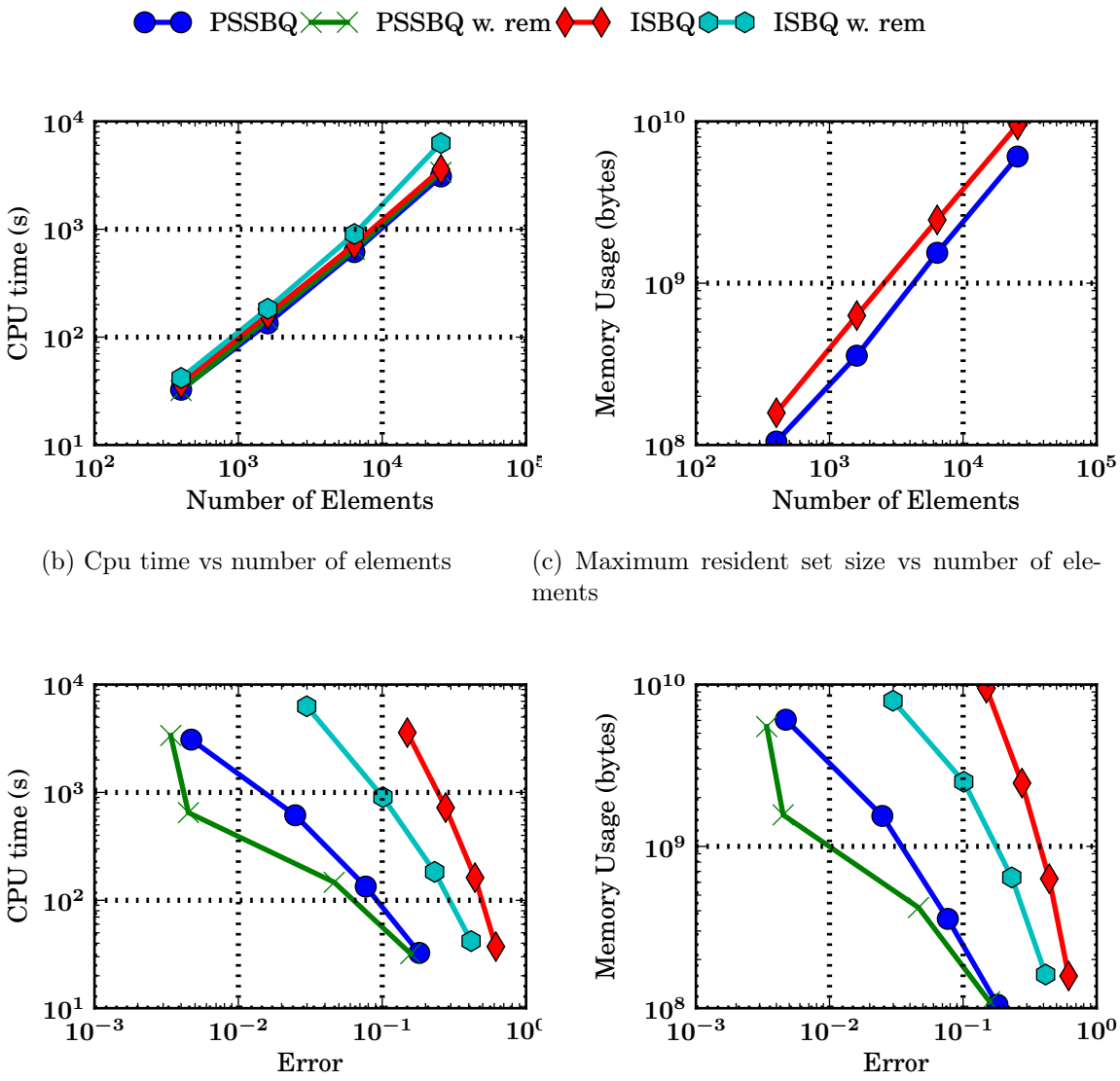

(b) Cpu time vs number of elements

(c) Maximum resident set size vs number of elements

(d) Cpu time required to achieve a given level of error compared to the reference

(e) Memory required to achieve a given level of error compared to the reference

Figure 4.8: Timings and iteration counts

Chapter 5

A Unified Model for Metal Failure Capturing Shear Banding and Fracture

In this chapter a combined thermal softening shear banding and phase field fracture model is presented. The shear band model consists of an elastic - viscoplastic, strain hardening, strain rate hardening, and thermally softening material. Thermal diffusion is accounted for, which weakly defines a length scale and regularizes the problem. This type of model and diffusive regularization have been studied in references [13, 16, 17, 19, 20, 99, 100, 140]. Fracture is accounted for with the phase field method, which is a regularized Griffith type [61] fracture model based on energy minimization [34, 56, 103, 104]. The crack is approximated as a continuous entity, whose width is defined by a small process zone parameter, see Figure 1.1. It is thus possible to approximate the fracture energy with a volume integral, which does not require a procedure for tracking the crack surface. It has been shown in [33, 56] that in the limit as the process zone parameter tends to zero, the phase field approximation to

the fracture energy converges to that of the discontinuous crack. Phase field models have been extended to account for dynamic brittle fracture in references [31, 35].

Growth of cracks in the phase field models cited above is driven by the elastic free energy. The elastic energy can then be split into portions which contribute to fracture and portions which do not. For example [31, 103, 104] decompose the strain energy using the principal strains, where only the tensile principal strains contribute to fracture. Inelasticity has been introduced to the phase field model by [32] who combined the phase field model for dynamic fracture with the finite deformation plasticity models in [124]. In addition, modeling of thermo mechanical damage in tungsten subject to conditions found in a fusion reactor was conducted by [44], who combined the phase field model with small deformation plasticity. For an inelastic material, the growth of the elastic free energy will be limited by yielding; in fact the elastic free energy can decrease once thermal softening begins. For metals, where the inelastic response is independent of volumetric deformations, it is conceivable that the elastic free energy due to tensile volumetric deformation will be large enough to initiate a crack. However, the contribution of the extensive inelastic working that occurs during the shear banding process will not be modeled. To remedy this, the model presented here includes an enhancement of the phase field model to account for the contribution of energy of internal inelastic variables to the fracture energy. This leads to the addition of source terms in the phase field evolution equation which are due to inelastic deformation.

An interesting aspect of this enhancement to the phase field model is the partition of the inelastic work into heat and cold work, which is energy stored by defects in the metal's lattice [28]. In the present model, heat production drives thermal softening and shear bands, while cold work terms along with the elastic energy drives cracks. The partition of the inelastic work is thus significant in determining the eventual mode of failure. Citing the experimental work of [55, 130], shear band models nearly

universally assume that the fraction of inelastic work converted to heat is a constant in the neighborhood of 0.9. This constant is frequently referred to as the Taylor Quinney fraction. However, more recent experiments by [68, 95, 98] have convincingly demonstrated that the fraction of inelastic work converted to heat depends on strain, strain rate and temperature. Furthermore, theoretical objections to constant partition of inelastic work have been pointed out in [138].

Several studies have been conducted which aim to theoretically or experimentally determine the partition of inelastic work. Early examples are [6], where an expression for the partition is derived from residual stress theory, [142]. More recently, [122] used a dislocation density strain hardening model within a thermodynamic framework similar to the one presented here to model the stored energy. Another approach is that of [40], calculated the stored energy of cold work from dislocation theory and incorporated this into a crystal plasticity, high rate failure model. A dislocation theory approach was also taken in [27], who concluded that the stored energy of cold work depends not only on the dislocation density but on the dislocation structure as well. A method for experimental determination of the partition is given in [69], where the stored energy of cold work as a function of plastic strain for a few metal alloys is calculated from the experiments of [68]. Lastly, [90, 91] calculate the partition from the phenomenological plasticity model employed therein.

Using a rigid plastic model, Wright and Walter [140] studied the strain to failure of a thermal softening, rate dependent material over several decades of strain rate. This is illustrated here in Figure 5.1. The failure strain plotted against the strain rate results in a U shape, since thermal diffusion inhibits localization at low strain rates, and inertia inhibits it at high strain rates. This leaves a range of strain rates where thermal softening shear bands occur most readily, which will be referred to in this work as the critical shear band zone (zone 3 in Figure 5.1). Other zones on the U curve are the diffusion stabilized zone (zone 1 in Figure 5.1), where no localization

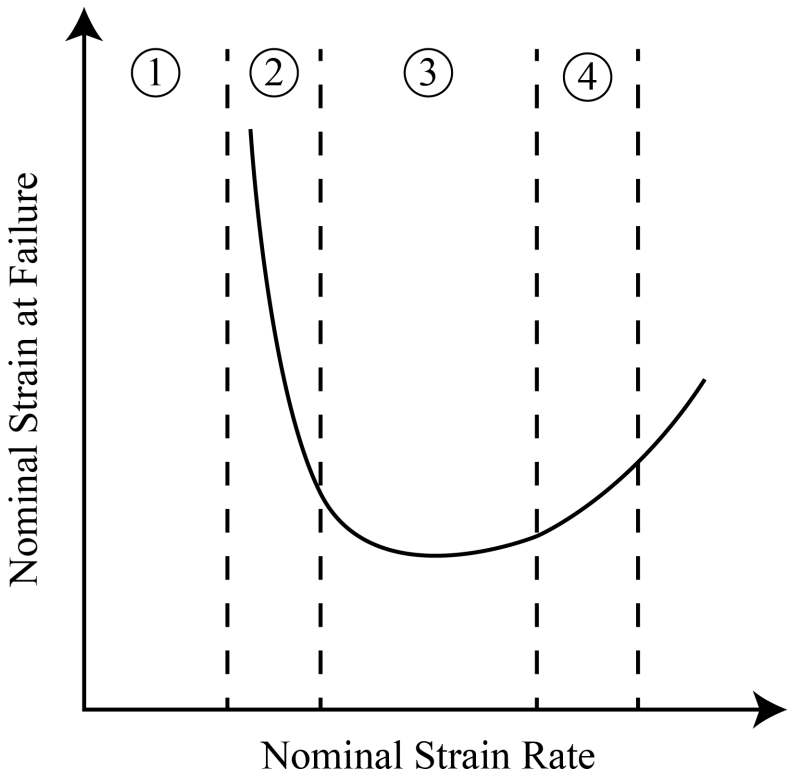

Figure 5.1: Schematic illustration of the results reported in [140], for a rigid plastic model. Zone 1 is the diffusion stabilized zone, where thermal diffusion is able to prevent severe localization due to the slow loading rate. Zone 2 is the first transition zone, where severe localization occurs at increasingly low strains. Zone 3 is the critical shear band zone, where thermal softening failure is most prevalent. Lastly, zone 4 is the second transition zone, where inertia effects become important. Inertia has been shown to delay shear localization [57]

occurs, and the two transition zones on either side of the critical shear band zone (zones 2 and 4 in Figure 5.1). Further studies on the effect of strain rate on shear banding have been conducted by [57, 60].

In the numerical experiments shown in this study, a constant partition of the inelastic work is assumed, and the failure strain and energy dissipation of a one dimensional model is studied over a wide range of strain rates and values of the Taylor Quinney fraction. Significant differences in the failure behavior of the shear band, and combined model are present in all zones except the critical shear band

zone. Of particular interest are the transition zones, where differences between the two formulations becomes most important for high rate failure modeling.

5.1 Proposed Model Derivation

In this section the proposed modeling framework is developed. The combined phase field and shear band model consists of macro and micro force balance equations, the energy balance equation, and the entropy inequality. In addition, elastic and inelastic constitutive relations are needed. A brief review of the requisite kinematics is given before developing the governing equations.

5.1.1 Kinematics

The decompositions of F_{iA}, l_{ij}, and d_{ij} used in this chapter are the same as those used in chapter 4. Some additional kinematic quantities will be needed, the first being the elastic Right Cauchy Green tensor, defined as

$$C^e_{qr} = F^e_{kq} F^e_{kr} \tag{5.1}$$

giving the elastic Green strain as

$$E^e_{qr} = \frac{1}{2}\left(C^e_{qr} - \delta_{qr}\right) \tag{5.2}$$

Differentiating (5.2) with respect to time gives the rate of Green strain

$$\dot{E}^e_{qr} = \frac{1}{2}\left(\dot{F}^e_{kq} F^e_{kr} + F^e_{kq} \dot{F}^e_{kr}\right) \tag{5.3}$$

Note that the first and second terms of this equation can be written respectively as

$$\dot{F}^e_{kq}F^e_{kr} = F^e_{iq}\dot{F}^e_{ja}F^{e,-1}_{ai}F^e_{jr} = F^e_{iq}l^e_{ji}F^e_{jr} \tag{5.4}$$

$$F^e_{kq}\dot{F}^e_{kr} = F^e_{iq}\dot{F}^e_{ia}F^{e,-1}_{aj}F^e_{jr} = F^e_{iq}l^e_{ij}F^e_{jr} \tag{5.5}$$

and thus the elastic deformation rate and the rate of elastic Green strain have the relation

$$\dot{E}^e_{qr} = \frac{1}{2}F^e_{iq}\left(l^e_{ji} + l^e_{ij}\right)F^e_{jr} = F^e_{iq}d^e_{ij}F^e_{jr} \tag{5.6}$$

5.1.2 Balance laws and entropy inequality

There are three balance laws governing the physical system. They are the macro force balance, the micro force balance, and the energy balance. In addition, the entropy inequality must be satisfied. The macro force balance is

$$\rho_0\ddot{u}_i = P_{iI,I} + B_i \tag{5.7}$$

where ρ_0 is the reference density, u_i is the displacement, B_i is the body force per reference volume, and P_{iA} is the first Piola Kirchhoff stress. Cracks, which are characterized by the phase field parameter c, are assumed to evolve under the influence of micro forces [128], which are governed by the following equation

$$\rho_0\theta\ddot{c} = H_{I,I} - K + G \tag{5.8}$$

Here, θ is the micro inertia, which accounts for the local inertia of accelerating material at the crack tip. The external micro force, G, which may be used to model bond breakage due to reactive materials or internally pressurized cracks. The internal micro force is denoted as K, which is the main driving force of the crack. It will be shown later that K depends on the elastic free energy and, a novel feature of

the present model, the stored energy of internal inelastic variables. Lastly, H_I is the micro traction.

The energy balance law is given by

$$\rho_0 \dot{e} = S_{IJ}\dot{E}_{IJ} + K\dot{c} + H_I \dot{c}_{,I} + \rho_0 R - Q_{I,I} \tag{5.9}$$

where S_{IJ} is the second Piola Kirchhoff stress, $\dot{E}_{IJ}$ is the rate of Green strain, R is the heat supply and Q_I is the heat flux through the reference area.

Lastly the entropy inequality is [97]

$$\rho_0 \dot{\eta} \geq \left(\frac{Q_I}{T}\right)_{,I} + \rho_0 \frac{R}{T} \tag{5.10}$$

where η is the specific entropy, and T is the temperature.

The free energy per unit mass is

$$\psi = e - T\eta \tag{5.11}$$

or in rate form

$$\dot{\psi} = \dot{e} - \dot{T}\eta - T\dot{\eta} \tag{5.12}$$

Substituting (5.12) into (5.10)

$$S_{IJ}\dot{E}_{IJ} + H_I \dot{c}_{,I} + K\dot{c} - \rho_0 \left(\dot{\psi} + \dot{T}\eta\right) \geq \frac{Q_I T_{,I}}{T} \tag{5.13}$$

The terms on the left hand side account for the internal energy dissipation per unit reference volume, $\mathcal{D} \geq 0$ so that

$$\mathcal{D} = \tau_{ij} d_{ij} + H_I \dot{c}_j + K\dot{c} - \rho_0 \left(\dot{\psi} + \dot{T}\eta\right) \tag{5.14}$$

where we have used the identity $S_{IJ}\dot{E}_{IJ} = \tau_{ij}d_{ij}$, with τ_{ij} being the Kirchhoff stress. The rate of deformation d_{ij} and conjugate stress measure τ_{ij} are convinient because it permits the use of the additive decomposition in (4.4). using (5.14), along with (5.12), the energy equation (5.9) can be written in an alternative form, which will prove to be convenient later

$$\rho_0 T\dot{\eta} = \mathcal{D} - Q_{I,I} + \rho_0 R \tag{5.15}$$

Using the additive decomposition of d_{ij} in (4.4), the stress power term in (5.13) is expanded so that entropy inequality becomes

$$\tau_{ij}d^e_{ij} + \tau_{ij}d^t_{ij} + \tau_{ij}d^p_{ij} + H_I\dot{c}_{,j} + K\dot{c} - \rho_0\left(\dot{\psi} + \dot{T}\eta\right) \geq \frac{Q_I T_{,I}}{T} \tag{5.16}$$

the elastic part of the stress power, using (5.6) can alternatively be written as

$$\tau_{ij}d^e_{ij} = \tau_{ij}F^{e,-1}_{qi}F^{e,-1}_{rj}\dot{E}^e_{qr} \tag{5.17}$$

also the thermal part of the stress power can be replaced with

$$\tau_{ij}d^t_{ij} = \tau_{ij}\delta_{ij}\alpha\dot{T} \tag{5.18}$$

Where α is the coefficient of thermal expansion. Defining the elastic second Piola Kirchhoff stress, which is the second Piola Kirchhoff stress with respect to the elastic configuration, as

$$S^e_{qr} = \tau_{ij}F^{e,-1}_{qi}F^{e,-1}_{rj} \tag{5.19}$$

Eq. (5.17) can be written as

$$\tau_{ij}d^e_{ij} = S^e_{qr}\dot{E}^e_{qr} = \frac{1}{2}S^e_{qr}\dot{C}^e_{qr} \tag{5.20}$$

substituting (5.20) into the entropy inequality (5.16) gives

$$\frac{1}{2}S^e_{qr}\dot{C}^e_{qr} + \tau_{ij}\delta_{ij}\alpha\dot{T} + \tau_{ij}d^p_{ij} + H_I\dot{c}_{,I} + K\dot{c} - \rho_0\left(\dot{\psi} + \dot{T}\eta\right) \geq \frac{Q_I T_{,I}}{T} \tag{5.21}$$

Now, the free energy is assumed to be a function of elastic right Cauchy Green tensor C^e_{ij}, T, c, $c_{,j}$, and n internal variables ξ_i for $i = 1,\ n$ so that

$$\psi = \psi\left(C^e, T, c, c_{,j}, \xi_1, \ldots, \xi_n\right) \tag{5.22}$$

The internal variables quantify microstructural details of the material which affect the mechanical response [120]. Common examples of internal variables are dislocation density, isotropic hardening parameter, and back stress [110]. The time derivative of the free energy is now

$$\dot{\psi} = \left(\partial_{C^e}\psi\right)_{qr}\dot{C}^e_{qr} + \partial_T\psi\dot{T} + \partial_c\psi\dot{c} + \partial_{c,I}\psi\dot{c}_{,I} + \sum_{i=1}^{n}\Xi_i\dot{\xi}_i \tag{5.23}$$

Where the $\Xi_i = \partial_{\xi_i}\psi$ are the thermodynamic forces conjugate to the ξ_i. substituting this into (5.21) gives

$$\begin{aligned}\mathcal{D} = &\left(S^e_{qr} - 2\rho_0\left(\partial_{C^e}\psi\right)_{qr}\right)\dot{C}^e_{qr} + \left(\tau_{kk}\alpha - \rho_0\partial_T\psi - \rho_0\eta\right)\dot{T} \\ &+ \left(K - \rho_0\partial_c\psi\right)\dot{c} + \left(H_I - \rho_0\partial_{c,I}\psi\right)\dot{c}_{,I} + \tau_{ij}d^p_{ij} - \rho_0\sum_{i=1}^{n}\Xi_i\dot{\xi}_i \\ &\geq \frac{Q_I T_{,I}}{T}\end{aligned} \tag{5.24}$$

Since the above inequality should hold for an arbitrary thermodynamic process, which is to say that $\dot{E}_{qr}$, $\dot{T}$, $\dot{c}$, $\dot{c}_{,I}$ can assume arbitrary values, the coefficients of these values should be zero so that

$$S^e_{qr} = 2\rho_0\left(\partial_{C^e}\psi\right)_{qr} \tag{5.25}$$

$$H_I = \rho_0 \partial_{c,I} \psi \tag{5.26}$$

and

$$\eta = \tau_{kk} \frac{\alpha}{\rho_0} - \partial_T \psi = \Pi - \partial_T \psi \tag{5.27}$$

We assume the internal micro force K is given in the form

$$K = K^* \left(E_{IJ}, \dot{E}_{IJ}, c, \dot{c}, c_{,I}, T \right) + \rho_0 \partial_c \psi \tag{5.28}$$

Where K^* is a dissipation function. The dissipation is now

$$\mathcal{D} = \mathcal{D}^p + \mathcal{D}^f \geq 0 \tag{5.29}$$

$$\mathcal{D}^p = \tau_{ij} d^p_{ij} - \rho_0 \sum_{i=1}^{n} \Xi_i \dot{\xi}_i \geq 0 \tag{5.30}$$

$$\mathcal{D}^f = K^* \dot{c} \geq 0 \tag{5.31}$$

Where $\mathcal{D}^p$ and $\mathcal{D}^f$ are the contributions to the dissipation from inelasticity and fracture respectively. The inelastic dissipation is thus interpreted as the inelastic stress power less the rate of energy stored by changing internal variables. In light of (5.27), the rate of entropy production can be expanded using the chain rule

$$\dot{\eta} = \partial_T \Pi \dot{T} - \left[\left(\partial_{TC^e} \psi \right)_{qr} \dot{C}^e_{qr} + \partial_{TT} \psi \dot{T} + \partial_{Tc} \psi \dot{c} + \partial_{Tc,I} \psi \dot{c}_{,I} + \sum_{i=1}^{n} \partial_T \Xi_i \dot{\xi}_i \right] \tag{5.32}$$

substitution of (5.29) and (5.32) into the energy equation (5.15) leads to

$$\begin{aligned} \rho_0 T \left(\partial_T \Pi - \partial_{TT} \psi \right) \dot{T} = {} & \rho_0 T \left(\partial_{TC^e} \psi \right)_{qr} \dot{C}^e_{qr} + \tau_{ij} d^p_{ij} - \rho_0 \sum_{i=1}^{n} \left(\Xi_i - T \partial_T \Xi_i \right) \dot{\xi}_i \\ & + \rho_0 T \partial_T H_I \dot{c}_I + \rho_0 T \partial_T K \dot{c} + K^* \dot{c} \\ & - Q_{I,I} + \rho_0 R \end{aligned} \tag{5.33}$$

We let the specific heat be a constant, defined as

$$\hat{c} = \frac{\partial e}{\partial T} = \frac{\partial e}{\partial \eta}\frac{\partial \eta}{\partial T} = T\left(\frac{\partial \Pi}{\partial T} - \frac{\partial^2 \psi}{\partial T^2}\right) = constant \tag{5.34}$$

The energy equation can thus be written as

$$\begin{aligned}\rho_0 \hat{c}\dot{T} = {} & \rho_0 T \left(\partial_{TC^e}\psi\right)_{qr} \dot{C}^e_{qr} + \tau_{ij} d^p_{ij} - \rho_0 \sum_{i=1}^{n} \left(\Xi_i - T\partial_T \Xi_i\right) \dot{\xi}_i \\ & + \rho_0 T \partial_T H_I \dot{c}_I + \rho_0 T \partial_T K \dot{c} + K^* \dot{c} \\ & - Q_{I,I} + \rho_0 R \end{aligned} \tag{5.35}$$

This equation accounts for heat storage, thermo elastic heating, inelastic work, energy storage by internal variables, reversible and dissipative heat generation due to fracture, thermal diffusion, and heat supply.

5.1.3 Specification of the Free Energy

The constitutive relations now depend on the specified form of the elastic and fracture contributions to the free energy. We use a general form, where the free energy is additively decomposed into thermal, elastic, fracture, and internal variable parts: ψ^t, ψ^e, ψ^f, and ψ^ξ respectively, giving

$$\psi = \psi^t + \psi^e + \psi^f + \psi^\xi \tag{5.36}$$

The elastic and internal variable portions are further broken into portions which contribute to fracture and portions which do not. Splitting the free energy is typically done to permit modeling of fracture in tension only. In accordance with the constant specific heat assumption eq. (5.34), the thermal part of the free energy is given by

[40]

$$\rho_0 \psi^t = -\rho_0 \hat{c} T \log T/T_0 \tag{5.37}$$

The elastic part of the free energy is

$$\rho_0 \psi^e = W + [m(c) - 1] W^+ \tag{5.38}$$

Where W is a function of the elastic deformation and the elastic material properties and W^+ is the damaged free energy. The degradation function $m(c)$ models the loss of strength in the material due to fracture, and is often chosen to be a quadratic. Note that this is notationally different from most phase field models where the elastic free energy is defined as

$$\rho_0 \psi^e = W^- + m(c) W^+ \tag{5.39}$$

Where W^- is the undamaged free energy. The reason for this difference is that the resulting definition of the elastic second Piola Kirchhoff stress, after using equation (5.25) in equation (5.38), will look familiar to the shear band only model, but with an additional term appended accounting for degradation of the stress due to fracture. Examples of W used in the literature for small strain analysis are a volumetric - deviatoric split of the strain energy used in [5], which is

$$W = \frac{1}{2} C^{elas}_{ijkl} \epsilon_{ij} \epsilon_{kl} \tag{5.40}$$

$$W^+ = (\lambda + 2\mu/3) \left\langle \epsilon^2_{ii} \right\rangle + \mu \epsilon^{dev}_{ij} \epsilon^{dev}_{ij} \tag{5.41}$$

Where ϵ_{ij} is the small strain tensor, the deviatoric strain tensor is $\epsilon^{dev}_{ij} = \epsilon_{ij} - \frac{1}{3}\epsilon_{kk}\delta_{ij}$, λ and μ are Lame's constants, and $\langle\ \rangle$ are Macaulay brackets, defined as

$$\langle x \rangle = \begin{cases} 0, & \text{if } x \leq 0 \\ x, & \text{if } x > 0 \end{cases} \tag{5.42}$$

In this split tensile volumetric and deviatoric strains contribute to damage. The finite deformation analogue of this split was used in a phase field model with plasticity in [32].

A second popular split, used in [31, 103, 104] is based on principal strains so that

$$W^+ = \frac{\lambda}{2}\left\langle \epsilon_1^{pr} + \epsilon_2^{pr} + \epsilon_3^{pr} \right\rangle^2 + \mu\left(\left\langle \epsilon_1^{pr}\right\rangle^2 + \left\langle \epsilon_2^{pr}\right\rangle^2 + \left\langle \epsilon_3^{pr}\right\rangle^2\right) \tag{5.43}$$

where the principal strains ϵ_a^{pr} and principal directions p_a are given by the spectral decomposition of the small strain tensor

$$\epsilon = \epsilon_{ij} e_i \otimes e_j = \sum_{a=1}^{3} \epsilon_a^{pr} p_a \otimes p_a \tag{5.44}$$

The fracture energy is given by the phase field theory [34, 56, 103, 104] as

$$\rho_0 \psi^f = \mathcal{G}_c \left[\frac{c^2}{4l_0} + l_0 c_{,I} c_{,I}\right] \tag{5.45}$$

As noted earlier, the phase field approximation to the fracture energy converges to that of the discontinuous crack in the limit as the process zone parameter l_0 goes to zero [33, 56]. Lastly, the free energy due to internal variables is

$$\rho_0 \psi^\xi = \sum_{i=1}^{n} \left(\Xi_i \xi_i + \left[m(c) - 1\right] \Xi_i \xi_i^+\right) \tag{5.46}$$

Where the ξ_i^+ are the internal variables whose evolution contributes to fracture. Thus, this modeling framework allows the choice of which internal variables contribute to the generation of fracture surfaces and which do not. In addition, similar to the notion of splitting the elastic free energy, the contribution of a single internal variable may be split into a fracture producing part and a non fracture producing part. This is where the present formulation departs significantly from existing phase field models

which incorporate plasticity [32, 44], and as shown below, these contributions to the free energy will lead to additional source terms in the phase field evolution equation. The physical motivation for inclusion of these terms in the modeling framework is due to the well known relationship between fracture and barriers to dislocation motion such as dislocation density and grain size. This leads to a model for fracture which is explicitly rate and temperature dependent, due to the rate and temperature dependence of the internal variables.

Adopting as an example a volumetric - deviatoric split of the elastic strain energy [124], the elastic second Piola Kirchhoff stress, and thus the Kirchhoff stress, can be determined. The elastic energy is thus composed of a volumetric contribution $U\left(J^e\right)$, dependent on the elastic volume change J^e, and a deviatoric contribution $\bar{W}\left(\bar{C}^e_{qr}\right)$, dependent on the deviatoric part of elastic right Cauchy Green tensor $\bar{C}^e_{qr} = J^{e,-2/3}F^e_{kq}F^e_{kr}$. W, U, and $\bar{W}$ are defined as

$$W = U\left(J^e\right) + \bar{W}\left(\bar{C}^e_{qr}\right) \tag{5.47}$$

$$U\left(J^e\right) = \frac{1}{2}k\left[\frac{1}{2}\left(J^{e,2}-1\right) - \ln J^e\right] \tag{5.48}$$

$$\bar{W}\left(\bar{C}^e_{qr}\right) = \frac{1}{2}\mu\left(\text{trace}\left[\bar{C}^e_{qr}\right] - 3\right) \tag{5.49}$$

W is split so that W^+, the fracture producing portion, depends on the volumetric expansion so that

$$W^+ = \begin{cases} 0, & \text{if } J^e \leq 0 \\ U\left(J^e\right), & \text{if } J^e > 0 \end{cases} \tag{5.50}$$

Using (5.25) with the above definitions and the relation $\tau_{ij} = S^e_{qr}F^e_{iq}F^e_{jr}$ the Kirchhoff stress becomes

$$\tau_{ij} = \tau^{sb}_{ij} + \tau^f_{ij} \tag{5.51}$$

Where τ_{ij}^{sb} is the contribution of the familiar elastic - plastic material law, and is defined as

$$\tau_{ij}^{sb} = \frac{k}{2}\left(J^{e,2}-1\right)\delta_{ij} + \mu \text{dev}\left[\bar{b}^{e}\right] \tag{5.52}$$

Where $\text{dev}\left[\bar{b}_{ij}^{e}\right]$ is the deviatoric part of the tensor $\bar{b}_{ij}^{e} = J^{e,-2/3}F_{iq}^{e}F_{jq}^{e}$, with the elastic left Cauchy Green tensor being $b_{ij}^{e} = F_{iq}^{e}F_{jq}^{e}$. The decrement in stress due to cracking τ_{ij}^{f} is then

$$\tau_{ij}^{f} = \begin{cases} 0, & \text{if } J^{e} \leq 0 \\ \left[m(c)-1\right]\frac{k}{2}\left(J^{e,2}-1\right)\delta_{ij}, & \text{if } J^{e} > 0 \end{cases} \tag{5.53}$$

There are other options for splitting the energy, for example the deviatoric part of the elastic free energy can be included, which would result in an extra term in τ_{ij}^{f}

With the elastic constitutive relation specified, the terms micro force balance must now be developed. The micro force traction in the present formulation is identical to that of other phase field models. This is

$$H_I = \rho_0 \frac{\partial \psi}{\partial c_{,I}} = 2\mathcal{G}_c l_0 c_{,I} \tag{5.54}$$

However, the internal micro force contains extra source terms as follows

$$K = \rho_0 \frac{\partial \psi}{\partial c} + K^{*} = \frac{\partial m}{\partial c}\left(W^{+} + \sum_{i=1}^{n}\Xi_i \xi_i^{+}\right) + \mathcal{G}_c \frac{c}{2l_0} + K^{*} \tag{5.55}$$

Now, substituting (5.54) and (5.55) into (5.8) the micro force strong form becomes

$$\rho_0 \theta \ddot{c} = 4l_0 c_{,II} - c - \frac{2l_0}{\mathcal{G}_c}\frac{\partial m}{\partial c}\left(W^{+} + \sum_{i=1}^{n}\Xi_i \xi_i^{+}\right) - \frac{2l_0}{\mathcal{G}_c}K^{*} \tag{5.56}$$

Note that the addition of the terms $\sum_{i=1}^{n}\Xi_i \xi_i^{+}$ results in the possibility of cracking due to evolving internal inelastic variables, in contrast to the classical phase field method, where only the elastic free energy W^{+} contributes to fracture.

The final equations needed for the strong form are the inelastic constitutive equations. The equivalent plastic strain evolves according to the following equation

$$\dot{\bar{\gamma}}^p = \sqrt{\frac{2}{3} d^p_{ij} d^p_{ij}} \tag{5.57}$$

Since metal plasticity is considered here, the inelastic response is independent of volumetric deformation and thus the inelastic rate of deformation can be simplified to

$$d^p_{ij} = \frac{3 s_{ij}}{2\bar{\tau}} g\left(\bar{\tau}, T, \xi_i\right) \tag{5.58}$$

where $s_{ij} = \tau_{ij} - \frac{1}{3}\tau_{kk}\delta_{ij}$ is the deviatoric Kirchhoff stress and $\bar{\tau} = \sqrt{\frac{3}{2} s_{ij} s_{ij}}$ is the effective Kirchhoff stress. Using (5.58) in (5.57) gives

$$\dot{\bar{\gamma}}^p = g\left(\bar{\tau}, T, \xi_i\right) \tag{5.59}$$

Where the constitutive function $g\left(\bar{\tau}, T, \xi_i\right)$ gives the equivalent plastic strain rate as a function of stress, temperature and internal variables. Lastly, the constitutive relations for the ξ_i are [120]

$$\dot{\xi}_i = \mathcal{X}_i\left(\bar{\tau}, T, \xi_i\right) \tag{5.60}$$

An example of which, that has been used for shear band modeling by [17] is (using the present notation)

$$\dot{\xi} = \bar{\tau}\dot{\bar{\gamma}}^p / \left(1 + \xi/\xi_0\right)^n \tag{5.61}$$

In this case, there is one internal variable ξ which represents the extent of work hardening in the material.

Putting all of these equations together, the strong form consists of the balance laws

$$\rho_0 \ddot{u}_i = P_{iI,I} + B_i \tag{5.62}$$

$$\rho_0 \hat{c} \dot{T} = \rho_0 T \left(\partial_{TE^e} \psi\right)_{qr} \dot{E}^e_{qr} + \bar{\tau} g\left(\bar{\tau}, T, \xi_i\right) - \rho_0 \sum_{i=1}^{n} \left(\Xi_i - T \partial_T \Xi_i\right) \dot{\xi}_i$$

$$+ K^* \dot{c} - Q_{I,I} + \rho_0 R \tag{5.63}$$

$$\rho_0 \theta \ddot{c} = 4 l_0 c_{,II} - c - \frac{2 l_0}{\mathcal{G}_c} \frac{\partial m}{\partial c} \left(W^+ + \sum_{i=1}^{n} \Xi_i \xi_i^+ \right) - \frac{2 l_0}{\mathcal{G}_c} K^* \tag{5.64}$$

and the constitutive relations

$$\tau_{ij} = \tau^{sb}_{ij} + \tau^f_{ij} \tag{5.65}$$

$$\tau^{sb}_{ij} = \frac{k}{2}\left(J^{e,2} - 1\right)\delta_{ij} + \mu \mathrm{dev}\left[\bar{b}^e\right] \tag{5.66}$$

$$\tau^f_{ij} = \begin{cases} 0, & \text{if } J^e \leq 0 \\ \left[m(c) - 1\right] \frac{k}{2}\left(J^{e,2} - 1\right)\delta_{ij}, & \text{if } J^e > 0 \end{cases} \tag{5.67}$$

$$\dot{\bar{\gamma}}^p = g\left(\bar{\tau}, T, \xi_i\right) \tag{5.68}$$

$$\dot{\xi}_i = \mathcal{X}_i\left(\bar{\tau}, T, \xi_i\right) \tag{5.69}$$

5.2 1D Numerical Solutions With Constant Partition of Inelastic Work

To illustrate the basic behavior of the present model, several numerical experiments in one dimension are given below. Small strains are considered so that all stress measures are equivalent, and represented by σ_{ij}. There is no micro inertia or fracture dissipation, i.e. $\theta = 0$ and $K^* = 0$. A quadratic degradation function is employed: $m(c) = (1-c)^2$, which is the most commonly used degradation function, though

others are available, subject to certain restrictions [32]. The equivalent plastic strain is taken as the only internal variable, and represents the extent of work hardening of the material. As pointed out in the introduction, in general the Taylor Quinney fraction is not a material constant but depends on strain, strain rate, and temperature, as shown experimentally by [68, 98]. According to the previous section, the fraction of inelastic work converted to heat is

$$\chi = 1 - \frac{\rho_0 \sum_{i=1}^{n} \left(\Xi_i - T\partial_T \Xi_i\right) \dot{\xi}_i}{\bar{\sigma} g\left(\bar{\sigma}, T, \bar{\gamma}^p\right)} \tag{5.70}$$

When the equivalent plastic strain is the only internal variable, n = 1 and

$$\dot{\xi} = g\left(\bar{\sigma}, T, \bar{\gamma}^p\right) \tag{5.71}$$

The conjugate force to $\bar{\gamma}^p$ is a stress like variable related to isotropic strain hardening [93], and is defined as

$$\Xi = \partial_{\bar{\gamma}^p} \psi \tag{5.72}$$

Then equation (5.70) becomes

$$\chi = 1 - \frac{\Xi - T\partial_T \Xi}{\bar{\sigma}} \tag{5.73}$$

This approach for computing χ has been taken by [90, 91], but the predicted values of χ for steels tends to be significantly lower than the experimental predictions of [98]. In what follows, it is assumed that a constant fraction of the inelastic work is converted to heat, and that the remaining plastic work is expended by creating new fracture surfaces.

The strong form (5.62) - (5.69) becomes

$$\rho\ddot{u} = \sigma_{,x} \tag{5.74}$$

$$\rho\hat{c}\dot{T} = \kappa T_{,xx} + \chi\sigma g\left(\bar{\sigma}, T, \bar{\gamma}^p\right) \tag{5.75}$$

$$c = 4l_0 c_{,xx} + \frac{4l_0}{\mathcal{G}_c} c\left(W^+ + P^+\right) \tag{5.76}$$

$$\sigma = C^{elas}\epsilon^e + \left[(1-c)^2 - 1\right] C^{elas}\left\langle\epsilon^e\right\rangle \tag{5.77}$$

$$\dot{\bar{\gamma}}^p = g\left(\bar{\sigma}, T, \bar{\gamma}^p\right) \tag{5.78}$$

$$\tag{5.79}$$

Insulated thermal boundary conditions are chosen and a velocity is applied to each end. The rod is initially at rest, with a temperature of $315K$. The total strain is additively discomposed into elastic, inelastic and thermal parts as

$$\epsilon^{total} = u_{,x} = \epsilon^e + \epsilon^p + \epsilon^t \tag{5.80}$$

where the thermal part of strain is

$$\epsilon^t = \alpha\Delta T \tag{5.81}$$

and the plastic strain is

$$\epsilon^p = \int_0^t g\left(\bar{\sigma}, T, \bar{\gamma}^p\right) dt' \tag{5.82}$$

where t' is a dummy integration parameter and t is time. Thus, the elastic strain can be computed by

$$\epsilon^e = \epsilon^{total} - \epsilon^p - \epsilon^t. \tag{5.83}$$

The free energy terms which contribute to fracture are the elastic free energy

$$W^+ = \frac{1}{2} C^{elas}\left\langle\epsilon^e\right\rangle^2 \tag{5.84}$$

and the inelastic free energy, which is related to the accumulated plastic work

$$P^+ = \int_0^t (1-\chi)\,\sigma g\left(\bar{\sigma}, T, \bar{\gamma}^p\right) dt' \tag{5.85}$$

Four versions of the above model are considered, the first being the model as it is written, which will be called the combined phase field and shear band model (PFSB) and accounts for both shear banding and fracture. In the second version the phase field parameter is fixed at 0, which reduces the PFSB model to previously studied thermal softening shear band models. The abbreviation used for this is SB. The third version considers isothermal conditions (PFIT), implying that $\chi = 0$, which excludes the possibility of thermal softening, leaving fracture due to accumulation of inelastic work as the only source of failure. The fourth and final version considered is the same as the PFIT model, but with the inelastic contribution to fracture P^+ neglected, and so is abbreviated PFITNP. This model is most similar to existing combined phase field models with plasticity [32, 44]. A summary of the models is shown in table 5.1

Table 5.1: Summary of models tested.

Model Name	Taylor Quinney Parameter	Phase Field	Fracture Source Terms
PFSB	$\chi \neq 0$	Governed by Eq. (5.76)	P^+ and W^+
SB	$\chi \neq 0$	Fixed at 0	-
PFIT	$\chi = 0$	Governed by Eq. (5.76)	P^+ and W^+
PFITNP	$\chi = 0$	Governed by Eq. (5.76)	W^+ only

The problem studied is a 0.001 m rod with a central imperfection in the yield strength and critical energy release rate $\mathcal{G}_c$ and a velocity applied at each end. A wide range of nominal strain rates are tested, from 10^{-1} to 10^5, with the intent of examining the effect of rate on the mode and strain at failure. The effect of the Taylor Quinney fraction χ on the response is also studied over a range of values.

Table 5.2: Material Properties and Parameters. Johnson - Cook parameters were taken from [17] and are for HY 100 steel.

Property Name	Symbol	Value	Unit
Young's Modulus	E	200E9	Pa
Mass Density	ρ	7860	$\frac{kg}{m^3}$
Specific Heat	$\hat{c}$	473	$\frac{J}{kgK}$
Reference Stress	A	111.4E6	Pa
Hardening Parameter	B	579.1E6	Pa
Rate Sensitivity Parameter	c	0.028	-
Strain Hardening Exponent	N	0.054	-
Reference Temperature	T_0	300	K
Reference Temperature	T_m	1800	K
Thermal Softening Parameter	m	0.8	-
Critical Energy Release Rate	$\mathcal{G}_c$	1.25E-4	$\frac{J}{m^2}$
Process Zone Parameter	l_0	5.0E-5	m

The material parameters are chosen to be representative of HY 100 steel, where the Johnson Cook flow law has been used so that

$$g\left(\bar{\sigma}, T, \bar{\gamma}^p\right) = \exp\left\{\frac{1}{c}\left[\frac{\bar{\sigma}}{\left[A + B\left(\bar{\gamma}^p\right)^N\right]\left[1 - \left(\frac{T - T_0}{T_m - T_0}\right)^m\right]} - 1\right]\right\} \tag{5.86}$$

The phase field length scale parameter, which defines the width of the diffuse crack process zone, was chosen to be 5.0E-5 m. In the elastic setting, this parameter effects the peak stress obtained by the material before softening. In the one dimensional, quasi static case, homogeneous solutions of the elastic phase field model predict the critical stress as [31]

$$\sigma_c = \frac{9}{16}\sqrt{\frac{E\mathcal{G}_c}{6l_0}} \tag{5.87}$$

It is apparent that the critical stress tends to infinity as l_0 tends to zero. Physically, this corresponds to the well known crack tip singularity present in linear elastic fracture mechanics with discrete crack topology. In real materials however, experiments show finite fracture process regions. Process zone modeling dates back to the well

known Barenblatt-Dugdale model which introduces the concept of a bounded stress within the cohesive zone at the crack tip [11, 53].

In this study, l_0 simply serves as a regularization parameter. It's value does not determine the stress at which fracture occurs, because the stress in the specimen is limited by the yield stress. However, smaller values of l_0 lead to higher fracture strains. Determination of a physically motivated choice of l_0 is an ongoing area of research for the present authors.

5.2.1 Failure and post localization behavior

Given sufficient input strain, the combined phase field and shear band model will eventually lead to fracture. However, since stress collapse due to thermal softening is an instability in its own right, failure is divided into three categories based qualitatively on the extent of thermal softening before fracture. The failure categories and in Table 5.3.

Failure Mechanism with $\chi = 0.9$	Strain Rates $[1/s]$
Fracture without thermally induced stress collapse	1.0E-1 $-$ 1.0E+2
Thermally induced stress collapse with early transition to fracture	1.0E+2 $-$ 1.0E+4
Thermally induced stress collapse with late transition to fracture	1.0E+4 $-$ 1.0E+5

Table 5.3: Failure mechanisms and corresponding strain rate loading ranges.

Fracture without thermally induced stress collapse tends to occur at the low range of the strain rates modeled here, which lie in the diffusion stabilized zone of the shear band model. At these strain rates thermal diffusion has enough time to spread the heat generated by inelastic deformation throughout the domain, resulting in nearly homogeneous conditions within the rod. However, despite the fact that the heat production is not sufficient to produce failure, the continued inelastic straining leads to fracture. In this range of strain rates, the shear band only model is essentially stable, and large strains are needed to produce significant softening. This is evident

from Figure 5.2a, where the stress strain curves from the four formulations, PFSB, SB, PFIT, and PFITNP are plotted side by side with the phase field parameter vs strain and the temperature vs strain. The temperature rise up to fracture is about 150 degrees, which does not lead to significant thermal softening. The PFSB and SB models perform nearly identically up until the point of fracture, with a slightly slower rate of temperature rise for the PFSB model. This is because the increase of the phase field parameter degrades the stress, which in turn results in less inelastic straining and thus less heat production. Note that inelastic straining and heat production cannot continue in the fully fractured phase since by definition the equivalent plastic strain rate is zero for an unstressed material, i.e. $g\left(\bar{\sigma}=0, T, \bar{\gamma}^{p}\right)=0$. The PFITNP model is similar to the other models only at small strains, and continues to harden without failure. This is due to the fact that the only source term for fracture in the PFITNP model is the elastic free energy, the growth of which is limited by yielding. The implications of this are discussed further in the next section. The PFIT model fails at the earliest strain, since all of the inelastic work contributes to fracture, as opposed to the PFSB model, where a tenth of the inelastic work is generates fracture and the remainder is converted to heat.

Failure due to thermally induced stress collapse with early transition to fracture tend to occur in the transition zone between the diffusion stabilized zone and the critical shear band zone, and is probably where the differences between the PFSB and SB formulations are most important for failure modeling. In these intermediate rates, thermal softening induced stress collapse occurs at roughly the nominal strain for both the SB and the PFSB formulations, but the post localization behavior of the two models is very different.

For the SB model, after an initial rapid stress collapse the rate of softening decreases significantly and a great deal of additional input strain is needed to continue to soften the material, see Figure 5.2b. In contrast for the PFSB model, the stress

collapse causes the stress to drop to zero without a decrease in the softening rate. This is because the phase field parameter has grown to a significant value, roughly 0.6, during the plateau region of the stress strain curve, and the subsequent intense inelastic straining resulting from thermal softening stress collapse causes the material to quickly transition to fracture. The differences in the post localization behavior of the two models is of particular importance in higher dimensions, where the propagation characteristics of the shear band depend on the unloading rate. Again, the PFIT model, which is most appropriate for small strain rates, fails at very low strains. The PFITNP model is not shown since no failure is predicted by this model.

Thermally induced stress collapse with late transition to fracture occurs in the critical shear band zone, and there are only minor differences between the two models in this range until late in the stress collapse process. Due to slower heat production, the PFSB model shows slightly higher strain to failure than the SB model, see Figure 5.2c. The post localization behavior of the two models is also similar, since thermal softening is prevalent at these rates and thus fracture will not occur until late in the stress collapse process. Further details on the effect of the strain rate and Taylor Quinney fraction on the failure characteristics are given in section 5.2.3.

5.2.2 Inelastic contribution to fracture

A comparison of the elastic and inelastic contributions to fracture vs nominal strain for the PFSB model are shown in Figure 5.3, with the same strain rates as were shown in the previous section. These are the inelastic free energy, the elastic free energy, and the sum of the two, defined as

$$\text{inelastic energy} \qquad \psi^i = (1-c)^2 P^+ \tag{5.88}$$

$$\text{elastic energy} \qquad \psi^e = (1-c)^2 W^+ \tag{5.89}$$

$$\text{total energy} \qquad \psi^{tot} = \psi^i + \psi^e = (1-c)^2 \left[P^+ + W^+\right] \tag{5.90}$$

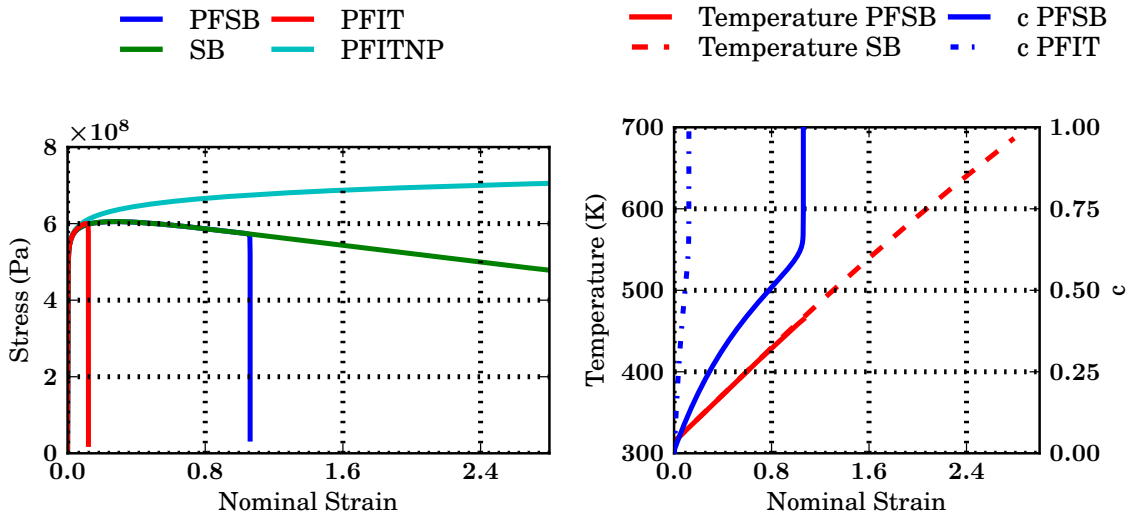

(a) $\chi = 0.9$, $\dot{\epsilon_0} = 1.0$

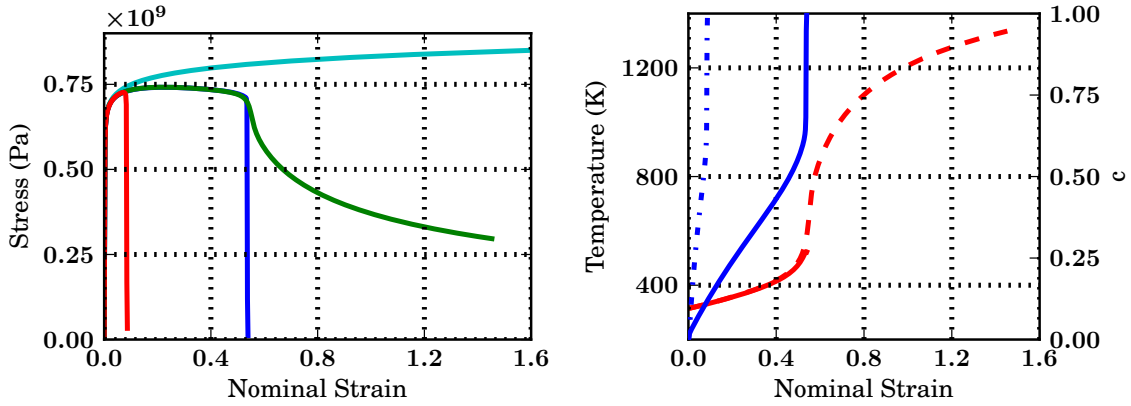

(b) $\chi = 0.9$, $\dot{\epsilon_0} = 5.0E + 3$

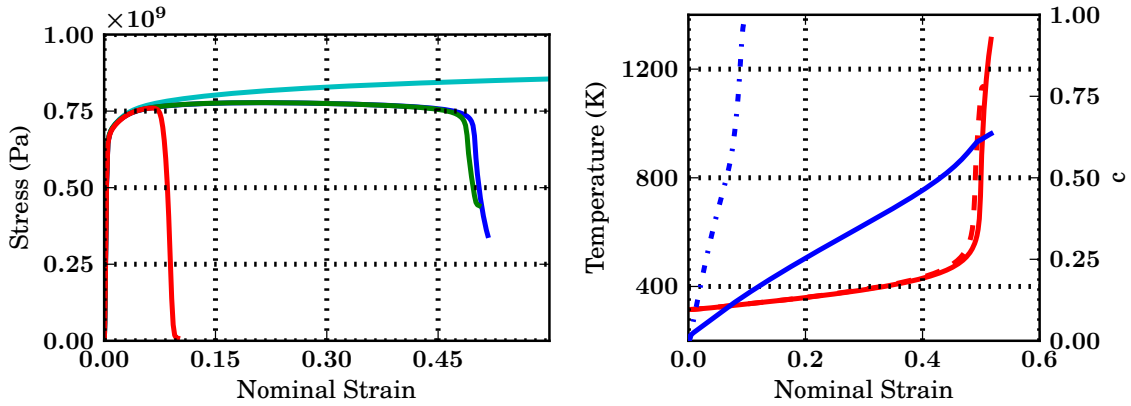

(c) $\chi = 0.9$, $\dot{\epsilon_0} = 5.0E + 4$

Figure 5.2: Plots illustrating the three failure categories. Stress vs nominal strain is shown in the left column. In the right column the phase field parameter and temperature vs nominal strain is shown. The left axis is for the temperature, which is plotted in red, and the right axis is for the phase field parameter c, which is plotted in blue.

Up until the point of fracture, the contribution of the inelastic free energy is much higher than the elastic contribution, due to the fact that the elastic strain is small compared to the inelastic strain. After fracture, inelastic straining ceases and the inelastic free energy drops to zero due to the degradation function $(1-c)^2$, while the elastic strain increases rapidly. The increase in the elastic strain is because the strain increments in the fully fractured phase are modeled as pure elastic, even though they physically represent a separated material.

In the one dimensional setting, it is clear that the growth of the elastic free energy will be quadratic in the elastic range, but the onset of yielding will limit further growth of this term. In fact, with thermally induced softening, the elastic free energy can decrease as the material unloads. Thus, unless fracture occurs before yielding, crack formation will not be possible in the one dimensional setting unless the contribution of inelastic deformation to fracture is accounted for as in the present formulation. This is evident from figure 5.4, where the free energies are shown vs strain for the PFSB, PFIT, and PFITNP models.

Here it is shown that when the inelastic free energy is not accounted as a source term in the phase field equation, the elastic free energy does not increase beyond the peak stress, thus prohibiting the occurrence of a crack, as shown by the light blue curve in Figure 5.4. In contrast, when the inelastic free energy is accounted for, the phase field source term will continue to increase, even during thermal softening. Additionally, continued growth of the phase field parameter degrades the stress as previously mentioned, which leads to smaller increments of inelastic strain, which means a larger portion of the total strain increment will be elastic. This is why the elastic free energy is larger and why it continues to grow after yielding when the inelastic contribution to fracture is accounted for, as shown in figure 5.3.

In multi dimensional simulations of elastic plastic materials, it is possible for cracks to occur without consideration of P^+ if the loading is sufficiently triaxial. However

for shear bands, extensive inelastic deformation occurs in an essentially isochoric manner, and exclusion of this term ignores the contribution of this deformation to fracture. Exclusion of P^+ or a similar term as presented in the previous section would model fracture as independent of the state of the material's microstructure. This is in contrast to the fact that microstructural characteristics which impede dislocation motion such as dislocation density and grain size are related to fracture.

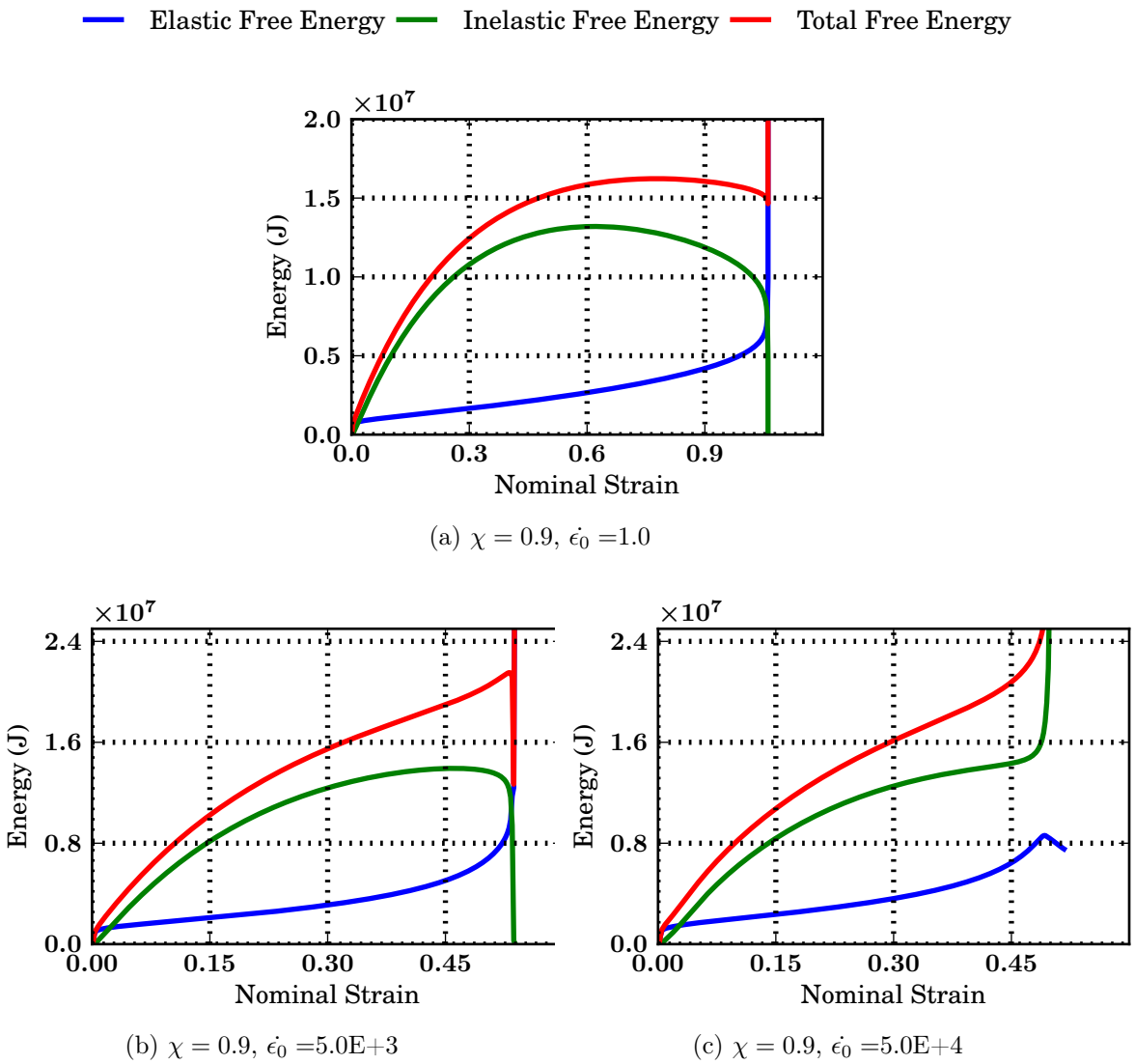

(a) $\chi = 0.9$, $\dot{\epsilon_0}$ =1.0

(b) $\chi = 0.9$, $\dot{\epsilon_0}$ =5.0E+3

(c) $\chi = 0.9$, $\dot{\epsilon_0}$ =5.0E+4

Figure 5.3: For the PFSB model the elastic, inelastic, and total free energies, which serve as the driving forces for fracture, are shown vs nominal strain.

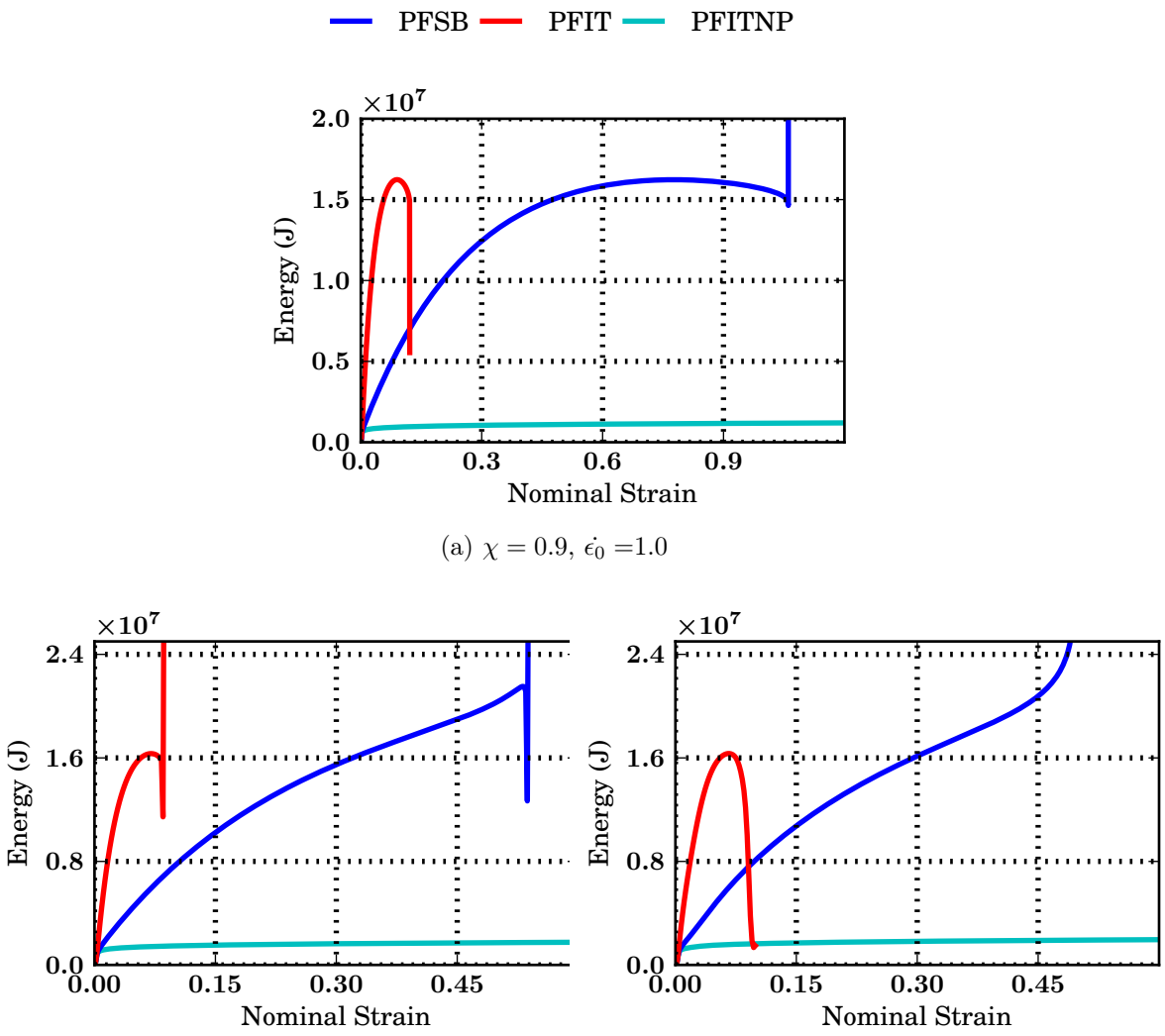

(a) $\chi = 0.9$, $\dot{\epsilon_0}$ =1.0

(b) $\chi = 0.9$, $\dot{\epsilon_0}$ =5.0E+3

(c) $\chi = 0.9$, $\dot{\epsilon_0}$ =5.0E+4

Figure 5.4: The total free energy for the PFSB, PFIT, and PFITNP models is shown vs nominal strain. For the PFITNP model, the only fracture producing contribution to the free energy is the elastic energy, shown in light blue, which does not increase significantly beyond the yield point.

5.2.3 Effect of strain rate and Taylor Quinney fraction on failure strain

The combined phase field and shear band model has been tested for Taylor Quinney fractions of 0.5, 0.7, and 0.9, with strain rates varying from 10^{-1} to 10^{5}. Here, we define failure as a drop in the integral averaged stress to 0.9 of the peak value in its

history

$$\int_{\Omega} \sigma(x,t) d\Omega = 0.9 \max \left[\int_{\Omega} \sigma(x,t) d\Omega \right] \tag{5.91}$$

and as a second condition, there must be severe strain localization at the center of the rod. The range of strain rates was chosen to illustrate the zones in Figure, which are the diffusion stabilized zone, the critical shear band zone, and the two transition zones above and below the critical shear band zone, as illustrated in Figure 1. In the transition zone above the critical shear band zone inertia effects are significant and the conditions in the domain are highly non uniform due to elastic wave propagation. For the current test problem, strain rates beyond 1.0E+5 $1/s$ lead to significant thermal softening at the ends of the rod, which can occur while the center of the rod has not yet been loaded. Since the aim of studying the one dimensional test problem is to compare the four formulations in the simplest possible setting, we leave these higher rates to future studies.

The failure strain vs strain rate is shown in figure 5.5. For the shear band only model, the diffusion stabilized, first transition, and critical shear band zones can be clearly identified. The second transition zone can not be clearly shown due to the effect described in the previous paragraph. For a Taylor Quinney parameter of 0.9, which is the value used typically in the literature, differences in the failure strain in the diffusion stabilized zone are due to fracture occurring without much thermal softening. In the first transition zone, some differences in failure strain are present, but the response of the PFSB and SB formulations mainly differs beyond the failure point recorded for this plot. Lastly, the PFSB and SB formulations are most similar in the critical shear band zone, where there are only slight differences in the failure strains of the two models. It is worth noting that since the inelastic source term in the phase field equation is strain, strain rate, and temperature dependent, the fracture response is also dependent on these quantities as well.

For the isothermal PFIT model , increased strain rate is found to always decrease the strain to failure with χ held fixed. In the context of the model, this is due to the rate dependence of the Johnson Cook model, where higher strain rates lead to higher yield stresses, which causes the plastic work term in equation (5.85) to accumulate faster. The presence of thermal softening in the PFSB model leads to larger failure strains compared to the PFIT model, and in addition there is a minimum strain to failure in the critical shear band zone for the PFSB model.

While a fully variable fraction is not modeled, a parametric study of constant Taylor Quinney fraction has been conducted, and this parameter was found to have a significant effect on the results. A lower Taylor Quinney fraction not only leads to a higher fraction of the inelastic work available as a source term in the phase field equation, but less heat will be generated, resulting in a lower susceptibility to thermal softening induced stress collapse. In the results shown in Figure 5.5, lowering the fraction significantly biases the results toward fracture.

Experimental work on carbon steels by [51] show a transition from essentially isothermal conditions to essentially adiabatic conditions over the course of three decades of strain rate. This was used by [137], to develop an expression for χ as a function of strain rate as a smooth step function. We use a similar expression here, namely

$$\chi = 0.45 + 0.45 \tanh\left(0.6 \log\left(\frac{\dot{\epsilon}_0}{50}\right)\right) \tag{5.92}$$

Which is the same as the function used by [137], but the limiting values of χ used here are 0.0 and 0.9, instead of 0 and 1. The transition region from $\chi = 0.0$ to $\chi = 0.9$ is thus 1.0 1/s - 1.0E+3 1/s. The results of this are shown in Figure 5.5d, which demonstrates that the PFSB and PFIT models are identical at low strain rates, where the effects of temperature are very small. For the same reason, there is no failure predicted by the SB model. As the strain rate is increased, the strain to failure predicted by PFSB and PFIT begins to increase, due to the fact that the

fraction of inelastic work that generates fracture decreases. This trend is in qualitative agreement with experiments on HY 100 steel by [119], where the failure strains at intermediate strain rates were found to be larger than failure strain of quasi static tests. In this region, the failure strain of the PFSB model is higher than the PFIT model, indicating that temperature rise is improving the ductility of the material. The PFSB and SB model meet in the critical shear band zone, where thermal softening is most prevalent. Thus the PFSB model coincides with the PFIT model at low strain rates where the thermal softening is negligible, and with the SB model in the critical shear band zone, where thermal softening induced stress collapse occurs most readily. In the transition region, which is of the most interest, failure strains for the PFSB model are higher than the PFIT model, but significantly lower than the SB model.

5.3 Conclusion

A formulation for simultaneously modeling shear bands and fracture was developed using conservation laws and thermodynamic principles. The formulation combines a thermally softening shear band model with the phase field method for fracture. The phase field method presented here differs from existing ones in that it includes a term accounting for the creation of fracture surfaces stored energy of cold work, which is energy stored by imperfections in the crystal lattice of a metal upon inelastic straining. Thus, the inelastic work is partitioned into heat, which contributes to thermal softening, and stored energy of cold work, which contributes to fracture.

A simple, one dimensional parametric study was conducted with constant partition of cold work to illustrate the basic behavior of the model and compare the model with two special cases. The original model, abbreviated as PFSB to indicate that thermal softening and fracture are present, was compared to the isothermal case (PFIT) which models ductile fracture without temperature rise, and the damage free

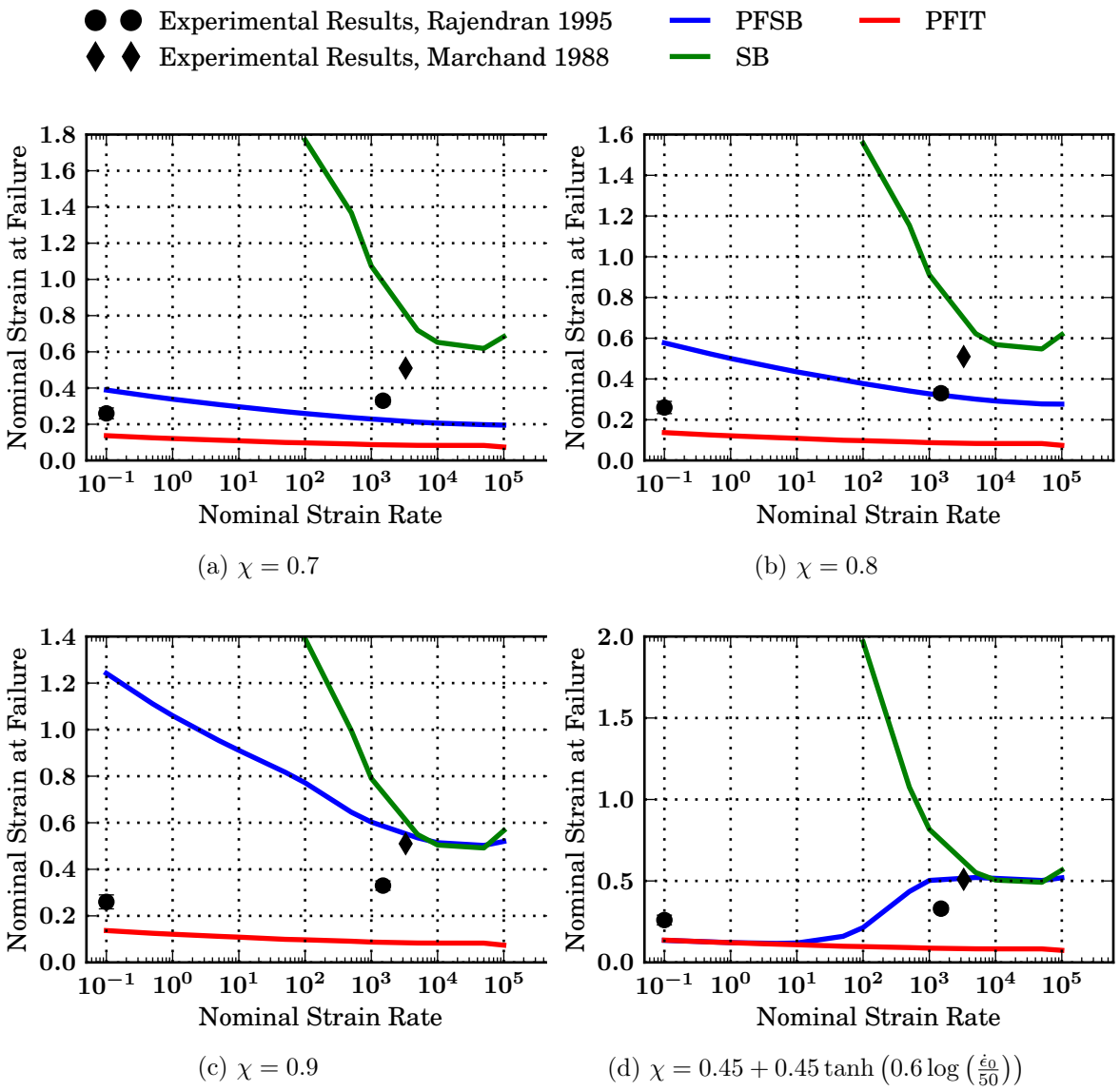

(a) $\chi = 0.7$

(b) $\chi = 0.8$

(c) $\chi = 0.9$

(d) $\chi = 0.45 + 0.45 \tanh\left(0.6 \log\left(\frac{\dot{\epsilon}_0}{50}\right)\right)$

Figure 5.5: Failure strain vs strain rate for different values of χ. The black dots are from experimental tension tests on HY 100 steel from [119], which consisted of a quasi static test and a split Hopkinson test at 1500 1/s. The black diamond is the failure strain from a Hopkinson bar torsion test at 3300 1/3.

case (SB), which reduces the model to thermal softening shear banding models found in the literature. The final model tested was isothermal with damage, but without the inelastic contribution to fracture introduced in section 5.1 of this chapter. This model was abbreviated at PFITNP and was found to never lead to failure since the only source of damage is the elastic free energy, the growth of which is limited by yielding. Material parameters were chosen for a typical steel and strain rates of 10^{-1}

to 10^5 were tested. Using a Taylor Quinney fraction of 0.9, it was found that in the diffusion stabilized zone, where shear banding does not occur, fracture occurs in the PFSB model without much thermal softening. In the first transition zone, there are also very significant differences between the PFSB and the SB models, principally in the post stress collapse behavior, where the unloading rate of the present model is much faster than the shear band only model.

For all strain rates, the PFSB model predicts higher failure strains then the PFIT model, indicating that temperature rise improves the ductility of the material. Using a strain rate dependent Taylor Quinney fraction which ramps smoothly from a value of 0.0 to 0.9 over the strain rates 1.0 1/s to 1.0E+3 1/s, the PFSB model coincides with the PFIT model at low strain rates, where thermal softening is negligible, and with the SB model in the critical shear band zone, where thermal softening is most prevalent. This formulation is very important for accurate failure modeling in higher dimensions, where the unloading rate effects the propagation characteristics of the shear band. In the critical shear band zone, where thermal softening is prevalent, the models behaved quite similarly. Thus, it is expected that the present model will be valid for failure modeling in a much broader range of strain rates than the shear band only model, as well as significantly improve the accuracy of failure modeling in the transition regions. Furthermore, the framework presented here permits modeling of the relationship between fracture and barriers to dislocation motion such as dislocation density and grain size. This leads to a model for fracture which is explicitly rate and temperature dependent, due to the rate and temperature dependence of the internal variables.

Future studies will include determination of the most physically reasonable values for the phase field length scale parameter, l_0, which at present is interpreted as a regularization parameter. In addition, multidimensional studies will be conducted,

where the triaxiality of the load will contribute to the tendency of the material to fracture or shear band, in addition to the effects modeled here.

Chapter 6

Conclusion

This dissertation has presented a number of contributions to numerical modeling of high rate failure in metals. Chapter 2 demonstrated that a monolithic nonlinear solver in conjunction with thermal diffusion lead to results which were insensitive to mesh size and which had a reduced sensitivity to mesh alignment in comparison with a split nonlinear solver. This formulation was then applied to the analysis of friction stir welded aluminum joints under high rate loading in chapter 3, where it was found that the abrupt changes in material properties which arise from the distinct microstructural zones produced by the stir welding process significantly reduce the energy absorption capacity of the joint. This analysis suggests that weld capacity can be improved through various process modifications leading to less abrupt property changes. Chapter 4 developed a Pian Sumihara type element for shear bands which was shown to furnish greater accuracy for less computational resources than standard irreducible interpolations. This element was also shown to be less sensitive to the stiffening effect observed in mildly distorted meshes. Chapter 5 introduced a combined model for shear banding and fracture, the behavior of which was studied in a simple one dimensional setting. This model is important for realistic dynamic failure simulation of metals where cracks and shear bands are both typically present

There are numerous future directions for this work, both in terms of enhanced physical modeling as well as improved numerical procedures. Numerical improvements include analysis of efficient and scalable composable linear solvers for the shear band and combined shear band and fracture models. As shown in chapter 2, split solvers are not suitable nonlinear solvers for the shear band problem, but this does not exclude the possibility of the use of a split method as a preconditioner for the linear solve phase of the monolithic scheme. Thus the block structure of the Jacobian matrix, which are dependent upon the type of shape functions used, can be exploited, and special solvers which may exist for sub problems of the multiphysics shear band problem can be leveraged. An example of this would be using multigrid in the preconditioning scheme for the thermal part of the shear band problem. The notion of composable linear solvers and the implementation of them in PETSc is described in [37].

A second future area of numerical research is the use of isogeometric analysis with the formulations presented here. Appendix A gives a brief account of preliminary results for this, where it is shown that NURBS elements outperform the Pian-Sumihara element on the plate in tension test problem used in chapter 2. In addition, T-splines have been successfully used for phase field fracture analysis by [31], suggesting that isogeometric analysis will also be successful for the combined phase field and shear band model of chapter 5. Isogeometric analysis may also help suppress the mesh alignment sensitivity that was only partially cured by the monolithic solver in chapter 2.

Enhancements to physical modeling will include crystal plasticity based calculation of the evolution of internal plastic variables described in 5. From a theoretical standpoint, this appears to be the most promising method for accurate calculation of the partition of inelastic work into heat, and appears to posses the most favorable agreement with experiment [40]. As pointed out in chapter 5, the tendency of a ma-

terial to fail by fracture or shear banding is very sensitive to this partition, and thus the partition must be accurately calculated.

Bibliography

[1] E C Aifantis. On the Microstructural Origin of Certain Microstructural Models. Journal of Engineering Materials Technology, 106:326, 1984.

[2] E C Aifantis. The Physics of Plastic Deformation. International Journal of Plasticity, 3:211–247, 1987.

[3] Rashid K Abu Al-Rub and George Z Voyiadjis. A Finite Strain Plastic-damage Model for High Velocity using Combined Viscosity and Gradient Localization Limiters: Part I - Theoretical Formulation. International Journal of Damage Mechanics, 15:293–334, 2006.

[4] Rashid K Abu Al-Rub and George Z Voyiadjis. A Physically Based Gradient Plasticity Theory. International Journal of Plasticity, 22:654–684, 2006.

[5] Hanen Amor, Jean-jacques Marigo, and Corrado Maurini. Journal of the Mechanics and Physics of Solids Regularized formulation of the variational brittle fracture with unilateral contact : Numerical experiments. Journal of the Mechanics and Physics of Solids, 57(8):1209–1229, 2009.

[6] N. Aravas, K-S. Kim, and F. A. Leckie. On the Calculations of the Stored Energy of Cold Work. 112:465–470, 1990.

[7] I Babuska. Error Bounds for Finite Element Method. Numerische Mathematik, 16:322–333, 1971.

[8] M. E. Backman and S. A. Finnegan. The Propagation of Adiabatic Shear. In R. W. Rohde, B. M. Butcher, J. R. Holland, and C. H. Karnes, editors, Metallurgical Effect at High Strain Rates, pages 531–543, New York, 1973. Plenum Press.

[9] Y.L. Bai. Thermo-plastic instability in simple shear. Journal of the Mechanics and Physics of Solids, 30(4):195–207, August 1982.

[10] Satish Balay, Jed Brown, Kris Buschelman, Victor Eijkhout, William D Gropp, Dinesh Kaushik, Matthew G Knepley, Lois Curfman McInnes, Barry F Smith, and Hong Zhang. PETSc Users Manual. Technical report, Argonne National Laboratory, 2007.

[11] G. I. Barenblatt. The mathematical theory of equilibrium cracks in brittle fracture. Advances in Applied Mechanics, 7:55–129, 1962.

[12] R H Bartels, J C Beatty, and B A Barsky. An introduction to splines for use in computer graphics and geometric modeling. Morgan Kaufmann, 1987.

[13] R C Batra. The initiation and growth of, and the interaction among, adiabatic shear bands in simple and dipolar materials. International journal of plasticity, 3:75–89, 1987.

[14] R C Batra, N A Jaber, and M E Malsbury. Analysis of failure modes in an impact loaded thermoviscoplastic prenotched plate. International Journal of Plasticity, 19:139–196, 2003.

[15] R C Batra and B M Love. Multiscale analysis of adiabatic shear bands in tungsten heavy alloy particulate composites. Internatonal Journal for Multiscale Computational Engineering, 4(95-114), 2006.

[16] RC Batra and XS S Jin. Analysis of dynamic shear bands in porous thermally softening viscoplastic materials. Archives of Mechanics, 46:13–36, 1994.

[17] R.C. Batra and C.H. Kim. Effect of thermal conductivity on the initiation, growth and bandwidth of adiabatic shear bands. International Journal of Engineering Science, 29(8):949–960, January 1991.

[18] R.C. Batra and B.M. Love. Consideration of microstructural effects in the analysis of adiabatic shear bands in a tungsten heavy alloy. International Journal of Plasticity, 22(10):1858–1878, October 2006.

[19] RC Batra and MVS Ravinsankar. Three-dimensional numerical simulation of the Kalthoff experiment. International Journal of fracture, (105):161–186, 2000.

[20] R.C. Batra and G.M. Zhang. Analysis of adiabatic shear bands in elasto-thermo-viscoplastic materials by modified smoothed-particle hydrodynamics (MSPH) method. Journal of Computational Physics, 201(1):172–190, November 2004.

[21] Th. H Baxevanis, Th. Katsaounis, a. E. Tzavaras, and T H Kataounis. Adaptive Finite Element Computations of Shear Band Formation. Mathematical Models and Methods in Applied Sciences, 20(03):423–448, March 2010.

[22] A Bayliss, T Belytschko, M Kulkarni, and D A Lott-Crumpler. On the dynamics and the role of imperfections for localization in thermo-viscoplastic materials. Modelling and Simulation in Materials Science and Engineering, 2(5):941, 1994.

[23] Zdenek P Bazant and Ted B Belytschko. Wave Propagation in a Strain-Softening Bar: Exact Solution. Journal of Engineering Mechanics, 111(3):381–389, 1985.

[24] Zdenek P Bazant and Milan Jirasek. Nonlocal Integral Formulations of Plasticity and Damage: Survey of Progress. Journal of Engineering Mechanics, 128(11):1119–1149, 2002.

[25] Y Bazilevs, L Beirao da Veiga, J A Cottrell, T J R Hughes, and G Sangalli. Isogeometric analysis: approximation, stability and error estimates for h-refined meshes. Mathematical Models and Methods in Applied Sciences, 16(07):1031–1090, 2006.

[26] T Belytschko, HY Chiang, and E Plaskacz. High resolution two-dimensional shear band computations: imperfections and mesh dependence. Computer Methods in Applied Mechanics and Engineering, 119:1–15, 1994.

[27] A. Benzerga, Y. Bréchet, A. Needleman, E. Van der Giessen, and a.a. Benzerga. The stored energy of cold work: Predictions from discrete dislocation plasticity. Acta Materialia, 53:4765–4779, October 2005.

[28] M. B. Bever, D. L. Holt, and A. L. Titchener. The stored energy of cold work. Progress in Materials Science, 17:1–190, 1973.

[29] J Bonet and R C Wood. Nonlinear Continuum Mechanics for Finite Element Analysis. Cambridge University Press, 1997.

[30] A S Bonnet-Lebouvier, A Molinari, and P Lipinski. Analysis pf dynamic propagation of adiabatic shear bands. International Journal of Solids and Structures, 39:4249–4269, 2002.

[31] Michael J Borden, Clemens V Verhoosel, Michael A Scott, Thomas J R Hughes, and Chad M Landis. A phase-field description of dynamic brittle fracture. Computer Methods in Applied Mechanics and Engineering, 217-220:77–95, 2012.

[32] Michael Johns Borden. Isogeometric Analysis of Phase Field Models for Dynamic Brittle Fracture. PhD thesis, Univeristy of Texas at Austin, 2012.

[33] B Bourdin, G A Francfort, and J-J Marigo. Numerical experiments in revisited brittle fracture. Journal of the Mechanics and Physics of Solids, 48(4):797–826, 2000.

[34] Blaise Bourdin, Gilles A Francfort, and Jean-jacques Marigo. The Variational Approach to Fracture. Journal of Elasticity, 91:5–148, 2008.

[35] Blaise Bourdin, Christopher J Larsen, and Casey L Richardson. A time-discrete model for dynamic fracture based on crack regularization. International Journal of fracture, 168:133–143, 2011.

[36] F Brezzi. On the existence, uniqueness and approximation of saddle-point problems arising from Lagrangian multipliers. Rev. Française Automat. Informat. Recherche Opérationnelle Sér. Rouge, 8:129–151, 1974.

[37] Jed Brown, Matthew G. Knepley, David a. May, Lois Curfman McInnes, and Barry Smith. Composable Linear Solvers for Multiphysics. 2012 11th International Symposium on Parallel and Distributed Computing, pages 55–62, June 2012.

[38] Nilsson C. On nonlocal rate-independent plasticity. International Journal of Plasticity, 14:551–575, 1998.

[39] Guanrong Chen. Stability of Nonlinear Systems, pages 4881–4896. John Wiley & Sons, Inc., 2005.

[40] J. D. Clayton. Dynamic Plasticity and Fracture in High Density Polycrystals : Constitutive Modeling and Numerical Simulation. Journal of the Mechanics and Physics of Solids, 53:261–301, 2005.

[41] R W Clough and J Penzien. Dynamics of structures. Dynamics of Structures Ray W. Clough, Joseph Penzien. McGraw-Hill, 1975.

[42] C Comi and U Perego. A unified approach for variationally consistent finite elements in elastoplasticity. Computer Methods in Applied Mechanics and Engineering, 121:323–344, 1995.

[43] J A Cottrell, T J R Hughes, and Y Bazilevs. Isogeometric Analysis: toward integration of CAD and FEA. Wiley, 2009.

[44] Tamer Crosby and Nasr Ghoniem. Phase-field modeling of thermomechanical damage in tungsten under severe plasma transients. Computational Mechanics, 50(2):159–168, June 2012.

[45] T A Davis and I S Duff. An unsymmetric-pattern multifrontal method for sparse LU factorization. SIAM Journal on Matrix Analysis and Applications, 18:140–158, 1997.

[46] C J Dawes and W M Thomas. Friction stir process welds alluminum alloys. Welding Journal, 75:41–52, 1996.

[47] C de Boor. A Practical Guide to Splines. Number v. 27 in Applied Mathematical Sciences. Springer, 2001.

[48] J A DiLellio and W E Olmstead. Shearband Formation due to a Thermal Flux Inhomogeneity. SIAM Journal of Applied Mathematics, 57:959–971, 1997.

[49] J A DiLellio and W E Olmstead. Temporal Evolution of Shearband Thickness. Journal of the Mechanics and Physics of Solids, 45:345–359, 1997.

[50] J A DiLellio and W E Olmstead. Numerical Solutions of Shear Localization in a Finite Slab. Mechanics of Materials, 29:71–80, 1998.

[51] P R Dixon and D J Parry. Thermal softening effects in type 224 carbon steel. Journal de Physique IV, 1, 1991.

[52] R. Dormeval. The adiabatic shear phenomenon. In T. Z. Blazynski, editor, Materials at High Strain Rates, pages 47–70, London, 1987. Elsevier.

[53] D. S. Dugdale. Yielding of steel sheets containing slits. Journal of the Mechanics and Physics of Solids, 8(2):100–104, 1960.

[54] G E Farin. NURBS Curves and Surfaces: from Projective Geometry to Practical Use. A.K. Peters Ltd., 1995.

[55] W. S. Farren and G. I. Taylor. The heat developed during plastic extension of metals. Proceedings of the Royal Society of London A, 107:422–451, 1925.

[56] G A Francfort and J J Marigo. Revisiting brittle fracture as an energy minimization problem. Journal of the Mechanics and Physics of Solids, 46(8):1319–1342, 1998.

[57] C Fressengeas. Adiabatic shear morphology at very high strain rates. International Journal of Impact Engineering, 8(2):141–157, 1989.

[58] C Fressengeas and A Molinari. Instability and localization of plastic in shear at high strain rates. Journal of the Mechanics and Physics of Solids, 35(2):185–211, 1987.

[59] Christophe Geuzaine and Jean-Francois Remacle. Gmsh Reference Manual. http://www.geuz.org/gmsh, 1.12 edition, August 2003.

[60] D. E. Grady and M. E. Kipp. The growth of unstable thermoplastic shear with application to steady-wave shock compression in solids. Journal of the Mechanics and Physics of Solids, 35(1):95–118, 1987.

[61] A A Griffith. The Phenomena of Rupture and Flow in Solids. Philosophical Transactions of the Royal Society A Mathematical Physical and Engineering Sciences, 221(582-593):163–198, 1921.

[62] M Grujicic, G Arakere, P Pandurangan, C F Yen, B A Cheeseman, A P Reynolds, and M A Sutton. Computational analysis of material flow during friction stir welding of AA5059 aluminum alloys. Journal Materials Engineering and Performance, 21:1824–1840, 2012.

[63] M Grujicic, T He, G Arakere, H V Yalavarthy, C F Yen, and B A Cheeseman. Fully coupled thermomechanical finite element analysis of material evolution during friction stir welding of AA5083. Journal of Engineering Manufacture, 224:609–625, 2009.

[64] M Grujicic, P Pandurangan, C F Yen, and B A Cheeseman. Modifications in the AA5083 Johnson-Cook material model for use in friction stir welding computational analyses. Journal Materials Engineering and Performance, 21:2207–2217, 2012.

[65] S Guiliani. An algorithm for continuous rezoning of the hydrodynamic grid in arbitrary Lagrangian-Eulerian codes. Nuclear Engineering and Design, 72:205–212, 1982.

[66] M A Gutierrez, R de Borst, J C J Schellekens, and L J Sluys. An algorithm for mesh rezoning with application to strain localization problems. Computers and Structures, 55:237–247, 1995.

[67] A Henderson. ParaView Guide, A Parallel Visualization Application, Kitware Inc., 3.10 edition, 2007.

[68] J. Hodowany, G. Ravichandran, a. J. Rosakis, and P. Rosakis. Partition of plastic work into heat and stored energy in metals. Experimental Mechanics, 40(2):113–123, June 2000.

[69] J. Hodowany, G. Ravichandran, A.J. Rosakis, and P. Rosakis. A thermodynamic internal variable model for the partition of plastic work into heat and stored energy in metals. Journal of the Mechanics and Physics of Solids, 48(3):581–607, June 2000.

[70] V E Howle and Lloyd N Trefethen. Eigenvalues and musical instruments. Journal of Computational and Applied Mathematics, 135(1):23–40, 2001.

[71] T J R Hughes. Generalization of selective integration procedures to anisotropic and nonlinear materials. International Journal of Numerical Methods in Engineering, 15:1413–1418, 1980.

[72] T J R Hughes. The Finite Element Method: Linear Static and Dynamic Finite Element Analysis. Prentice-Hall, 1987.

[73] T J R Hughes, J A Cottrell, and Y Bazilevs. Isogeometric analysis: CAD, finite elements, NURBS, exact geometry and mesh refinement. Computer Methods in Applied Mechanics and Engineering, 194(39-41):4135–4195, 2005.

[74] John D Hunter. Matplotlib: A 2D Graphics Environment. Computing in Science and Engineering, 9(3):90–95, 2007.

[75] C. J. Irwin. Metallographic Interpretation of Impacted Ogive Penetrators. Technical report, DREV, Canada, 1972.

[76] J W Ju. Energy-based coupled elastoplastic damage models at finite strains. International Journal of Solids and Structures, 115(11):803–833, 1989.

[77] J W Ju. On energy-based coupled elasto-plastic-damage theories:Constitutive modeling and computational aspects. International Journal of Solids and Structures, 25:803–833, 1989.

[78] Brian Justusson. Microstructural Investigation and Evaluation of Mechanical Properties in Friction Stir Welded Joints. Technical report, U. S. Army Research Labortory WMRD RDRL-WMM-B, Aberdeen Proving Ground, MD, 21005, 2011.

[79] Brian Justusson, Jessica Medintz, Jian Yu, Constantine Fountzoulas, and Chian Fong Yen. Spatial Mechanical Response and Strain Gradient Evolution of Friction Stir Welded Aluminum-2139. Technical Report February, U.S. Army Research Laboratory RDRL-WMM-B, Aberdeen Proving Ground, MD 21005, 2012.

[80] J. F. Kalthoff and S. Winkler. Failure mode transition at high rates of shear loading. In C. Chiem, H. D. Kunze, and L. W. Meyer, editors, Impact Loading and Dynamic Behavior of Materials, vol. 1, pages 185–195. DGM Informationsgesellschaft Verlag, 1987.

[81] Joerg F Kalthoff. Modes of dynamic shear failure in solids. International Journal of fracture, 101:1–31, 2000.

[82] D A Knoll, L Chacon, L G Margolin, and V A Mousseau. On balanced approximations for time integration of multiple time scale systems. Journal of Computational Physics, 185:583–611, 2003.

[83] E N Lages, G H Paulino, I F M Menezes, and R R Silva. Nonlinear Finite Element Analysis Using an Object Oriented Philosophy - Application to Beam Elements and to the Cosserat Continuum. Engineering with Computers, 15:73–89, 1999.

[84] C W Lan, M K Chen, and M C Liang. Bifurcation and stability analyses of horizontal Bridgman crystal growth of a low Prandtl number material. Journal of Crystal Growth, 187(2):303–313, 1998.

[85] Shaofan Li and Wing Kam Liu. Numerical simulations of strain localization in inelastic solids using meshfree methods. International Journal of Solids and Structures, 37:7185–7206, 2000.

[86] Shaofan Li, Wing Kam Liu, Ares J Rosakis, Ted Belytschko, and Wei Hao. Mesh-free Galerkin simulations of dynamic shear band propagation and failure mode transition. International Journal of Solids and Structures, 39:1213–1240, 2002.

[87] Xue Liang and Ted Belytschko. Fast methods for determining instabilities of elastic-plastic damage models through closed form expressions. International Journal for Numerical Methods in Engineering, 84(12):1490–1518, 2010.

[88] Xianwu Ling and Ted Belytschko. Thermal softening induced plastic instability in rate-dependent materials. Journal of the Mechanics and Physics of Solids, 57:788–802, April 2009.

[89] H Liu, H Fulii, M Maeda, and K Nogi. Tensile properties and fracture locations of friction-stir welded joints of 6061-T6 aluminium Alloy. Journal of Material Science Letters, 22:1061–1063, 2003.

[90] P Longere and A Dragon. Adiabatic heat evaluation for dynamic plastic localization. Theoretical and Applied Mechanics, 45:203–223, 2007.

[91] Patrice Longere and Andre Dragon. Inelastic heat fraction evaluation for engineering problems involving dynamic plastic localization phenomena. Journal of Mechanics of Materials and Structures, 4(2):319–349, 2009.

[92] B Loret and J H Prevost. Dynamic strain localization in elasto-(visco-)plastic solids 1. General formulation and one-dimensional examples. Computer Methods in Applied Mechanics and Engineering, 83:247–273, 1990.

[93] J Lubliner. Plasticity Theory. Macmillan, New York, 1990.

[94] A M Lyapunov. General Problem of the Stability Of Motion. CRC Press, 1 edition, 1992.

[95] D. Macdougall. Determination of the plastic work converted to heat using radiometry. Experimental Mechanics, 40(3):298–306, September 2000.

[96] A Marchand and J Duffy. An Experimental Study of the Formation Process of Adiabatic Shear Bands. Journal of the Mechanics and Physics of Solids, 38:238–251, 1988.

[97] Jerrold Marsden and Thomas J R Hughes. Mathematical Foundations of Elasticity. Prentice-Hall, Englewood Cliffs, 1993.

[98] J J Mason, A J Rosakis, and G Ravichandran. On the strain and strain rate dependence of the faction of plastic work converted to heat: an experimental study using high speed infrared dectoctora and the Kolsky bar. Mechanics of Materials, 17:135–145, 1994.

[99] Colin McAuliffe and Haim Waisman. Mesh insensitive formulation for initiation and growth of shear bands using mixed finite elements. Computational Mechanics, 51(5):807–823, 2012.

[100] Colin McAuliffe and Haim Waisman. A Pian Sumihara type element for modeling shear bands at finite deformation. Computational Mechanics, In press, 2013.

[101] C McVeigh and W K Liu. Multiresolution continuum modeling of micro-void assisted dynamic adiabatic shear band propagation. Journal of the Mechanics and Physics of Solids, 58:187–205, 2010.

[102] Sergey N Medyanik, Wing Kam Liu, and Shaofan Li. On criteria for dynamic adiabatic shear band propagation. Journal of the Mechanics and Physics of Solids, 55:1439–1461, 2007.

[103] C Miehe, F Welschinger, and M Hofacker. Thermodynamically consistent phase-field models of fracture : Variational principles and multi-field FE implementations. International Journal for Numerical Methods in Engineering, 83(March):1273–1311, 2010.

[104] Christian Miehe, Martina Hofacker, and Fabian Welschinger. A phase field model for rate-independent crack propagation: Robust algorithmic implementation based on operator splits. Computer Methods in Applied Mechanics and Engineering, 199(45-48):2765–2778, November 2010.

[105] H B Muhlhaus. A variational principle for gradient plasticity. International Journal of Solids and Structures, 28:845–857, 1991.

[106] R M Murray and S S Sastry. A mathematical introduction to robotic manipulation. CRC PressINC, 1994.

[107] J C Nagtegaal, D M Parks, and J R Rice. On numerically accurate finite element solutions in the fully plastic range. Computer Methods in Applied Mechanics and Engineering, 4:153–177, 1974.

[108] A. Needleman. Material rate dependence and mesh sensitivity in localization problems. Computer Methods in Applied Mechanics and Engineering, 67(1):69–85, March 1988.

[109] A Needleman. Dynamic shear band development in plane strain. Journal of Applied Mechanics, 56:1–9, 1989.

[110] S Nemat-Nasser. Plasticity: A Treatise on Finite Deformation of Heterogeneous Inelastic Materials. Cambridge University Press, 2004.

[111] Glen H Nickodemus, Lawrence S Kramer, Joseph R Pickens, and Matthew S Burkins. Aluminum Alloys - Advances for Ground Vehicles. Advanced Materials and Processes, (February):51–54, 2002.

[112] A.G. G Odeshi, M.N. N Bassim, S. Al-Ameeri, and Q. Li. Dynamic shear band propagation and failure in AISI 4340 steel. Journal of Materials Processing Technology, 169(2):150–155, November 2005.

[113] Michael Ortiz, Yves Leroy, and Alan Needleman. A Finite Element Method for Localized Failure Analysis. Computer Methods in Applied Mechanics and Engineering, 61:189–214, 1987.

[114] T H H Pian and K Sumihara. Rational approach for assumed stress finite elements. International Journal of Numerical Methods in Engineering, 20:1638–1685, 1984.

[115] L A Piegl and W Tiller. The NURBS book. Springer, 2nd edition, 1997.

[116] D Pierce, C F Shih, and A Needleman. A Tangent Modulus Method for Rate Dependent Solids. Computers and Structures, 18(5):875–887, 1984.

[117] C Polizzotto. Unified thermodynamic framework for nonlocal/gradient continuum theories. European Journal of Mechanics A/Solids, 22:651–668, 2003.

[118] C Polizzotto and G Borino. A thermodynamics-based formulation of gradient dependent plasticity. European Journal of Mechanics A/Solids, 17:741–761, 1998.

[119] A. M. Rajendran, H. R. Last, and R. K. Garrett. Plastic flow and failure in HY100, HY130 and AF1410 alloy steels under high strain rate and impact loading conditions. Technical Report March, Army Research Lab, 1995.

[120] J R Rice. Inelastic constitutive relations for solids: an internal-variable theory and its application to metal plasticity. Journal of the Mechanics and Physics of Solids, 19:433–455, 1971.

[121] D F Rogers. An Introduction to NURBS With Historical Perspective. Academic Press, 2001.

[122] H L Schreyer and P J Maudlin. Thermodynamically consistent relations involving plasticity, internal energy and thermal effects. Philosophical transactions. Series A, Mathematical, physical, and engineering sciences, 363(1836):2517–41, November 2005.

[123] D. A. Shockey. No Title. Technical report, SRI, Int., California.

[124] J. C. Simo and Thomas J R Hughes. Computational Inelasticity. Springer, New York, 1998.

[125] J C Simo, J G Kennedy, and R L Taylor. Complementary mixed finite element formulations for elastoplasticity. Computer Methods in Applied Mechanics and Engineering, 74:177–206, 1989.

[126] J C Simo, K S Pister, and R Taylor. Variational and projection methods for the volume contraint in finite deformation elastoplasticity. Computer Methods in Applied Mechanics and Engineering, 51:177–208, 1985.

[127] L Stromberg and K Ristinmaa. FE-formulation of a nonlocal plasticity theory. Computer Methods in Applied Mechanics and Engineering, 136:127–144, 1996.

[128] H. Stumpf and K. Hackl. Micromechanical concept for the analysis of damage evolution in thermo-viscoelastic and quasi-brittle materials. International Journal of Solids and Structures, 40(6):1567–1584, March 2003.

[129] J Q Su, T W Nelson, R Mishra, and M Mahoney. Microstructural investigation of friction stir welded 7050-T651 aluminium. Acta Materialia, 51(3):713–729, 2003.

[130] G. I. Taylor and H. Quinney. The latent heat remaining in a metal after cold working. Proceedings of the Royal Society of London A, 163:157–181, 1937.

[131] Robert L Taylor. FEAP - - A Finite Element Analysis Program, April 2011.

[132] T.E. and Tezduyar. Stabilized Finite Element Formulations for Incompressible Flow Computations. volume 28 of Advances in Applied Mechanics, pages 1–44. Elsevier, 1991.

[133] W M Thomas and R E Dolby. Friction stir process welds alluminum alloys. In S A David, T DebRoy, J C Lippold, H B Smartt, and J M Vitek, editors, Proceedings of the Sixth International Conference on Trends in Welding Research. ASM International, Materials Park, Ohio, 1996.

[134] W M Thomas and E D Nicholas. Friction stir welding for the transporation industries. Material Design, 18:267–273, 1997.

[135] W M Thomas, E D Nicholas, J C Needham, M G Murch, P Temple-Smith, and C J Dawes. Friction stir butt welding. (Internaional Patent Number PCT/GB92/02203), 1991.

[136] George Z Voyiadjis and Rashid K Abu Al-Rub. A Finite Strain Plastic-damage Model for High Velocity using Combined Viscosity and Gradient Localization Limiters: Part II - Numerical Aspects and Simulations. International Journal of Damage Mechanics, 15:335–373, 2006.

[137] M Vural, D Rittel, and G Ravichandran. Large Strain Mechanical Behavior of 1018 Cold-Rolled Steel over a Wide Range of Strain Rates. Metallurgical and Materials Transactions A, 34:2873–2885, 2003.

[138] T. W. Wright. The Physics and Mathematics of Adiabatic Shear Bands. Cambridge University Press, 2002.

[139] T W Wright and R C Batra. The Initiation and Growth of Adiabatic Shear Bands. International Journal of Plasticity, 1:205–212, 1985.

[140] TW Wright and JW Walter. On stress collapse in adiabatic shear bands. Journal of the Mechanics and Physics of Solids, 35(6):701–720, 1987.

[141] J Yu. No Title. private communication.

[142] Alan T. Zehnder and Ares J. Rosakis. On the temperature distribution at the vicinity of dynamically propagating cracks in 4340 steel. Journal of the Mechanics and Physics of Solids, 39(3):385–415, January 1991.

[143] M Zhou, A Needleman, and R J Clifton. Finite Element Simulations of Shear Localization in Plate Impact. Journal of the Mechanics and Physics of Solids, 42:423–458, 1994.

[144] M Zhou, G Ravichandran, and AJ Rosakis. Dynamically propagating shear bands in impact-loaded prenotched plates-1. experimental investigations of temperature signatures and propagation speed. Journal of the Mechanics and Physics of Solids, 44(6):981–1006, 1996.

[145] M Zhou, G Ravichandran, and AJ Rosakis. Dynamically propagating shear bands in impact-loaded prenotched plates-II. numerical simulations. Journal of the Mechanics and Physics of Solids, 44(6):1007–1032, 1996.

[146] O C Zienkiewicz and R L Taylor. The Finite Element Method, volume Volume 1. Butterworth Heinemann, 5 edition, 2000.

Appendix A

Isogeometric modeling of shear bands

The contents of this appendix are reproduced from a work in progress by Luc Berger-Vergiat, Colin McAuliffe and Haim Waisman. Input from the co-authors is gratefully acknowledged.

Isogeometric Analysis [43, 73] (IGA) was originally developed with the intent of streamlining the simulation and design process. This process typically starts with discrete geometrical description of the part or system to be analyzed with a Computer Aided Design (CAD) package, which employ the NURBS basis functions [12, 54]. Once the geometry is fully described it is passed on to the simulation group, which in turn rediscretize the geometry according to the needs of the simulation technique chosen for analysis. IGA eliminates this rediscretization step from the simulation work flow by using the same basis functions for both the CAD geometrical description and analysis phases. Another added benefit of this approach is that now the geometry used during the analysis is exact.

Despite the original intent, perhaps the most interesting feature of IGA is the property of the NURBS shape functions when used for simulation. Basis functions constructed with NURBS are globally continuous across elements, not only within them. This means that solution computed with IGA are higher order and not piecewise higher order as would be the case with the $p-version$ of the finite elements method. Moreover, it is also easy to raise the polynomial order of these NURBS basis [47] which lead to more accurate simulations [25] with roughly as many nodes as for a simulation with a low order basis. This last property is due to the fact that IGA allows for a new type of refinement named $k-refinement$, an attractive feature which raises the order of the shape functions without excessively increasing the size of the linear system to be solved. Nonetheless, it should be noted that these matrices are also much denser than standard FEM matrices since the NURBS basis is not compactly supported.

The aim of the use of NURBS here is to reduce the computational cost of shear band simulations by finding shape functions which furnish the greatest accuracy for the lowest cost. To this end we tested multiple elements, with a focus on IGA based elements. The main evaluation method of these discretizations is study of the convergence rates, volumetric locking and memory usage. This paper begins by presenting the IGA formulation for the mixed finite elements, then introduces the PDE model

we chose to employ for shear bands. Finally, we study two test cases and assess the convergence properties of the proposed elements.

A.1 Computational modeling with NURBS functions

NURBS are functions designed to exactly represent curves and were originally created for computational geometry purposes. Detailed description of these functions, their properties, and how to compute them can be found in Piegl and Tiller [115] and Rogers [121].

NURBS are parametrized curves in d-dimensional spaces ($\mathbb{R}^d$ for example), constructed as a tensorial product of d 1D-NURBS curves. 1D-NURBS are themselves constructed as a rational combination of B-splines. In order to further describe B-splines functions we need to introduce the parametric space used to construct them. The parametric space associated with a B-spline function is called a knot vector and is composed of non-decreasing real numbers (the knots) $\Xi = \{\xi_1, \xi_2, \ldots, \xi_{n+p+1}\}$. By convention, the knot vector is scaled so that it spans the unit subspace $[0, 1] \subset \mathbb{R}$, where $\mathbb{R}$ is the space of all real numbers. The multiplicity of knots cannot exceed the degree of the curve $p + 1$ where p is also the degree of the polynomial basis used to construct the B-spline. n is the number of basis functions defined on the knot vector, it is also the number of control points used to describe the geometry of the B-spline. A knot vector is said to be open if its first and last knots have multiplicity $p+1$. Open knot vectors are commonly used since they produce bases that are interpolatory at the endpoints of the interval.
B-spline basis of order p are constructed recursively from an underlying piecewise constant basis

$$N_i(\xi) = \begin{cases} 1 & \text{if } \xi_i \leq \xi \leq \xi_{i+1}, \\ 0 & \text{otherwise.} \end{cases} \tag{A.1}$$

Bases of order p are then constructed using the following recursion formula

$$N_{i,p}(\xi) = \frac{\xi - \xi_i}{\xi_{i+p} - \xi_i} N_{i,p-1}(\xi) + \frac{\xi_{i+p+1} - \xi}{\xi_{i+p+1} - \xi_{i+1}} N_{i+1,p-1}(\xi) \tag{A.2}$$

first introduced by Cox and de Boor [47].
The associated B-spline curve is obtained using a linear combination of the basis function as follows

$$\mathcal{C}(\xi) = \sum_{i=1}^{n} \mathbf{P}_i N_i(\xi) \tag{A.3}$$

where $\mathbf{P}_i \in \mathbb{R}^d$ is the $i - th$ control point.
The B-splines can then be extended to multiple dimensions using a tensorial product,

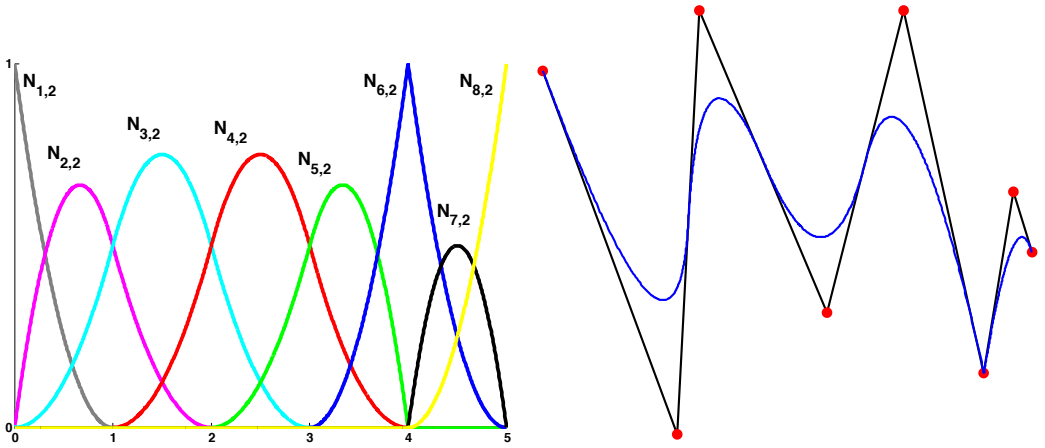

Figure A.1: On the left a quadratic basis of NURBS functions is represented. On the right the corresponding curve (in blue) is obtained where • represent the control points.

in the case of $d = 2$, we get the following expression for a B-spline surface

$$\mathcal{S}(\xi, \eta) = \sum_{i=1}^{n} \sum_{j=1}^{m} N_i(\xi) M_j(\eta) \mathbf{P}_{ij}, \tag{A.4}$$

where $M_j(\eta)$ are basis functions defined by the following knot vector $\mathcal{H} = \{\eta_1, \ldots, \eta_{m+q+1}\}$.
Finally NURBS basis functions are created using a rational combination of 1D B-spline basis functions, here again for $d = 2$, the result is

$$R_{ij}(\xi, \eta) = \frac{N_i(\xi) M_j(\eta) w_{ij}}{\sum_{i=1}^{n} \sum_{j=1}^{m} N_i(\xi) M_j(\eta) w_{ij}}. \tag{A.5}$$

These shape functions are combined with the control points to construct NURBS surfaces as follow

$$\mathcal{S}(\xi, \eta) = \sum_{i=1}^{n} \sum_{j=1}^{m} R_{ij} B_{ij}. \tag{A.6}$$

An example of a basis of NURBS functions and its associated curve are presented in Figure A.1.

Note how three shape functions are non zero over three elements instead of two as is the case for Lagrange or Hermite polynomials. It can also be observed that the curve is not interpolatory at all points. It generally is interpolatory only at the boundary.

The NURBS basis forms a partition of unity which makes it easy to use as a shape function basis for the finite element method (FEM). NURBS k-refinement preserves the number and geometry of the elements on the mesh for any order of shape functions, which allows us to use NURBS of different order in a mixed formulation.

A.2 Numerical results

In this section convergence studies for the plate in tension problem shown in chapter 2 are conducted for the small strain shear band formulation. Higher order NURBS shape functions are used for the displacement, temperature, and stress fields, while irreducible interpolation is used for the equivalent plastic strain field. The reason for this is that higher order interpolations for the equivalent plastic strain have been observed to lead to oscillations in this field, which are unphysical and fatal to the simulation. It may be possible to include an artificial diffusion term to smooth these unphysical oscillations, and thus permit use of NURBS functions on this field.

The error norm is defined here as the relative distance in an Euclidian space between some reference solution and the current computed solution, which is expressed as follow:

$$e = \frac{||u_{ref} - u||_2}{||u_{ref}||_2} = \frac{\sum_{i=1}^{n} (u_{ref,i} - u_i)^2}{\sum_{i=1}^{n} u_{ref,i}^2}. \tag{A.7}$$

The error terms for a specific solution field are computed at nodes which are shared by coarse and fine meshes, as illustrated by the red circles in Figure A.2. This also ensures that all the values used to compute the error on each mesh are actually values which have been solved for and not interpolated. This means that the error presented is least biased by the post-processing operations, and number of terms are determined by the coarsest grid.

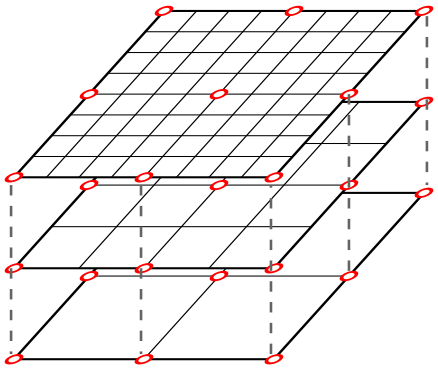

Figure A.2: The error terms contributing to the error norm are computed at the nodes denoted by •, which are shared on all hierarchy of grids.

On all the examples studied, the same structured discretizations have been employed, which have been generated by a tensorial product type of construction. Meshes with 10 by 10, 20 by 20, 30 by 30 and 40 by 40 elements are used, which allows observation of how the convergence rate is affected by h refinement. Convergence of the error is also investigated by k-refinement capabilities of the NURBS shape

functions.

As expected, the convergence of the fields discretized with NURBS shape functions exhibit fast convergence rates and smaller initial errors on coarse meshes see Figure A.3b to A.3e. These are significantly lower than the convergence rate and initial error observed for the Pian Sumihara element. The convergence rates of the EQPS are similar for all the elements.

The dependence of the computational time (CPU time) with respect to the size of the mesh (in 2D) is of the same order for all the elements. Therefore, the cost of mesh refinement for the NURBS element is comparable to the Pian Sumihara element. Thus to achieve a similar accuracy the NURBS element will take less cpu time than the Pian Sumihara element. Similarly Figure A.3g shows that the NURBS element requires less memory for a given accuracy than the memory required by the Pian Sumihara element, especially if high order NURBS functions are used.

(a)

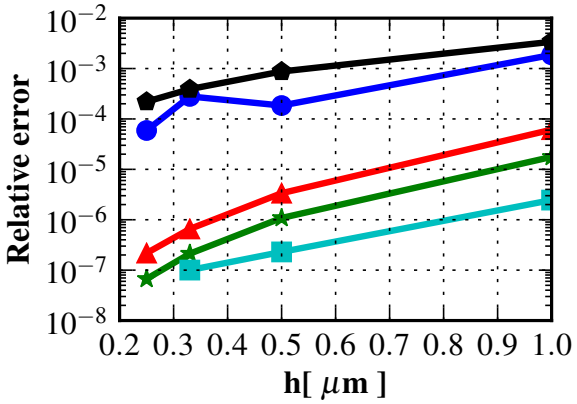

(b) Displacements

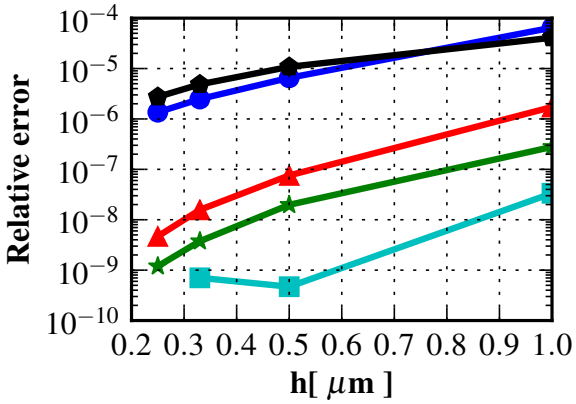

(c) Temperature

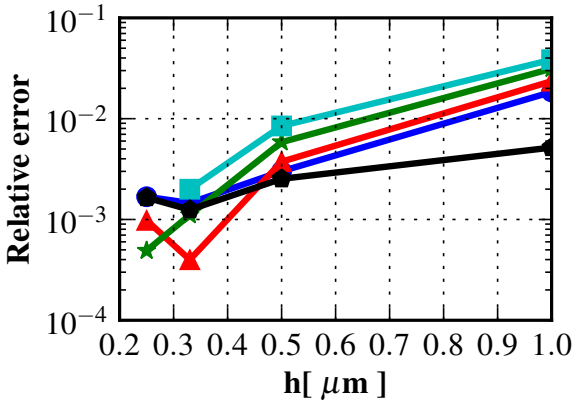

(d) Equivalent plastic strain

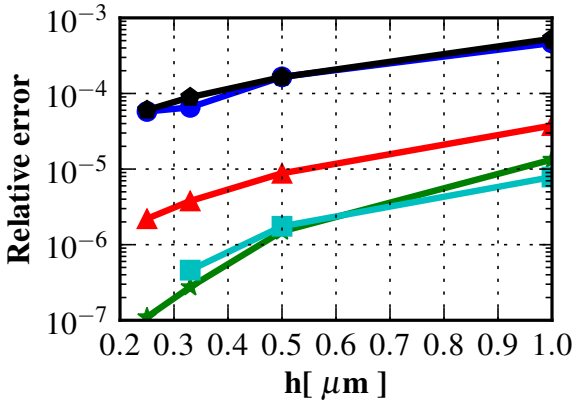

(e) von Mises stress

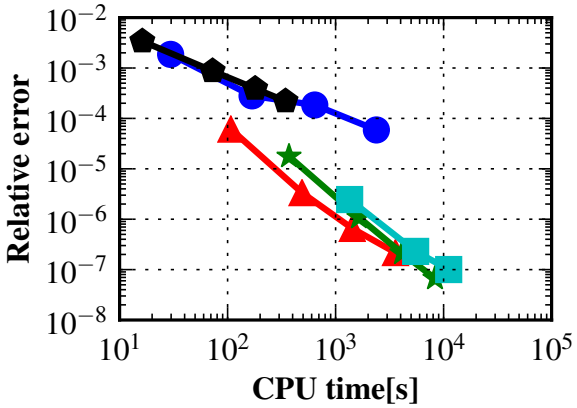

(f) Error against CPU usage

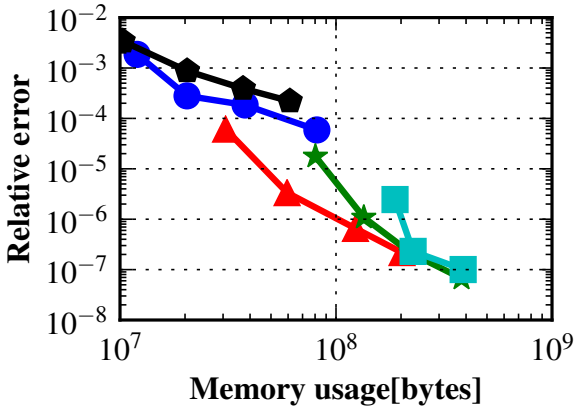

(g) Error against memory usage

Figure A.3: Convergence rate of the NURBS element using different order of NURBS basis function are shown for each solution field. Cpu time and memory usage are also shown.

Appendix B

Stability Analysis of the Shear Band Problem

The contents of this appendix are reproduced from a work in progress by Miguel Arriaga, Colin McAuliffe and Haim Waisman. Input from the co-authors is gratefully acknowledged.

Quantitative identification of stress collapse is of great interest for understanding the behavior of shear band models. Additionally, potential practical applications of a stress collapse identification method are element deletion schemes or domain decomposition based on stress collapse criteria. While mathematical instability does not necessarily imply stress collapse [91], instability analysis is a useful first step toward identifying stress collapse. Instability analysis of shear band models is conducted with the perturbation method of various continuous forms of shear band models [9, 58, 88] and the eigenanalysis of the acoustic tensor [87]. These methods each give the instability conditions for a single material point.

The perturbation method can also be applied to the semi discrete system of ordinary differential equations (ODEs) which result from applying Galerkin's method to the strong form given in chapter 2. This methodology results in a global instability criterion and has been applied to crystal growth in [84].

The general autonomous form of a system of equations is

$$\mathcal{L}(\dot{u}) = F(v) \tag{B.1}$$

where u represents all non-constant variables of the problem and $\mathcal{L}$ represents a linear operator. Note that $F(v)$ is not a linear function of v.

Consider v^*, a solution to (B.1) at a given moment in time, or in other words, an equilibrium point. Linearizing $F(v)$ with a Taylor Series Expansion around v^* gives

$$F(v) = F(v^*) + F'(v^*)(v - v^*) \tag{B.2}$$

Since v^* is an equilibrium point, then $F(v^*) = 0$, in which case (B.1) becomes

$$\mathcal{L}(\dot{v}) = F'(v^*)(v - v^*) \tag{B.3}$$

The problem can be centered at the equilibrium point such that the origin becomes the new equilibrium point. This is done by defining a new variable $u(t) = v(t) - v^*$ which permits application of Lyapunov indirect stability analysis [106]. Since v^* is a fixed equilibrium point $\dot{u} = \dot{v}$. Substituting this in (B.3) gives

$$\mathcal{L}(\dot{u}) = Au \tag{B.4}$$

where $A = F'(v^*)$ is the Jacobian of $F(v)$.

Applying the Galerkin discretization, these operators will assemble into matrices as follows,

$$\mathbf{M}\dot{\mathbf{u}} = \mathbf{A}\mathbf{u} \tag{B.5}$$

where $\mathbf{M}$ is the assembled matrix for all the mass matrices and $\mathbf{A} = \mathbf{K} + \mathbf{G}$ is the assembled matrix for both the linear stiffness matrices ($\mathbf{K}$) and the stiffness matrices associated with the non-linear behavior ($\mathbf{G}$), as described in chapter **??**.

Consider a linear perturbation of the form

$$\mathbf{u} = \mathbf{u_0} e^{\lambda t} \tag{B.6}$$

where we will call $\lambda \in \mathbb{C}$ an eigenvalue and $\mathbf{u_0}$ the corresponding eigenvector. Plugging (B.6) into (B.5) leads to

$$\lambda \mathbf{M}\mathbf{u} = \mathbf{A}\mathbf{u} \Rightarrow (\mathbf{A} - \lambda \mathbf{M})\,\mathbf{u} = \mathbf{0} \tag{B.7}$$

Non-trivial solution of (B.7) requires

$$\det(\mathbf{A} - \lambda \mathbf{M}) = 0 \tag{B.8}$$

which translates into a typical generalized eigenvalue problem [41].

The fact that λ is in the complex plane allows for some conclusions to be taken from its value. A very interesting description of these in the perspective of musical instruments is given by [70]. In short, a strictly imaginary value of λ corresponds to an oscillatory motion, whereas a strictly real value of λ corresponds to monotonic solution which can be asymptotically stable ($\lambda < 0$) or unstable ($\lambda > 0$). A combination of both is also possible, corresponding to a stable (unstable) oscillatory mode for a negative (positive) real part of the eigenvalue. This method for stability analysis (called the first method of Lyapunov) and was proposed by Lyapunov[94] and has also been referred to as the indirect method of Lyapunov[39, 106]. Shear banding instability is thus indicated by at least one eigenvalue with positive real part.

Preliminary results with the use of this method have determined that eigenanalysis of the local element form of (B.5) agrees with the local stability criteria from [88]. Eigenanalysis of the global form of (B.5) detects local instabilities as well as a global instability mode which dominates when the shear band propagates through the entire part. Research on these techniques for detecting shear banding is ongoing.

Appendix C

Linearization Examples

In this appendix two blocks of the Jacobian in equation (4.51) are derived in detail. The variation of the momentum equation with respect to displacement is computed by

$$J_i^{uu}\delta u_i = \delta R^{uu}\left[\delta u_i\right] = \lim_{\epsilon\to 0}\frac{1}{\epsilon}\left(R^u\left[u_i+\epsilon\delta u_i\right]-R^u\left[u_i\right]\right) = \frac{d}{d\epsilon}R^u\left[u_i+\epsilon\delta u_i\right]\Big|_{\epsilon=0} \tag{C.1}$$

Plugging (4.38) into (C.1) and separating the derivative into three parts due to the inertia term, the J in the stress divergence term, and the F^{-1} in the stress divergence term, gives

$$\delta R^{uu} = \delta R^{\ddot{u}} + \delta R^J + \delta R^{F^{-1}} \tag{C.2}$$

with

$$\delta R^{\ddot{u}} = \int_{\Omega_0} w_i^u \frac{\rho_0}{\mathcal{B}\Delta t^2}\delta u_i d\Omega_0 \tag{C.3}$$

$$\delta R^J = \int_{\Omega_0} w_{i,A}^u F_{Aj}^{-1}\left(\delta J\left[\delta u_i\right]\right)\sigma_{ij}\Omega_0 \tag{C.4}$$

$$\delta R^{F^{-1}} = \int_{\Omega_0} w_{i,A}^u \left(\delta F_{Aj}^{-1}\left[\delta u_j\right]\right) J\sigma_{ij}\Omega_0 \tag{C.5}$$

Noting the following linearizations of J and F^{-1}, which are derived in detail in [29]

$$\lim_{\epsilon\to 0}\frac{1}{\epsilon}\left[J\left[u_i+\epsilon\delta u_i\right]-J\left[u_i\right]\right) = J\delta u_{k,k} \tag{C.6}$$

$$\lim_{\epsilon\to 0}\frac{1}{\epsilon}\left(F_{Aj}^{-1}\left[u_j+\epsilon\delta u_j\right]-F_{Aj}^{-1}\left[u_j\right]\right) = -F_{Ak}^{-1}\delta u_{k,j} \tag{C.7}$$

equations (C.3) - (C.5) can be written as

$$\delta R^{\ddot{u}} = \int_{\Omega_0} w_i^u \frac{\rho_0}{\mathcal{B}\Delta t^2} \delta u_i d\Omega_0 \tag{C.8}$$

$$\delta R^{J} = \int_{\Omega_0} w_{i,A}^u F_{Aj}^{-1} \tau_{ij} \delta u_{k,k} \Omega_0 \tag{C.9}$$

$$\delta R^{F^{-1}} = -\int_{\Omega_0} w_{i,A}^u F_{Ak}^{-1} \tau_{ij} \delta u_{k,j} \Omega_0 \tag{C.10}$$

after some index manipulation, δR^{uu} is

$$\delta R^{uu} = \int_{\Omega_0} w_i^u \frac{\rho_0}{\mathcal{B}\Delta t^2} \delta u_i - w_{i,A}^u F_{Aj}^{-1} \left[\tau_{ij}\delta_{kl} - \tau_{il}\delta_{jk}\right] \delta u_{k,l} d\Omega_0 \tag{C.11}$$

Substitution of the Galerkin approximation into (C.11), leads to

$$\delta \mathbf{R}_\alpha^{uu} = \mathbf{J}_{\alpha\beta}^{uu} \delta \hat{u}_\beta = \int_{\Omega_0} \frac{\rho_0}{\mathcal{B}\Delta t^2} N_{i\alpha}^u N_{i\beta}^u - J N_{i\alpha,A}^u F_{Aj}^{-1} \left[N_{ij\zeta}^\sigma \hat{\lambda}_\zeta \delta_{kl} - N_{il\zeta}^\sigma \hat{\lambda}_\zeta \delta_{jk}\right] N_{k\beta,l}^u d\Omega_0 \delta \hat{u}_\beta \tag{C.12}$$

or

$$\mathbf{J}_{\alpha\beta}^{uu} = \int_{\Omega_0} \frac{\rho_0}{\mathcal{B}\Delta t^2} N_{i\alpha}^u N_{i\beta}^u - J N_{i\alpha,A}^u F_{Aj}^{-1} \left[N_{ij\zeta}^\sigma \hat{\lambda}_\zeta \delta_{kl} - N_{il\zeta}^\sigma \hat{\lambda}_\zeta \delta_{jk}\right] N_{k\beta,l}^u d\Omega_0 \tag{C.13}$$

The first term is a linear mass matrix and the second term is a stiffness matrix arising from geometric nonlinearity. In equation (4.51), these are denoted as $\mathbf{M}_{\alpha\beta}^u$ and $\mathbf{L}_{\alpha\beta}^u$ respectively. The second example we will derive is the block $\mathbf{J}_{\alpha\beta}^{\sigma u}$, which is the variation of the elasticity equation with respect to displacement. This is

$$J_i^{\sigma u} \delta u_i = \delta R^\sigma \left[\delta u_i\right] = \lim_{\epsilon \to 0} \frac{1}{\epsilon} \left(R^\sigma \left[u_i + \epsilon \delta u_i\right] - R^\sigma \left[u_i\right]\right) = \frac{d}{d\epsilon} R^\sigma \left[u_i + \epsilon \delta u_i\right] \Big|_{\epsilon=0} \tag{C.14}$$

Separating δR^σ into a five parts,

$$\delta R^\sigma = \delta R^{\sigma J} + \delta R^{\sigma spin} + \delta R^{\sigma mat} + \delta R^{\sigma d^p} + \delta R^{\sigma \tilde{\tau}} \tag{C.15}$$

due to the J term in the Jaumann rate, the d terms in the spin correction, the d term in the material rate, the J terms in d^p, and the F terms in $\tilde{\tau}$, respectively, we obtain

$$\delta R^{\sigma J} = \int_{\Omega_0} w_{ij}^{\sigma} \left(\delta J\left[\delta u_i\right]\right)\left[\sigma_{ij} - \Delta t\left(d_{ik}\sigma_{kj} + \sigma_{ik}d_{kj}\right)\right] d\Omega_0 \tag{C.16}$$

$$\delta R^{\sigma spin} = -\int_{\Omega_0} w_{ij}^{\sigma} \Delta t J\left(\left(\delta d_{ik}\left[\delta u_i\right]\right)\sigma_{kj} + \sigma_{ik}\left(\delta d_{kj}\left[\delta u_k\right]\right)\right) d\Omega_0 \tag{C.17}$$

$$\delta R^{\sigma mat} = -\int_{\Omega_0} w_{ij}^{\sigma} \Delta t C_{ijkl}^{elas}\left(\delta d_{kl}\left[\delta u_k\right]\right) d\Omega_0 \tag{C.18}$$

$$\delta R^{\sigma d^p} = \int_{\Omega_0} w_{ij}^{\sigma} \Delta t C_{ijkl}^{elas} \frac{3 s_{kl}}{2\bar{\tau}}\left(\delta g\left(J\bar{\sigma}, T, \bar{\gamma}^p\right)\left[\delta u_i\right]\right) d\Omega_0 \tag{C.19}$$

$$\delta R^{\sigma\tilde{\tau}} = -\int_{\Omega_0} w_{ij}^{\sigma}\left(\delta f_{ia}\left[\delta u_i\right]\right)\ {}_n\tau_{ab} f_{jb} + f_{ia}\ {}_n\tau_{ab}\left(\delta f_{jb}\left[\delta u_j\right]\right) d\Omega_0 \tag{C.20}$$

The linearizations of f and f^{-1} are needed for $J^{\sigma\tilde{\tau}}$ and terms which contain linearized d. These are

$$\lim_{\epsilon\to 0}\frac{1}{\epsilon}\left(f_{ia}\left[u_i + \epsilon\delta u_i\right] - f_{ia}\left[u_i\right]\right) = \delta u_{i,j} f_{ja} \tag{C.21}$$

$$\lim_{\epsilon\to 0}\frac{1}{\epsilon}\left(f_{ai}^{-1}\left[u_i + \epsilon\delta u_i\right] - f_{ai}^{-1}\left[u_i\right]\right) = -f_{aj}^{-1}\delta u_{j,i} \tag{C.22}$$

using (C.21) in (C.20), the linearization of $\tilde{\tau}_{ij}$ becomes

$$\delta\tilde{\tau}_{ij}\left[\delta u_i\right] = \left(\delta_{ki}\tilde{\tau}_{lj} + \tilde{\tau}_{il}\delta_{kj}\right)\delta u_{k,l} \tag{C.23}$$

using (C.22), the linearization of d becomes

$$2\Delta t\left(\delta d_{ij}\left[\delta u_i\right]\right) = -\left(\delta f_{ai}^{-1}\left[\delta u_i\right]\right) f_{aj}^{-1} - f_{ai}^{-1}\left(\delta f_{aj}^{-1}\left[\delta u_j\right]\right) \tag{C.24}$$

$$= -\left(\delta_{il}E_{kj} + E_{ik}\delta_{jl}\right)\delta u_{k,l} \tag{C.25}$$

where

$$E_{ij} = f_{ai}^{-1} f_{aj}^{-1} \tag{C.26}$$

to linearize g, the chain rule is necessary, the result is

$$\delta g\left(J\bar{\sigma}, T, \bar{\gamma}^p\right)\left[\delta u_i\right] = \delta g\left(J\bar{\sigma}, T, \bar{\gamma}^p\right)\left(\delta J\left[\delta u_i\right]\right) \tag{C.27}$$

$$= m g\left(J\sigma, T, \bar{\gamma}^p\right)\delta u_{k,k} \tag{C.28}$$

using (C.21) - (C.28) we can rewrite (C.16) - (C.20) as

$$\delta R^{\sigma J} = \int_{\Omega_0} w_{ij}^{\sigma} \left[\tau_{ij} - \Delta t \left(d_{ik}\tau_{kj} + \tau_{ik}d_{kj}\right)\right] \delta u_{l,l} d\Omega_0 \tag{C.29}$$

$$\delta R^{\sigma spin} = \int_{\Omega_0} w_{ij}^{\sigma} \frac{1}{2} \left[\delta_{li}E_{kr}\tau_{rj} + E_{ik}\tau_{lj} + \tau_{il}E_{kj} + \tau_{ir}E_{rk}\delta_{lj}\right] \delta u_{k,l} d\Omega_0 \tag{C.30}$$

$$\delta R^{\sigma mat} = \int_{\Omega_0} w_{ij}^{\sigma} C_{ijrl}^{elas} E_{rk} \delta u_{k,l} d\Omega_0 \tag{C.31}$$

$$\delta R^{\sigma d^p} = \int_{\Omega_0} w_{ij}^{\sigma} \Delta t C_{ijkl}^{elas} \frac{3ms_{kl}}{2\bar{\tau}} g\left(J\bar{\sigma}, T, \bar{\gamma}^p\right) \delta u_{r,r} d\Omega_0 \tag{C.32}$$

$$\delta R^{\sigma \tilde{\tau}} = -\int_{\Omega_0} w_{ij}^{\sigma} \left[\delta_{ki}\tilde{\tau}_{lj} + \tilde{\tau}_{il}\delta_{kj}\right] \delta u_{k,l} d\Omega_0 \tag{C.33}$$

we group the material terms, $\delta R^{\sigma mat}$ and δR^{d^p} into K^{σ} and the remaining three geometric terms into L^{σ} so that

$$K^{\sigma} = \int_{\Omega_0} w_{ij}^{\sigma} C_{ijrl}^{elas} E_{rk} \delta u_{k,l} + \Delta t C_{ijkl}^{elas} \frac{3ms_{kl}}{2\bar{\tau}} g\left(J\bar{\sigma}, T, \bar{\gamma}^p\right) \delta u_{r,r} d\Omega_0 \tag{C.34}$$

$$\begin{aligned} L^{\sigma} = & \int_{\Omega_0} w_{ij}^{\sigma} \Big\{ \left[\tau_{ij} - \Delta t \left(d_{ik}\tau_{kj} + \tau_{ik}d_{kj}\right)\right] \delta_{kl} + \frac{1}{2} \left[\delta_{li}E_{kr}\tau_{rj} + E_{ik}\tau_{lj} + \tau_{il}E_{kj} + \tau_{ir}E_{rk}\delta_{lj}\right] \\ & - \left[\delta_{ki}\tilde{\tau}_{lj} + \tilde{\tau}_{il}\delta_{kj}\right] \Big\} \delta u_{k,l} d\Omega_0 \end{aligned} \tag{C.35}$$

Substitution of the Galerkin approximation then gives $\mathbf{K}_{\alpha\beta}^{\sigma}$ and $\mathbf{L}_{\alpha\beta}^{\sigma}$, with $\mathbf{J}_{\alpha\beta}^{\sigma u} = \mathbf{K}_{\alpha\beta}^{\sigma} + \mathbf{L}_{\alpha\beta}^{\sigma}$.